RSC Advances

REVIEW

View Article Online
View Journal | View Issue

Cite this: *RSC Adv.*, 2025, **15**, 23266

Flexible photovoltaics based on perovskite materials

Abdelaal S. A. Ahmed, *[a] Fatma S. M. Hashem,[b] Abu-Bakr A. El-Adasy[a] and Tarek A. Seaf El-Nasr[ac]

Flexible perovskite solar cells (FPSCs) have received extensive interest for application in wearable electronic devices owing to their high flexibility, light weight, and compatibility with irregular-shaped electronic devices. The roll-to-roll manufacturing method, which exhibits high capacity for mass production, has enabled significant advancements in FPSCs *via* composition engineering, interface modification, fabrication process optimization, and new charge transport materials. Devices utilizing high-quality perovskite films have achieved a power conversion efficiency (PCE) exceeding 24%. This paper comprehensively outlines the recent advancements in the development of FPSCs, including flexible substrates, electrodes, low-temperature interlayers, and diverse methodologies for fabricating high-quality perovskite films. This review also discusses the existing challenges and outlines future opportunities for growth in this rapidly evolving field.

Received 12th April 2025
Accepted 20th June 2025

DOI: 10.1039/d5ra02563j

rsc.li/rsc-advances

1 Introduction

The utilization of electrical energy has become indispensable for the advancement of human society, underpinning the operation of numerous devices and systems including lighting, domestic appliances, and climate control technologies. Thus, with the rapidly increasing global population, securing a constant energy supply is considered one of the most pressing concerns encountered presently.[1] Fossil fuels remain the dominant energy source; however, their depletion and environmental consequences underscore the importance of renewable alternatives such as wind energy, solar energy, geothermal energy, and bio-energy to satisfy the global energy demand.[2] These energy sources are generally considered environmentally friendly, and their utilization in place of fossil fuels has the potential to significantly reduce environmental pollution and mitigate global warming. The abundance of solar irradiance across the globe makes solar energy a viable contributor to the future energy system. It has been reported that Earth receives a great amount of solar radiation per hour, which is sufficient for human energy needs for an entire year.[2] Additionally, owing to the decline in the levelized cost of electricity (LCOE) for solar photovoltaics (PVs), reaching levels comparable to fossil fuels', they are becoming an increasingly attractive and competitive alternative to fossil fuels. Thus, the use of solar energy as a sustainable energy source has attracted great attention.[3] Thus far, many technologies have been developed, such as heating,[4] photocatalysis,[5] and solar PV,[6] to benefit from solar energy in various aspects of daily life. Solar cells are encouraging devices that directly convert sunlight into electricity *via* photovoltaics.[7] Recently, PVs have attracted great interest as a promising renewable energy supply to satisfy all our energy demands without polluting the environment for the coming generations.[8] Consequently, various types of PVs have been developed; the first PV generation, also known as silicon-based solar cells (Si-PVs), was first developed in 1954 at Bell Labs.[6] The second PV generation is called thin-film solar cells (TFSCs), which was developed in the 1970s as a result of the oil shock.[9] This generation is composed of various types of PVs, such as copper–indium–selenide ($CuInSe_2$)-based,[10] gallium arsenide (GaAs)-based,[11] and cadmium telluride (CdTe)-based devices.[12] However, their high fabrication cost, heavy weight, and rigid structure limit their roll-to-roll (R-to-R) continuous mass production.[13] Thus, to overcome the shortcomings in the first two generations, great efforts have been devoted to developing alternative PV systems. The developed PVs belonging to the third generation include organic photovoltaics (OPV), quantum dot solar cells (QDSCs),[14] dye-sensitized solar cells (DSSCs),[8,15–17] and perovskite solar cells (PSCs).[18] The viability of PVs for commercialization mainly depends on some critical factors, including the overall power conversion efficiency (PCE), long-term stability, and the total production cost. Recently, wearable and portable electronic devices have received much interest in next-generation artificial intelligence technologies.[19] These devices have become a reality through innovations like flexible phone displays, electronic skin sensors, and bendable

[a]*Chemistry Department, Faculty of Science, Al-Azhar University, Assiut 71524, Egypt. E-mail: abdelaalsaiyd@azhar.edu.eg; abdelaalsaiyd@gmail.com*

[b]*Chemistry Department, Faculty of Science, Assuit University, Assiut 71524, Egypt*

[c]*Department of Chemistry, College of Science and Arts, Jouf University, Sakaka 2014, Saudi Arabia*

solar panels due to their lightweight, flexible, wearable, and smart-friendly nature, revealing significant market potential. The power supply of these devices plays a crucial role in their shaping and design. This advancement in portable electronics has also driven increased demand for next-generation photovoltaic technologies.[20–23] Thanks to the flexibility of certain third-generation photovoltaic materials, like organic and perovskite compounds, they hold promise for use in non-flat surfaces, enabling the production of flexible solar cell (FSC) devices and even wearable technology that conforms to the human body.[24,25] The lightweight nature and high energy-to-weight (W g^{-1}) ratio of these flexible devices offer vast potential for various applications, opening up new markets that could support economic growth.[26,27] Along with near-space uses for robotic insects, weather balloons, self-powered blimps, small unmanned aircraft, and distributed power production.[28] Usually, lightweight, flexibility, portability, conformability, and power-per-weight ratio (specific power under standard solar irradiation (100 mW cm^{-2}, AM 1.5G, 25 °C)) were reported as critical factors to gauge the PV devices. Compared with conventional PVs, FSCs are typically much thinner and lighter, significantly lowering all associated expenses (production, storage, shipping, and transportation).[29] The most encouraging aspect of FSCs is their high ability to be constructed *via* continuous R-to-R technology with a shorter time, lower cost, and simpler manufacturing equipment.[30] In addition to their superior resistance to bending, torsion, and stretching, flexible devices offer practical benefits like portability and lightweight.[31]

Till now, various kinds of FSCs have been developed, including flexible silicon-based solar cells and TFSCs (*e.g.*, CIGS and CdTe).[32] Unfortunately, their general applicability is constrained by the complex fabrication methods linked to the high cost and use of various dangerous metals.[33] Thus, great attention has been devoted to developing alternative FSCs from the third generation, such as flexible-DSSCs (FDSSCs),[34] flexible-QDSSCs (FQDSSCs), and flexible-PSCs (FPSCs).[35] Compared with other flexible photovoltaic systems, FPSCs have emerged as viable options due to their excellent photovoltaic efficiency and lightweight, flexible design.[19,36] It is anticipated that FPSCs will find specialized uses in wearable and portable electronics, self-powered electronics,[37] and smart integrated buildings.[38] More significantly, FPSCs can be made using the R-to-R printing technique,[39] which will facilitate their mass manufacturing and advance their future commercialization.[40,41] Consequently, the development of FPSCs is crucial for the real-world use of PSCs. Thus, in this work, we aimed to present the current developments in FPSCs, including flexible substrates, electrode preparation, and the production of perovskite films. Then, the real application of FPSCs with common examples is introduced. Finally, a conclusion and outlook for the further development of FPSCs are provided.

2 Perovskite materials and flexible perovskite solar cells

Here, the fundamental structure of perovskites and their electrical and optical characteristics will be presented. Moreover, the recent progress in flexible perovskite photovoltaics will be discussed. The term perovskite is widely used to describe a calcium titanate ($CaTiO_3$) mineral.[42] The molecular formula of perovskite is ABX_3, where A is an organic and/or inorganic cation, such as methylammonium ($CH_3NH_3^+$ or MA^+), formamidine ($HN{=}CHNH_3^+$ or FA^+), or cesium (Cs^+), B is a divalent metal cation (Pb^{2+} or Sn^{2+}), and X is a halide anion (I^-, Br^-, Cl^-). Recently, diverse study domains, including material physics and chemistry, have shown significant interest in halide perovskites.[43–47] Generally, perovskite materials, even oxides (ABO_3), and non-oxides (ABX_3),[48] have high-temperature superconductivity, which indicates their superior electrical properties. The various properties of perovskite materials have been described by Li *et al.*[35] and Wei *et al.*[49] It has been reported that the electronic structures of perovskite are dictated by BX_6 blocks.[50,51] In halide perovskites, each $CH_3NH_3^+$ and Pb^{2+} cation offers one and two electrons to I_3, respectively. The electrical neutrality of the $CH_3NH_3^+$ and Pb–I structures results from their weak van der Waals force. As a result, the $CH_3NH_3^+$ cation rarely affects the properties of "Pb" in the conduction band (CB) and "I" in the valence band (VB). In contrast to most cations with empty outer s orbitals, Pb has an electron orbit (6s) below the top of its VB. Thus, the unusual electronic characteristics of perovskite are mostly caused by the lone pairs of "s" electrons in the "Pb" ions.[52]

Based on the density of states (DOS) and partial charge density, the valence band maximum (VBM) in halide perovskites exhibits strong antibonding character between the Pb s and I p orbitals. In contrast, the conduction band minimum (CBM) is primarily formed by the Pb p states. This unique electronic structure, featuring both ionic and covalent characteristics, stems from the molecular structure of the perovskite as well as the properties of the individual ions.[49] In conventional semiconductors, the VBM and CBM are typically dominated by p and s orbitals, respectively.[49] However, in halide perovskites, this trend is reversed. This inversion is one of the factors contributing to their exceptional optoelectronic performance. Another key advantage of perovskite solar cells (PSCs) is their high optical absorption, in which a perovskite absorber layer with a thickness of less than 500 nm can achieve a PCE of 15%. In comparison, the absorber layers in first and second-generation photovoltaics usually require much thicker layers; about 300 μm and 2 μm, respectively. The optical absorption of semiconductors is typically evaluated using two parameters, as follows: (i) the transition matrix elements between the VB and CB states, which determine the probability of each photoelectric transition, and (ii) the joint density of states (JDOS), which represents the total number of possible photoelectric transitions. Therefore, the optical absorption coefficient is closely linked to the electronic structure of the materials. Fig. 1 illustrates the mechanisms of optical absorption in first, second, and third-generation photovoltaics.

In silicon absorbers, optical absorption primarily occurs through transitions involving Si p and Si s/p orbitals. However, because silicon is an indirect bandgap semiconductor, the probability of electronic transitions between their VB and CB is significantly lower; approximately two times lower compared to materials with a direct bandgap. Consequently, the absorber

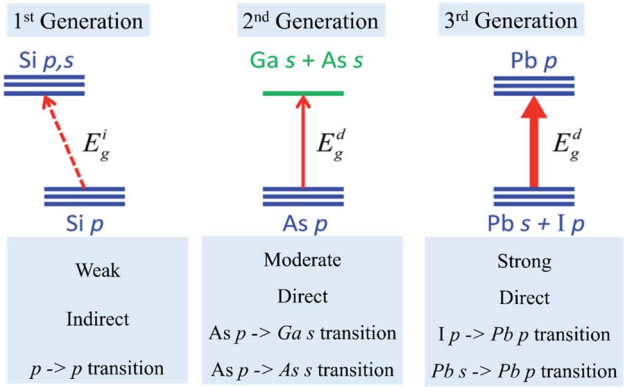

Fig. 1 Scheme representing the optical absorption of the absorbers in the 1st, 2nd, and 3rd generations of PVs. Reprinted with permission from ref. 49. Copyright 2015, Royal Society of Chemistry.

layer must be two orders of magnitude thicker to achieve sufficient absorption, which substantially increases the overall material cost. Other absorber materials, such as GaAs and halide perovskites (*e.g.*, $CH_3NH_3PbI_3$), possess direct bandgaps, which result in significantly stronger optical absorption compared to silicon. However, their electronic structures differ in notable ways. In $CH_3NH_3PbI_3$, the lower portion of its CB is primarily composed of degenerate Pb p orbitals, while in GaAs, the CB edge arises from a more dispersive s band. Additionally, in $CH_3NH_3PbI_3$, its edge transition originates from the hybridized (Pb s, I p) orbitals to Pb p orbitals. The transition probability between the VBM and CBM in $CH_3NH_3PbI_3$ is comparable to that in GaAs, owing to the strong intra-atomic Pb s → Pb p transition. Taken together, these features enable halide perovskites to exhibit even greater optical absorption than GaAs.

Based on the above-mentioned characteristics, perovskite materials demonstrate strong potential for photovoltaic applications, both in conventional and flexible formats. Among them, organic–inorganic lead halide perovskites, $CH_3NH_3PbI_3$, are some of the most widely used absorber materials for photovoltaics due to their optimal bandgap (1.57 eV),[53] and low exciton binding energy (50 meV).[54] The use of perovskite materials in opto electronic devices dates back to 1994, as reported by Tsutsui *et al.*[55] In this study, they employed the $(C_6H_5C_2H_4NH_3)_2PbI_4$ perovskite material in devices to study their fluorescence under electrical excitation. At low temperatures, an emission peak at 520 nm with a narrow full width at half-maximum (FWHM) of about 10 nm was observed. By utilising light-emitting diodes (LEDs), the obtained perovskite-based LEDs achieved brightness levels nearly five-times higher than conventional organic light-emitting diodes (OLED). Since then, the remarkable optical and electronic properties of perovskite materials have attracted significant attention for photovoltaic applications.[56] The photovoltaic performance of perovskite materials was first reported in 2009 by Kojima *et al.*,[57] in which a hybrid perovskite was used as a highly effective light-harvesting material in liquid electrolyte-based DSSCs. The assembled device achieved a PCE of 3.9%. However, a major limitation was its poor stability, given that the perovskite rapidly degraded in the presence of the liquid electrolyte. Thus, to address this issue, subsequent research introduced solid-state organic hole transport materials as alternatives to the liquid electrolyte.[58–60] In less than a decade, PSCs have achieved remarkable progress, with their PCE exceeding 25%. This value exceeds the PCEs of polycrystalline Si-PVs (22.3%), thin film crystalline Si PVs (21.2%), $CuInSe_2$ (22.6%), and CdTe PVs (22.1%). These improvements in the overall performance of PSCs can assigned to their many intrinsic properties such as high absorption coefficients, high defect tolerance, desirable/tunable bandgap, mechanical flexibility, and long charge carrier diffusion lengths.[61,62] Additionally, the cost-effective materials, mechanical durability, and low-temperature fabrication procedures (typically <150 °C) of PSCs make them suitable for realizing flexible perovskite solar cells (FPSCs) using a plastic substrate. Furthermore, FPSCs using plastic substrates would produce the most competitive power per weight among the solar cells. Consequently, FPSCs can be employed in specialized fields including electronic textiles, large-scale industrial roofs, portable electric chargers, and unmanned aerial vehicle (UAV) power sources.[35,63–68] FPSCs have shown a rapid performance improvement, and the first study on FPSCs was reported in 2013 by Mathews *et al.*,[69] in which the assembled FPSCs displayed a PCE of 2.62%. Subsequent developments have led to continuous performance enhancements, with recent devices achieving PCEs as high as 24.3% (Fig. 2),[35,69–80] which is considered the highest performance among TFSC devices. In comparison to alternative photovoltaic technologies such as Si, Cu(In, Ga)Se_2 (CIGS), CdTe, and organic solar cells, FPSCs have demonstrated a remarkable specific power-per-weight (W g^{-1}).[36,81,82] For example, Kaltenbrunner *et al.*[83] developed a lightweight FPSC that achieved a PCE exceeding 12% by utilizing an ultra-thin PET substrate with a thickness of 1.4 μm. These flexible devices maintained their original performance under 40% compression. Furthermore, owing to their extremely low thickness, the assembled devices showed a specific power output reaching 23 W g^{-1}. Furthermore, Kang *et al.*[84] reported that FPSCs assembled with silver nanowire (AgNW) transparent electrodes fabricated on 1.3 μm-thick polyethylene naphthalate foils demonstrated a specific power output of 29.4 W g^{-1}, outperforming other thin-film photovoltaics such as amorphous silicon (a-Si; 8.31 W g^{-1}),[85] organic solar cells (OSC; 10 W g^{-1}),[86] lead sulfide quantum dot solar cells (PbS QDs; 12.3 W g^{-1}),[87] and CdS/CdTe solar cells (0.254 W g^{-1}),[88] which is considered one of the highest values in photovoltaic technology.

Mechanical flexibility is another critical factor for the real applicability of FPSC devices. The fabrication of deformable and stretchable FPSCs is possible through the use of flexible substrates with excellent bending resilience.[35,89,90] For example, Park *et al.* utilized a shape-memory polymer as a substrate to develop highly deformable FPSCs.[90] The assembled FPSC devices displayed excellent mechanical stability, as indicated by the loss of only 40% of their initial value after 50 cycles of complete deformation and recovery. Additionally, one of the primary characteristics of FPSCs is their ability to work with flexible substrates, which permits high-throughput R-to-R production and may attract significant industry participants. In addition to enabling the manufacture of conventional silicon-based devices, R-to-R processing also makes it possible to create modules with unique shapes. Moreover, a significant

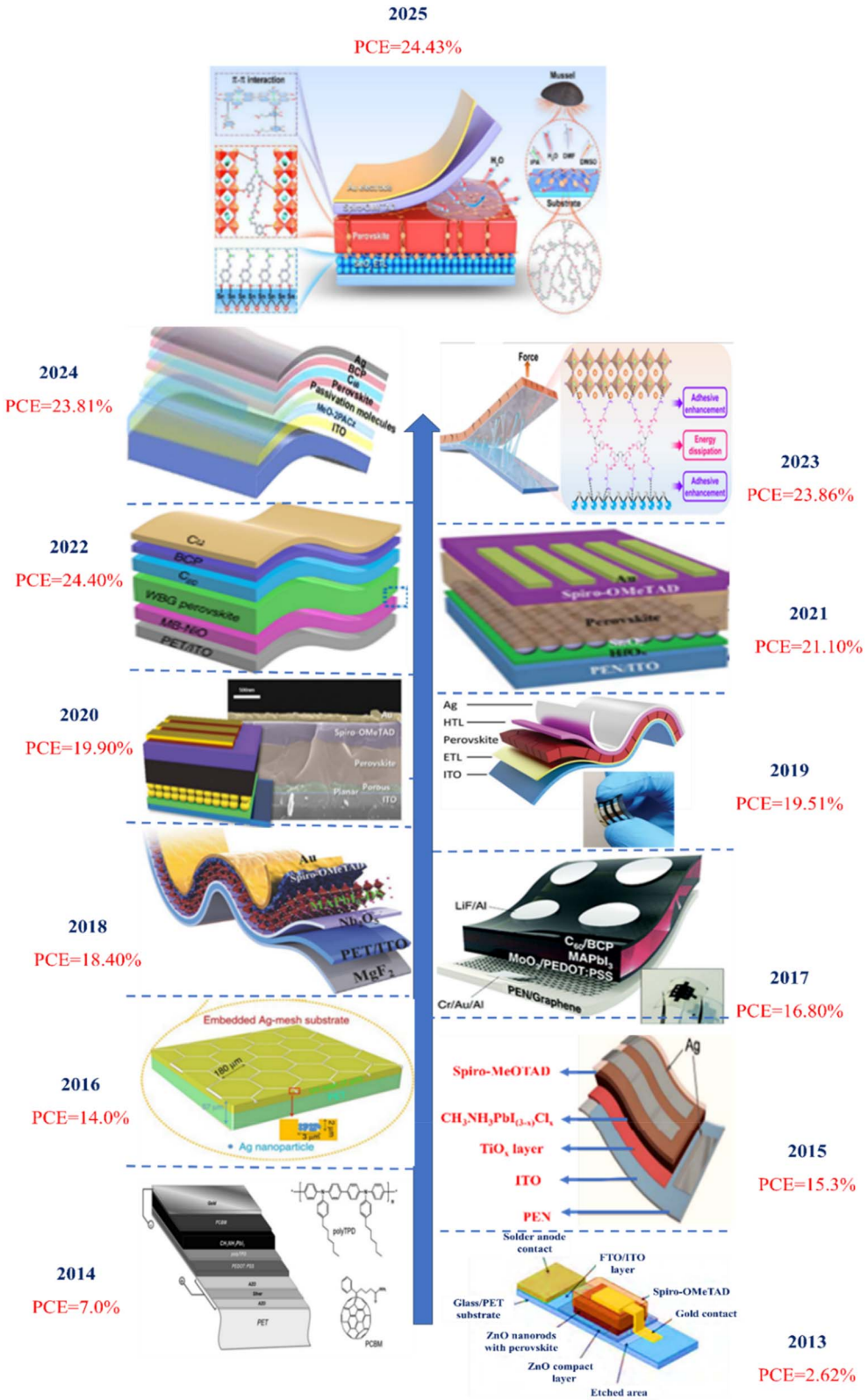

Fig. 2 Efficiency evolution of FPSCs from 2013 to 2025. Reprinted with permission from ref. 35, 69–72 and 74–80. Copyright 2013, 2014, 2017, 2020, 2021, Royal Society of Chemistry. Copyright 2015, 2016, 2022, 2023, 2025, Springer Nature. Copyright 2018, 2019 Wiley-VCH, Copyright 2024, American Chemical Society, [2013 PCE = 2.62%, 2014 PCE = 7.0%, 2015 PCE = 15.3%, 2016 PCE = 14.0%, 2017 PCE = 16.80%, 2018 PCE = 18.40%, 2019 PCE = 19.51%, 2020 PCE = 19.90%, 2021 PCE = 21.10%, 2022 PCE = 24.40%, 2023 PCE = 23.86%, 2024 PCE = 23.81%, 2025 PCE = 24.43%] .

advantage of FPSCs is their ability to work with flexible substrates, making them well-suited for high-speed R-to-R manufacturing, which can lead to their industrial production. The R-to-R technique not only accelerates production relative to conventional silicon devices but also facilitates the development of modules in various smart shapes.[91–94] For example, Galagan *et al.*[95] used the R-to-R slot die coating method to prepare FPSCs on flexible substrates. The fabricated FPSC devices with a mask of 0.04 cm^2 displayed a PCE of 14.5%. Additionally, the overall performance of the manufactured devices remained unchanged after 1000 bending cycles with a bending radius of 10 mm. In another study, Bu *et al.*[96] used the slot-die print method for preparing high-quality tin oxide (SnO_2) films for FPSCs. The small-size FPSCs achieved a PCE of 17.18%, while the devices with larger sizes (5 × 6 cm^2) displayed an efficiency of over 15%.

All the above-mentioned amazing characteristics make FPSCs ideal for wearable and portable electronic applications. However, the relatively lower PCE of FPSCs than that for rigid devices is still a challenge that seriously limits their further commercialization, and thus needs to be addressed.[97] The roughness and deformability of polymer substrates are common factors responsible for damage to the quality of the charge transport and perovskite layers, lowering the efficiency of FPSCs.[98] In addition to mechanical issues, the high sheet resistance and low transparency of flexible substrates negatively impact the FF and J_{SC} of FPSCs, particularly in the context of large-area device fabrication.[99] Furthermore, the low processing temperature (~100 °C) necessary for flexible substrates limits the crystallinity of the charge transport layers and perovskite films, thereby reducing the device efficiency.[74] Therefore, in the last few years, great efforts have been devoted to overcoming these limitations, and hence it is important to review and summarize the recent progress in the development of FPSCs.

3 The main components of FPSCs

The typical sandwich structure of an FPSC device includes a flexible substrate, cathode, electron-transport layer (ETL), perovskite photoactive layer, hole-transport layer (HTL), and anode. As illustrated in Fig. 3, the perovskite absorber layer is sandwiched between the ETL and an HTL. The commonly used ETL materials include TiO_2, SnO_2, and ZnO, while the HTL is typically composed of 2,2′,7,7′-tetrakis-(*N*,*N*-di-4-methoxyphenylamino)-9,9′-spirobifluorene (spiro-OMeTAD) or poly[bis(4-phenyl)(2,4,6-trimethylphenyl)amine] (PTAA). A transparent conducting oxide (TCO), such as indium tin oxide (ITO) or fluorine-doped tin oxide (FTO) deposited on a glass substrate to serve as the bottom electrode. The top electrode is usually made of a layer of conducting metal (Au, Ag) or carbon. The device is classified as an n-i-p structure when the ETL layer is positioned on the front (light incident) side. Conversely, it adopts a p-i-n structure when the HLT is placed on the front side.[56] Generally, the PSC device architectures are classified into conventional and inverted planar configurations based on their stacking order. The two fundamental structural types are mesoscopic and planar. The mesoscopic structure typically adopts an n-i-p layout (Fig. 3a), while the planar structure can support both n-i-p and p-i-n configurations (Fig. 3b and c, respectively). Among them, the mesoscopic n-i-p structure demonstrated the highest PCE due to its minimal hysteresis in the current–voltage (*J*–*V*) characteristics.[100] The architecture of a FPSC device closely mirrors that of its rigid counterpart. However, FPSCs use a flexible plastic substrate such as poly(ethylene terephthalate) (PET) or poly(ethylene naphthalate) (PEN), which is coated with a thin film of ITO to serve as the transparent conducting electrode.

3.1 High-quality perovskite films

As described in the previous section, PSC devices are composed of a perovskite thin film sandwiched between an ETL and an HTL (Fig. 3). The quality of the ETL and HTL interfaces and the perovskite thin film plays an important role in achieving an overall high performance in the assembled devices.[101] One of the main obstacles in the fabrication of high-efficiency FPSCs on plastic substrates is the formation of high-quality perovskite films with a large grain size, low trap density, high coverage, and high crystallinity. Generally, perovskite films have poor film quality on flexible substrates due to the low surface energy of plastic substrates, poor wettability, and wrinkling.[102] In the last few years, various attempts have been devoted to developing highly efficient perovskite films at low temperatures such as spray coating, spin coating, and squeegee coating.[103] In the

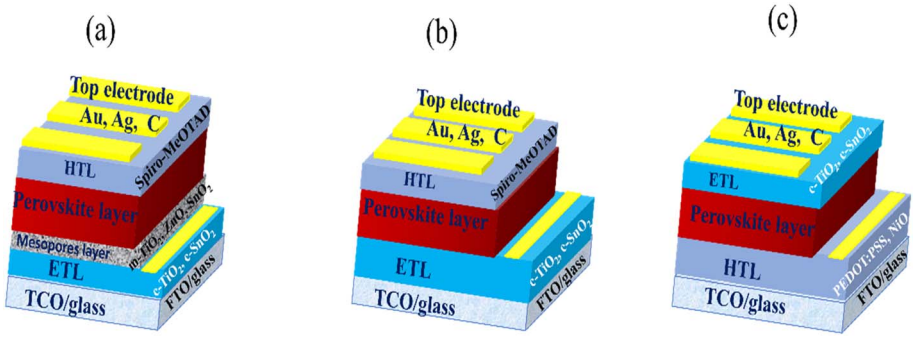

Fig. 3 Configuration of the PSC device; (a) n-i-p mesoscopic, (b) n-i-p planar, and (c) p-i-n planar PSC structures. Reprinted with permission from ref. 56. Copyright 2018, Royal Society of Chemistry.

following sections, the low-temperature techniques will be discussed.

3.1.1 Low-temperature one-step solution deposition method. This is a simple solution-processing technique in which all the perovskite precursors are mixed in a single solution, spin-coated on the substrate, and finally subjected to thermal annealing.[104] As presented in Fig. 4, the methylammonium ($CH_3NH_3^+$) or ethylammonium ($CH_3CH_2NH_3^+$) precursors combined with metal halide (PbX_2) components are deposited onto the substrates in either stoichiometric (1 : 1) or non-stoichiometric (*e.g.*, 3 : 1) molar ratios. Then, the deposited films are thermally treated at low temperatures to induce the crystallization of the perovskite layer.[105] For instance, Yang *et al.*[106] deposited a mixture of methylammonium iodide (MAI; CH_3NH_3I) solution and $PbCl_2$ in a 3 : 1 molar ratio onto TiO_2-coated ITO substrates *via* the spin-coating technique at room temperature. The assembled planar device fabricated without anti-reflective layers achieved an average PCE of 16.6%. The high performance, simplicity, and lower fabrication temperature demonstrate the potential for the large-scale production of perovskite films. However, multiple processing parameters such as the spin-coating speed, annealing temperature, duration, ambient humidity, and choice of solvent must be carefully controlled to produce high-quality perovskite layers. Grätzel *et al.*[107] investigated the effect of annealing temperature on the $CH_3NH_3PbI_3$ film produced *via* a one-step spin coating technique. As shown in the SEM images (Fig. 4a–c), an increase in the temperature from 60 °C to 100 °C significantly improved the film uniformity. However, a further increase in temperature led to the formation of large, non-uniform crystalline islands due to the rapid crystallization at multiple nucleation sites, resulting in a disrupted film morphology (Fig. 4d–g). Among them, the film annealed at 100 °C exhibited the most uniform morphology and achieved the highest performance (Fig. 4i). The low-temperature annealing process is particularly advantageous for producing uniform perovskite layers on flexible plastic substrates. Additionally, the film thickness is influenced by the spin-coating speed and time, and a thickness of ≈0.3 μm has been reported as sufficient for effective light absorption.

Besides controlling the morphology, the choice of solvent is also important, given that it affects the solubility of the precursors and the formation of intermediate phases.[108,109] The commonly used organic solvents include dimethylformamide (DMF), dimethyl sulfoxide (DMSO), methyl-2-pyrrolidinone

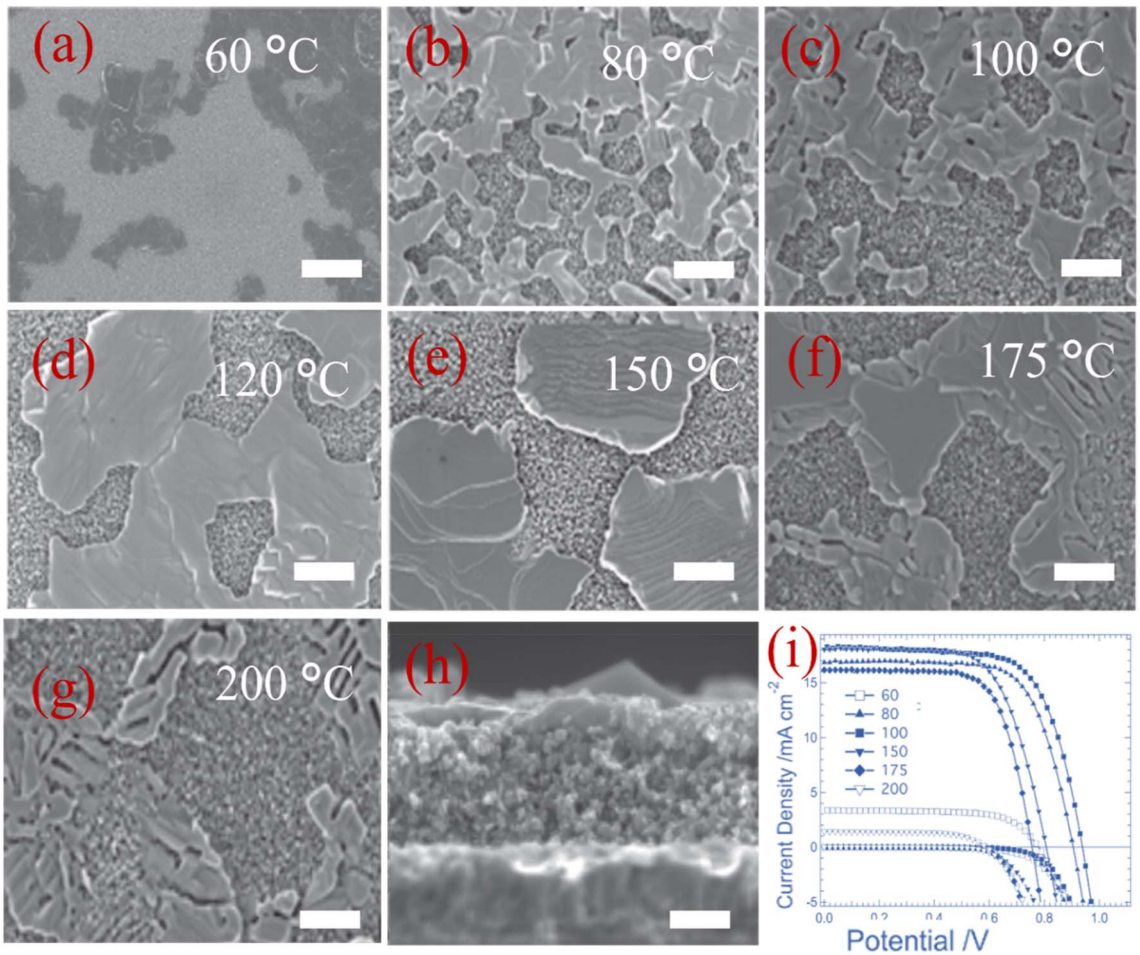

Fig. 4 (a–g) SEM of perovskite films deposited onto m-TiO_2 films, (h) cross sectional SEM image at 150 °C, and (i) *J*–*V* curves of the assembled FPSC devices. Reprinted with permission from ref. 107 Copyright 2014, Wiley-VCH.

(NMP), γ-butyrolactone (GBL), and toluene, which are utilized individually or as mixtures.[110–113] For example, Seok *et al.*[114] utilized a mixed solvent of GBL/DMSO and toluene drop-casting method to prepare homogenous and dense perovskite layers of CH_3NH_3I–PbI_2–DMSO intermediate phase. The assembled device achieved a PCE of 16.2%.

3.1.2 Low-temperature two-step solution deposition method. Despite the simplicity of the one-step approach and its popularity for the preparation of perovskite layers, the possibility of chemical reactions of the perovskite precursors can influence the quality of the resulting perovskite film, and thus the overall performance of the assembled devices. Moreover, the difficulty in controlling the morphology results from the uncontrollable nucleation and crystal growth, which is still a big challenge.[59] Therefore, developing alternative low-temperature two-step deposition methods has become necessary.

The two-step method is an alternative strategy that was very well-liked in the early stage of perovskite research. It involves depositing two precursors flowed by thermal annealing.[59] In this approach, a PbI_2 precursor is first deposited onto the conductive side of the substrate, followed by exposure to a CH_3NH_3I solution.[115,116] Fig. 5 illustrates the differences between the low-temperature one-step and two-step methods.[117] Generally, the two-step method yields an improved perovskite morphology and higher performance than that made using the one-step process.[59,118] This technique was first introduced by Mitzi *et al.*,[119] where a PbI_2 film was immersed in a CH_3NH_3I solution.

Due to its simplicity and reproducibility, the two-step deposition method has been widely adopted for the fabrication of PSC devices.[120] For instance, Huang *et al.*[121] successfully prepared pin-hole-free $CH_3NH_3PbI_3$ perovskite layers using a solution process by sequentially spin-coating PbI_2 and CH_3NH_3I layers (Fig. 6a). The PbI_2 and CH_3NH_3I precursors were dissolved in DMF and 2-propanol, respectively. Then, the resulting perovskite films were heated at 100 °C for varying durations. As shown in the SEM images in Fig. 6b–d, the perovskite film exhibited enhanced continuity compared to that prepared from premixed precursors. The assembled FPSC device showed a PCE of 15.4%, outperforming the devices fabricated by the interdiffusion method (14.5%). This demonstrates that the two-step deposition method has potential for the fabrication of efficient and low-cost perovskite layers at low temperatures. However, the incomplete conversion of PbI_2 and the uncontrolled configuration of the perovskite crystals are the main challenges.[122] Thus, to address these issues, great efforts have focused on improving the morphology and enhancing the conversion of PbI_2. The use of additives such as polymers, inorganic acids, and solvents has been proven to be an effective strategy for improving the quality of perovskite films.[123–125] Various organic polymers have been successfully utilized as additives.[126] For instance, Su *et al.*[127] reported that introducing 1wt% poly(ethylene glycol) (PEG) into the perovskite precursors enhanced the PCE of the assembled device by 25% (Fig. 6i). This improvement was assigned to the better control of the crystal size and aggregation (Fig. 6e and f). Moreover, PEG exhibits strong interactions with perovskite molecules, which enhances the moisture resistance, and consequently improves the long-term stability of the devices.

Inorganic acids such as hydroiodic acid (HI), hydrochloric acid (HCl), and hydrobromic (HBr) have also been employed as additives to significantly enhance the overall performance of PSCs.[123] The beneficial roles of these acids can be summarized as follows:[123] (i) they increase the solubility of the precursors, (ii) they prevent decomposition of the perovskite by converting elemental iodine into iodide ions, and (iii) they facilitate the formation of a pre-crystallized intermediate through interaction with the PbI_2 precursor, which is crucial for improving the grain size and crystallinity of the resulting perovskite film. Several studies have demonstrated the effectiveness of these additives. For example, Wen *et al.* used HI acid as an additive in an isopropanol (IPA) solution of CH_3NH_3I during the two-step spin-coated method to fabricate high-quality $CH_3NH_3PbI_3$ perovskite films. Increasing the HI concentration led to larger perovskite grain sizes. As presented in the SEM image (Fig. 7a–d), the film prepared with 0.004 vol% HI/IPA exhibited the most uniform and largest grain size. The assembled PSC device achieved a PCE of 18.21% (Fig. 7e). Similarly, Lu *et al.* reported that the addition of HI successfully enhanced the sensitivity of the perovskite particle sizes to the precursor (CH_3NH_3I/PbI_2) molar ratio.[128] Using a one-step spin-coating process, they fabricated a $CH_3NH_3PbI_3$ film with full surface coverage and high crystallinity. The assembled planar device displayed a PCE of 19.29%, highlighting the effectiveness of HI in optimizing the film quality and device performance. Recently, Wu *et al.*[129] demonstrated that water can serve as a promising additive in the perovskite precursors. In their study, a small amount of water was introduced in the PbI_2/DMF solution to investigate its effects on the properties of PbI_2 in the perovskite films fabricated using the two-step method. The resulting perovskite films were exceptionally pure, smooth, and dense, with no visible pinholes. This improvement facilitated the formation of a high-quality, pinhole-free perovskite layer with larger grain sizes and fewer defects, leading to an enhanced PCE of 18% in the inverted PSC device. These findings underscore the significant

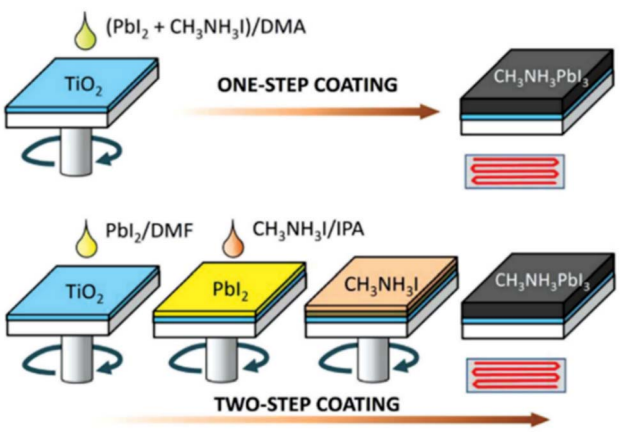

Fig. 5 Fabrication of $CH_3NH_3PbI_3$ films *via* one-step and two-step spin-coating techniques. Reprinted with permission from ref. 117 Copyright 2014, AIP Publishing.

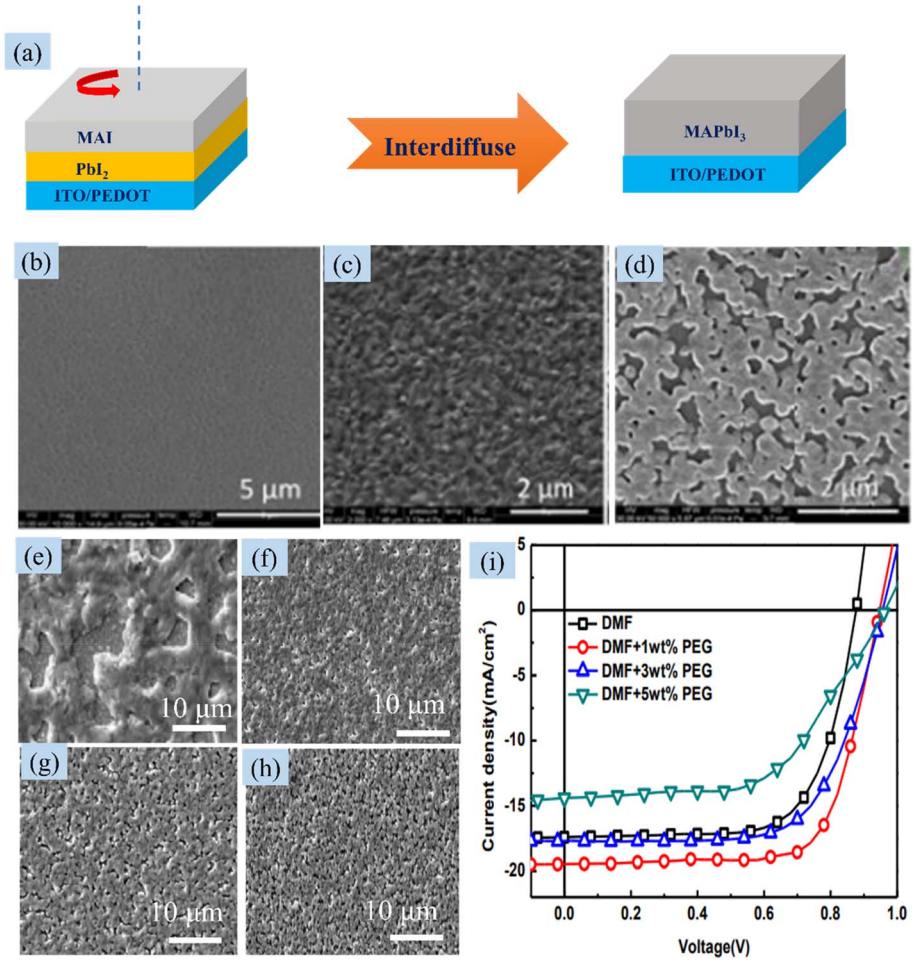

Fig. 6 (a) Scheme of the preparation of the perovskite layer *via* the interdiffusion method. SEM images of (b) the spun coated stacked PbI_2 layer, (c) annealed $CH_3NH_3PbI_3$ perovskite layers prepared by the interdiffusion method, and (d) annealed $CH_3NH_3PbI_3$ perovskite layers prepared using spun premixed precursors. Reprinted with permission from ref. 121 Copyright 2014, Royal Society of Chemistry. SEM images of perovskite films with (e) 0 wt% PEG, (f) 1 wt% PEG, (g) 3 wt% PEG, and (h) 5 wt% PEG. (i) *J*–*V* of the devices with pristine and *x* wt% of PEG additive. Reprinted with permission from ref. 127 Copyright 2015, American Chemical Society.

role of water in improving the perovskite film quality, and consequently the overall performance of inverted PSCs. Similarly, Meng *et al.* employed the two-step spin-coating method to fabricate $FA_xMA_{1-x}PbI_{2.55}Br_{0.45}$ perovskite layers by adding DMF to the FAI/MAI/IPA solution.[130] According to the SEM images (Fig. 7f–i), the addition of 2% DMF enhanced the conversion of the precursors to perovskite, leading to an improved film morphology, reduced crystal defects, and better charge-transfer efficiency. The assembled PSC device achieved a PCE of 20.1% (Fig. 7j), demonstrating both high efficiency and low processing temperature, which are ideal for the fabrication of FPSCs. Furthermore, Yang *et al.*[76] revealed that the use of dimethyl sulfide (DS) significantly slowed the perovskite crystallization process, allowing more controlled film formation. The assembled FPSC device is presented in Fig. 7k, and its cross section image is in Fig.7l. The resulting perovskite films exhibited larger crystal grains and enhanced stability (Fig. 7m and n), contributing to a maximum PCE of 18.40% in the corresponding FPSC devices (Fig. 7o). These results highlight the effectiveness of solvent engineering in optimizing the perovskite film quality and device performance.

3.1.3 Modified two-step deposition methods. Although the two-step process has demonstrated significant promise for producing high-performance PSCs, the perovskite thin films produced using this technique encounter several difficulties, including an uneven morphology and insufficient PbI_2 conversion to perovskite. Thus, to enhance the PbI_2 conversion and improve the morphology of the resulting perovskite films, several modified techniques have been developed. Liu *et al.* introduced a two-step deposition method that incorporates thermal evaporation for the formation of PbI_2 precursor films. This approach enables precise control of the PbI_2 film thickness, which is crucial for optimizing the film quality and device performance. Additionally, Yang *et al.*[132] fabricated high-quality polycrystalline perovskite films using a low-temperature vapor-assisted solution process (Fig. 8a). In their experiment, PbI_2 was first spin-coated onto the substrate, and then a layer of CH_3NH_3I powder was applied on top. The stacked layers were subsequently annealed at 150 °C. According to the SEM image

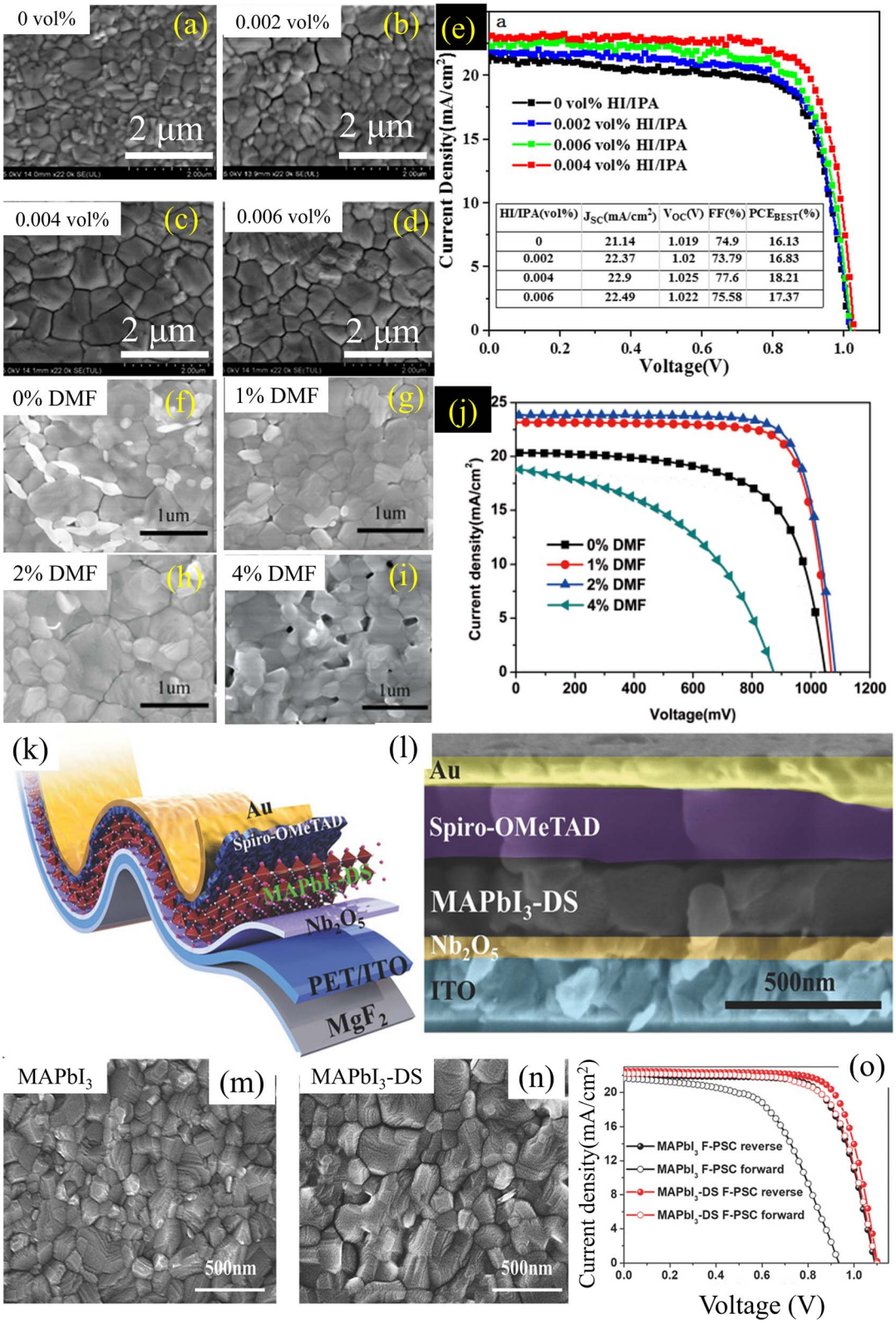

Fig. 7 (a) SEM images of $MAPbI_3$ film prepared by two-step spin-coating deposition with (a) 0, (b) 0.002, (c) 0.004, and (d) 0.006 vol% HI/IPA. (e) *J*–*V* curves of the FPSCs. Reprinted with permission from ref. 131. Copyright 2018, AIP Advances. (c) SEM image of perovskite films obtained by different ratios of DMF in IPA, (f) w/o DMF, (g) 1% DMF, (h) 2% DMF, (i) 4%DMF. (j) *J*–*V* curves of the FPSCs. Reprinted with permission from ref. 130. Copyright 2017, American Chemical Society. (k) Scheme of the FPSC device, (i) cross-sectional SEM image of the device. SEM image of $MAPbI_3$ films (m) without and (n) with DS additive, and (o) *J*–*V* curves of the FPSCs. Reprinted with permission from ref. 76. Copyright 2018, Wiley-VCH.

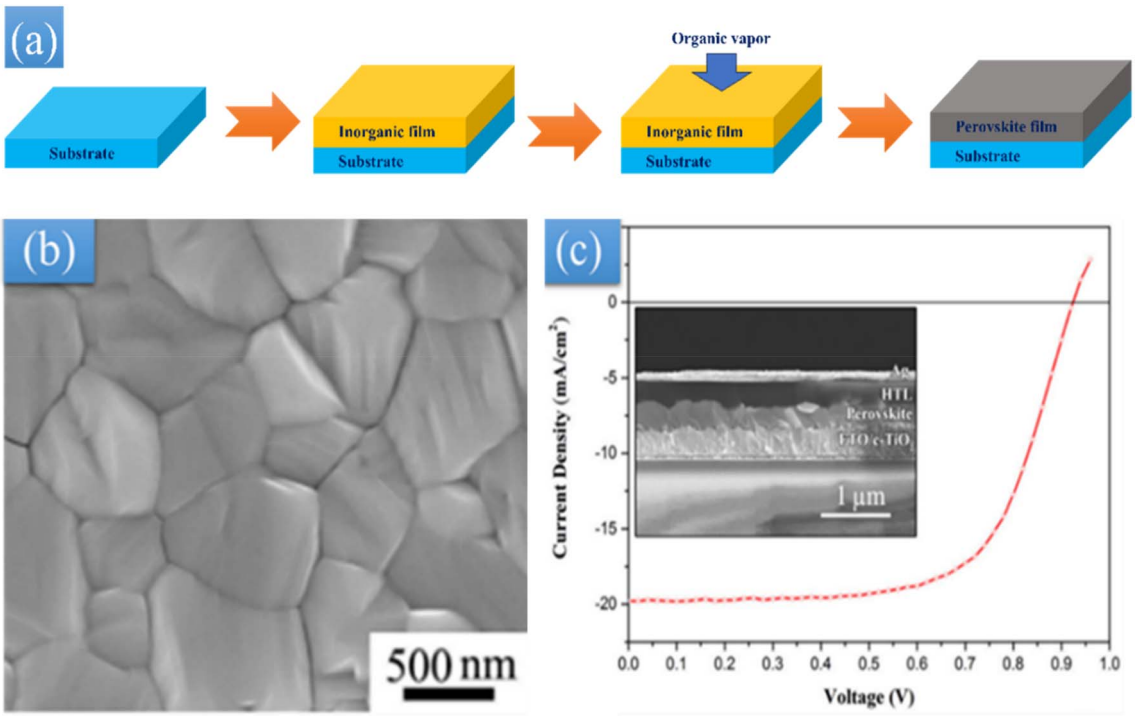

Fig. 8 (a) Scheme for the formation of the perovskite film through the vapour-assisted solution method, (b) SEM image of the perovskite film at 150 °C for 4 h, and (c) *J*–*V* curve of PSCs based on the as-prepared perovskite films (inset is the cross-sectional SEM of the FPSC). Reprinted with permission from ref. 132. Copyright 2014, American Chemical Society.

(Fig. 8b), the resulting perovskite films exhibited large grain sizes (≈1 μm), uniform surface coverage, and low surface roughness. The related fabricated planar heterojunction PSC achieved a PCE of 12.1% (Fig. 8c), demonstrating the potential of vapour-assisted techniques for improving the film quality under low-temperature processing conditions.

In a separate study, the same research group employed magnetron sputtering to deposit amorphous TiO_2 (am-TiO_2) as the ETL for FPSCs.[133] Subsequently, PbI_2 was deposited onto the substrate using a vacuum evaporation process, while an aluminium plate was coated with a layer of CH_3NH_3I powder. The two layers were placed face-to-face and annealed at 150 °C. This method yielded a perovskite film with full surface coverage. The resulting FPSC, with an active area of 410 mm^2, achieved a PCE of 15.07%, demonstrating the effectiveness of vacuum-based processing techniques for large-area flexible devices.

3.2 Low-temperature interface layers

The interface layers known as ETLs and HTLs also play a critical role in determining the overall performance of the constructed devices. The ideal materials for these layers should exhibit high charge carrier mobility, high transparency in the visible spectrum, and energy levels matching that of the perovskite absorber. In the following sections, we present the recent advances in the development and application of ETLs and HTLs for FPSCs.

3.2.1 Electron transport layers (ELTs).

In PSCs, the ETL is a key component and usually sandwiched between the light-harvesting absorber (perovskite layer) and the top electrode (FTO and ITO) to extract electrons efficiently and block holes. To date, many materials have been employed as ETLs.[134] ETLs should have excellent light transmittance, low trap density, and energy level matching the perovskite material. There are many materials have commonly been used as ETLs. TiO_2 is commonly used as an ETL in PSCs because its conduction band aligns well for effective electron transfer from the perovskite layer, while its deep valence band helps block hole carriers.[135–138] The conventional technique for preparing TiO_2 thin films is spray pyrolysis or spin-coating, followed by sintering at high temperatures (≈450 °C), which yields a dense and high crystalline structure. However, this high temperature limits the applicability of TiO_2 in FPSCs.[139,140] Hence, many attempts have been made to develop low-temperature methods for the fabrication of TiO_2 layers to realize FPSCs. For example, Dürr *et al.* developed a lift-off technique to transfer pre-sintered porous TiO_2 layers onto flexible substrates. The transferred layers retained their original electrical properties.[141] However, this method is relatively complex and requires several auxiliary tools (Fig. 9a), limiting its practicality. An alternative low-temperature strategy involved a hydrothermal process, where mechanically stable mesoporous TiO_2 films were fabricated at 100 °C using an aqueous paste composed of nanocrystalline TiO_2 powder and titanium salts. The FPSCs exhibited a PCE of 2.3%.[142] A significant improvement was achieved by Kim *et al.*,[143] where a 20 nm-thick amorphous TiO_2 layer was deposited on a PEN/ITO flexible

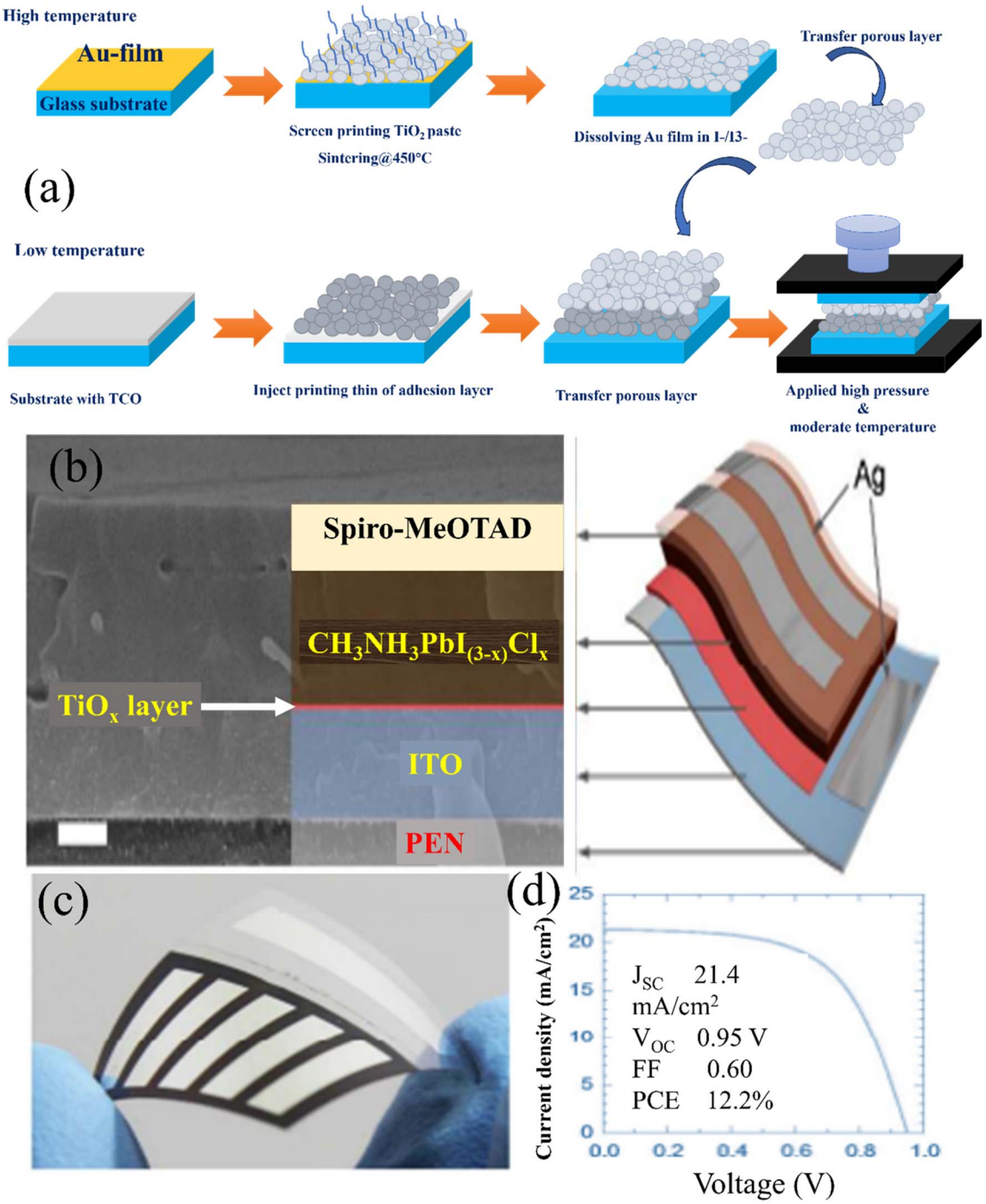

Fig. 9 (a) Lift-off and transfer process. Reprinted with permission from ref. 141. Copyright 2005, Nature. (b) Cross-sectional SEM image of FPSC and scheme of the flexible device, (c) photograph of FPSC, and (d) *J*–*V* curve of the best device. Reprinted with permission from ref. 143. Copyright 2015, Royal Society of Chemistry.

substrate at 80 °C *via* plasma-enhanced atomic layer deposition (PEALD). The constructed FPSCs (Fig. 9c) exhibited a PCE of 12.2% (Fig. 9d). After 1000 bending cycles with a bending radius of 10 mm, the PCE loss was only 5%. Another approach for producing very dense amorphous TiO_2 (am-TiO_2) films on PET/ITO substrates used as ETLs at room temperature was the magnetron sputtering technique reported by Yang *et al.*[133] The resulting am-TiO_2 exhibited a Fermi level of 4.15 eV, which is favorable for efficient electron injection from the perovskite layer. The PCE of the assembled FPSC device was 15.07%.

In parallel, significant efforts have been directed toward developing simpler and more scalable low-temperature methods.[144] For example, Yang *et al.*[144] employed 1-benzyl-3-methylimidazolium chloride as a solid-state ionic liquid (ss-

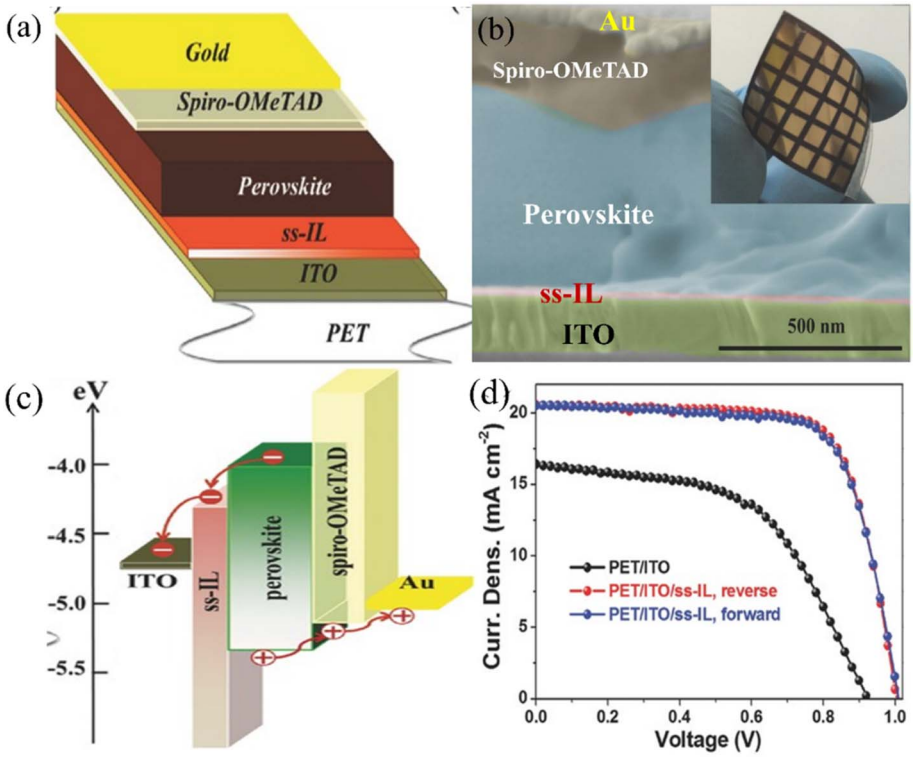

Fig. 10 (a) Device structure, (b) cross-sectional SEM of FPSC with ss-IL as ETL, (c) energy-level, and (d) *J*–*V* curve of the best device. Reprinted with permission from ref. 144. Copyright 2016, Wiley-VCH.

IL) to form ETLs at low temperatures. This approach offers a facile and potentially low-cost alternative for the fabrication of the ETL in FPSCs, as shown in Fig. 10a and b. The energy-level diagram of the device is presented in Fig. 10c. According to the scanning Kelvin probe microscopy (SKPM) measurements, the work function (WF) of ITO decreased from 4.67 eV to 4.32 eV after coating with the ss-IL layer. Similar reductions were observed from 4.41 to 4.02 eV for FTO, 5.10 to 3.93 eV for Au, and 4.60 to 3.84 eV for Ag. These results confirm that the ss-IL coating effectively modified the WF of both the metal oxides (ITO and FTO) and metals (Au, Ag). According to the energy-level alignment, the cathode/perovskite interface lowers the WF of the ss-IL layer, lowering the energy barrier for electron extraction, and thus improving the charge collection. Furthermore, the broad bandgap of ss-IL (~4.59 eV) served as an effective hole-blocking layer, reducing the hole diffusion into the ITO and enhancing the fill factor (FF) and J_{SC}. The broad band gap, high electron mobility, and well-aligned the WF of ss-IL-based ETLs contributed to an enhanced PCE to 16.09% (Fig. 10d).

Jeong *et al.*[145] used a UV-assisted solution process to prepare Nb-doped TiO_2 (UV-Nb:TiO_2) ETLs at low temperature (<50 °C). The prepared TiO_2 nanocrystals (NCs) stabilized with oleic acid spin-coated, and then treated with UV (Fig. 11a). After UV treatment, the prepared UV-TiO_2 displayed higher crystallinity, as indicated by the HR-TEM images (Fig. 11c and d). Due to its photocatalytic activity, the UV-treated TiO_2 thin-film (UV-TiO_2) degraded oleic acid, and thus the prepared TiO_2 NC film displayed highly uniform, high compact high transmittance (Fig. 11b) and better-blocking effect compared to that for TiO_2 film prepared at high temperature. Moreover, Nb doping enhanced the conductivity and improved the charge extraction by shifting the conduction band downward. As a result, the FPSCs using PEN/ITO and UV-Nb:TiO_2 achieved a PCE of 16.01%. Moreover, the assembled devices displayed higher stability even after 1000 bending cycles with a radius of 15 mm. Further enhancement was achieved by Yang *et al.*,[146] employing the sol–gel method for the preparation of a compact TiO_2 (c-TiO_2) ETL below 150 °C. The results confirmed that the c-TiO_2 ETL exhibited the best photoelectric performance with the concentration of TiO_2 precursor solution of 2 M and the annealing temperature of 150 °C for 30 min. The best PCE of the assembled FPSC on a PEN/ITO substrate was 6.11%, with good mechanical stability. Recently, Gu *et al.*[147] prepared TiO_2-doped carbon nanofibers (TiO_2/C NFs) *via* electrospinning as ETLs for FPSCs. The related constructed devices exhibited a PCE of 17.61%, with high mechanical stability, highlighting the promising application of TiO_2/C NFs in developing high-efficiency FPSCs.

Despite the great progress that has been achieved utilizing TiO_2 as ETLs in FPSCs, its lower electron mobility compared to conventional ETLs still a challenge.[144] As a result, intensive research has been devoted to developing alternative metal oxides with improved charge transport properties. Among them, zinc oxide (ZnO) has been highlighted as a potential alternative ETL in FPSCs to replace the conventional TiO_2 due to its excellent properties such as higher electron mobility and

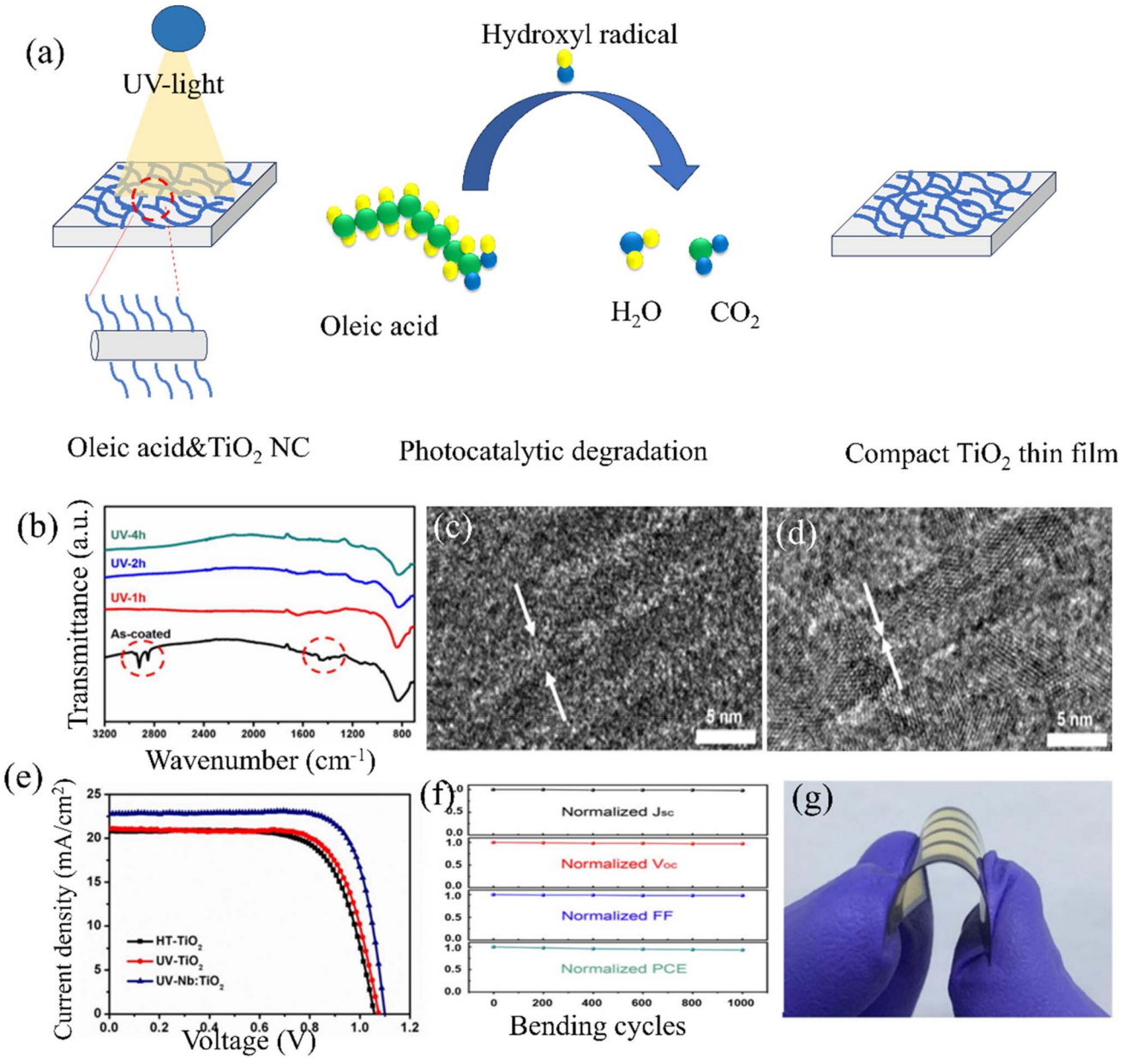

Fig. 11 (a) Scheme of the UV process for the formation of a compact TiO_2 thin film and (b) FTIR spectra of spin-coated TiO_2 thin films. HR-TEM images of oleic acid-capped TiO_2 NCs (c) before and (d) after UV treatment. (e) *J*–*V* curves of the FPSCs with various ETLs on FTO glass. (f) Normalized photovoltaic parameters of the FPSC device after bending with a radius of 15 mm for 1000 cycles. (g) Photograph of the FPSC based on with UV-Nb:TiO_2 ETL coated on a ITO/PEN substrate. Reprinted with permission from ref. 145. Copyright 2016, Elsevier.

easy processability from solution at low temperature without a sintering process.[148–150] The first work applying ZnO as the ETL in FPSCs was reported by Kumar *et al.*,[69] who utilized the chemical bath deposition (CBD) method to prepare a ZnO compact layer. The FPSCs prepared using the ZnO ETL showed a PCE of 2.62% on a flexible PET/ITO substrate. Higher improvements were achieved by Liu and Kelly,[148] where they deposited ZnO films onto ITO substrates using the spin-coating technique, and the whole the structure of device is presented in Fig. 12a, and its photograph is shown in Fig. 12b. According to the energy-level alignment shown in Fig. 12c, the photo-generated charge carriers within the perovskite layer can be efficiently separated, in which electrons can be transferred to the ZnO layer, while holes can move to the spiro-OMeTAD HTL. The device constructed on a flexible PET/ITO substrate displayed a PCE of 10.2% (Fig. 12d). Further enhancement was achieved by Chu *et al.*,[151] where they modified the surface quality and wettability of the ZnO ETL by an ionic liquid at room temperature (Fig. 12g and h). The modification greatly improved the charge mobility of the ZnO ETL and improved the crystallinity of the perovskite film. The perovskite film on the modified ZnO ETL (Fig. 12f) presented larger and more homogeneous grains with better crystallinity on the pristine substrate

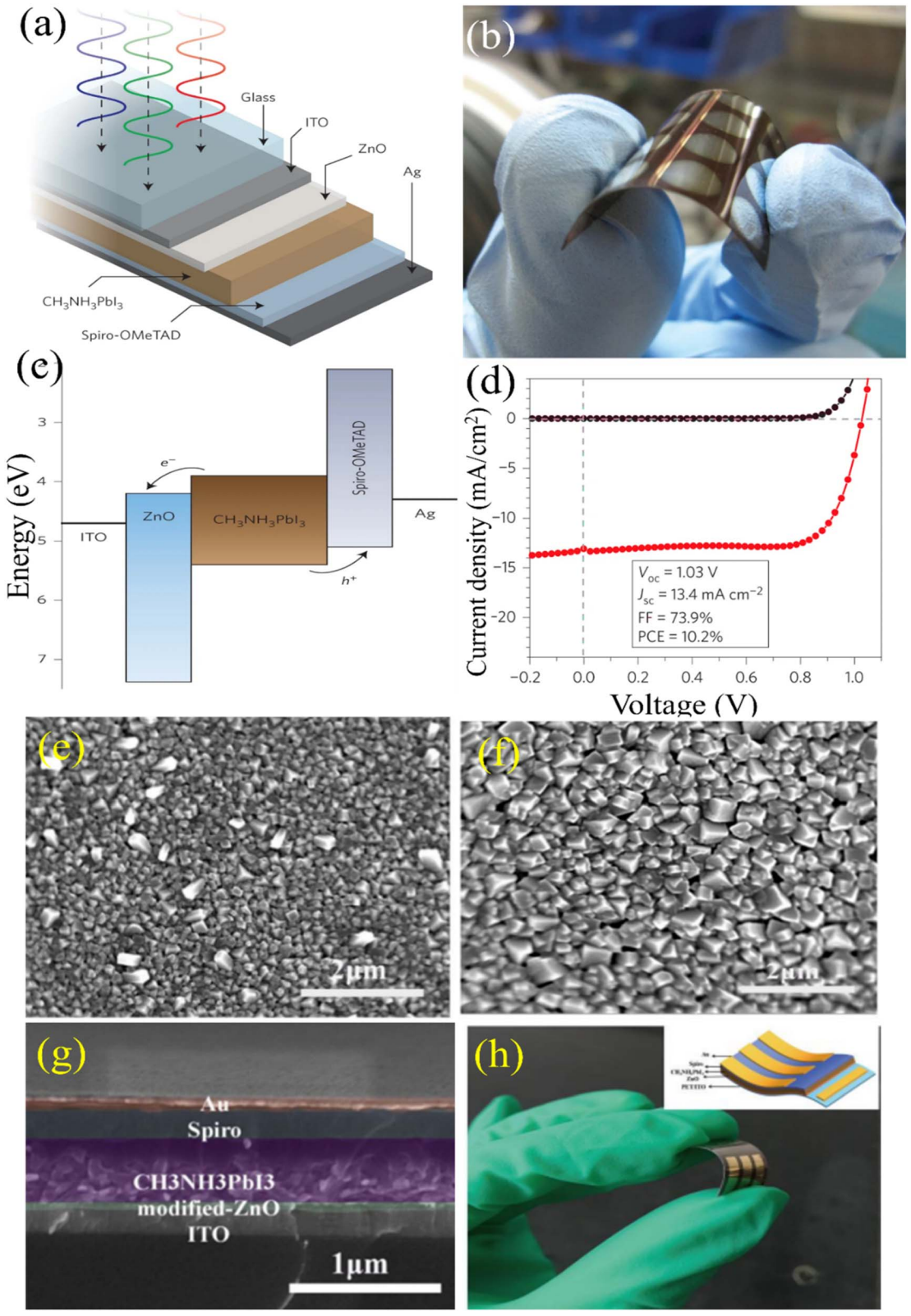

Fig. 12 (a) FPSC device structure, (b) photograph of ITO/ZnO/$CH_3NH_3PbI_3$/spiro-OMeTAD/Ag device on a PET substrate, (c) energy levels of the different parts of the device, and (d) *J*–*V* curves of the FPSC under illumination/in the dark. Reprinted with permission from ref. 148. Copyright 2013, Springer Nature. SEM image of the $MAPbI_3$ perovskite film on (e) pristine ZnO ETL, (f) modified ZnO ETL, (g) cross-sectional SEM image and (h) photograph of the assembled FPSC. Reprinted with permission from ref. 151. Copyright 2018, Elsevier.

(Fig. 12e). Thus, the assembled device on a flexible substrate displayed a PCE of 12.1%.

SnO_2 is another promising alternative ETL to TiO_2. Typically, SnO_2 exhibits a wide optical band gap (3.6–4.0 eV), high transparency, high mobility, excellent chemical stability, and easy low-temperature preparation.[152] To date, much research has been done on utilizing SnO_2 as the ETL in FPSCs. For example, Park *et al.*[153] developed an Li-doped SnO_2 (Li:SnO_2) ETL at low temperature. The doped Li remarkably enhanced the conductivity and lowered the CBM of SnO_2, which enhanced the electron injection and transport from the perovskite layer. The assembled FPSC achieved a PCE of 14.78%, with higher mechanical durability after 500 bending cycles at a radius of 10 mm, which showed a retention of 91.9% of the initial values. Furthermore, Shi *et al.*[152] developed a simple method to synthesize SnO_2 nanoparticles (NPs) at room temperature, followed by spin coating on a flexible substrate, and finally the SnO_2 thin-film was treated with UV-ozone. The assembled FPSC device displayed a PCE of 15.27%. Similarly, SnO_2 films were fabricated using plasma-enhanced atomic layer deposition (PEALD) for use as ETLs in FPSCs.[154] Notably, water vapor treatment significantly enhanced the charge transport properties of the SnO_2 layer, leading to a PCE of 18.36% for the assembled devices. A higher performance was achieved by Zhong *et al.*,[155] where they prepared metal ion-modified SnO_2 (M-SnO_2) *via* a hydrolysis process and coated it on a flexible substrate at room temperature to prepare an RT-SnO_2 ETL-based FPSC (Fig. 13a). Doping SnO_2 with metal ions remarkably enhanced the charge extraction and suppressed the interfacial charge recombination. As a result, the constructed FPSCs achieved a PCE of 19.3% (Fig. 13b and c), together with outstanding strong mechanical stability (Fig. 13d). Further enhancement was achieved by Paik *et al.*,[156] where they prepared an SnO_2–TiO_2 hybrid as the ETL. The related fabricated FPSC device with an SnO_2–TiO_2 ETL displayed strong mechanical reliability due to its strong adhesion to the substrate. The FPSC device with the SnO_2–TiO_2 ETL achieved a PCE of 21.02%. Recently Long *et al.*[157] achieved a higher performance by utilizing SnO_2 embedded in gold nanoparticles (Au NPs) ETL. The presence of Au NPs significantly improved the conductivity and electron mobilities of the ETL, which promoted electron extraction and transport, resulting in a decrease in charge recombination at the ETL/perovskite interface. Therefore, the assembled FPSC device with the SnO_2 ETL embedded with Au NPs showed a PCE of 23.08%, which is higher than the FPSCs with the pristine SnO_2 ETL (21.65%).

In addition to metal oxides, a variety of organic materials has been utilized as ETLs, owing to their ease of preparation at low temperatures; an essential requirement for the fabrication of flexible devices. Fullerene-based materials have emerged as promising ETLs in FPSCs due to their excellent electron mobility, solution-processability, and potential for interface engineering.[158] Recent advancements have focused on enhancing the performance and stability of these materials through structural modifications and hybrid compositions.[159] For example, Yoon *et al.*[160] fabricated a hysteresis-free planar $CH_3NH_3PbI_3$ PSC with vacuum-processed C_{60} ETL deposited on a PEN/ITO substrate at room-temperature without the hole blocking layer (Fig. 14a). They reported that the C_{60} layer deposited on perovskites reduced the photocurrent hysteresis, and thus enhanced the overall efficiency of the hysteresis-free FPSC, achieving a PCE of 16.0% (Fig. 14b). The device retained 95% of its original power conversion efficiency after 100 bending cycles at a bending radius of 5 mm. However, after 1000 cycles, the efficiency dropped by 20% compared to its initial value (Fig. 14c). A further enhancement was achieved by

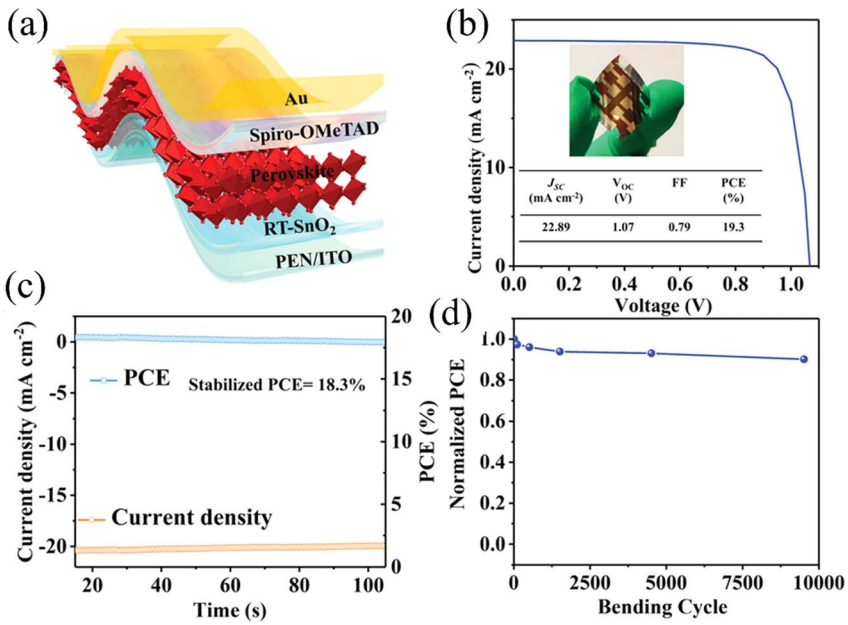

Fig. 13 (a) Scheme of the FPSC device, (b) *J*–*V* curve, (c) stabilized current density and PCE, and (d) normalized PCE as a function of bending cycles at a radius of 5 mm. Reprinted with permission from ref. 155. Copyright 2022, Wiley-VCH.

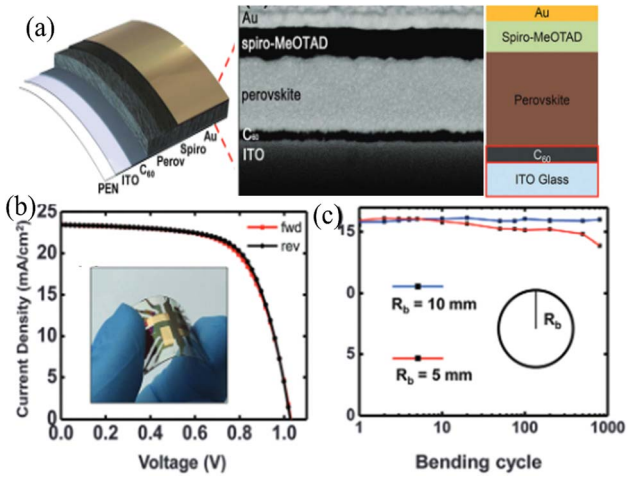

Fig. 14 (a) Scheme of the FPSC with a cross-sectional SEM image, (b) *J*–*V* curve, and (c) efficiency as a function of bending cycles with radii of 10 mm and 5 mm. Reprinted with permission from ref. 160. Copyright 2016, Royal Society of Chemistry.

Wang *et al.*,[161] where they highlighted the use of a carboxyl-functionalized fullerene, C_{60} pyrrolidine tris-acid (CPTA), as the ETLs in n-i-p planar FPSCs. CPTA forms a uniform film that covalently binds to the ITO substrate, reducing the hysteresis and improving the mechanical flexibility. Because CPTA is solution-processable, it supports the development of light-weight, FPSCs. The devices using ITO/CPTA/$CH_3NH_3PbI_3$/spiro-OMeTAD/Au structures on flexible substrates achieved a PCE of 17%. Recently, Hou *et al.*[162] reported that introducing a cross-linkable fullerene (FTAI) enhances the conductivity and elasticity of grain boundaries in tin-based perovskite films. The resulting devices exhibited a PCE of 14.91% and maintained 90% of their initial efficiency after 10 000 bending cycles, demonstrating excellent mechanical stability. Thus, these materials offer favorable energy level alignment and efficient electron extraction, making them attractive candidates for use in FPSCs.

3.2.2 Hole transport layers (HTLs). In FPSCs, the HTL is responsible for extracting holes from the perovskite layer and moving them to the electrodes. The efficient HTLs should

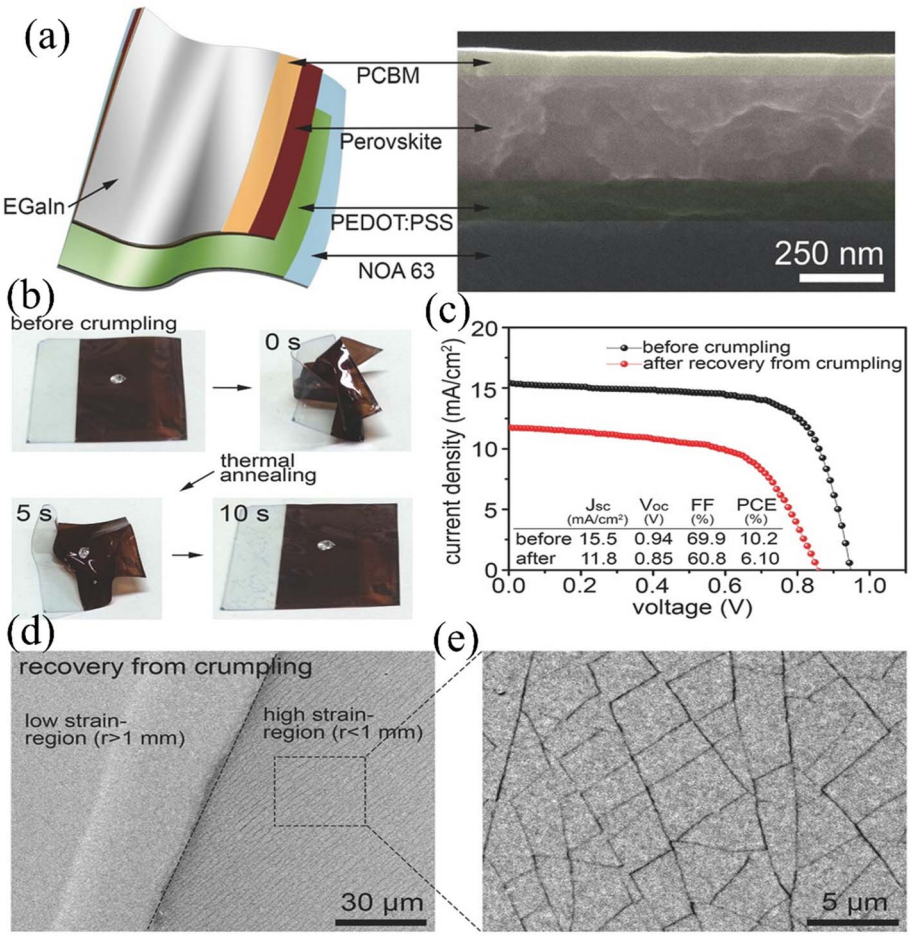

Fig. 15 (a) Scheme of the stacked layers on an NOA63 film and a cross-sectional SEM image of the device, (b) photographs of the device during the crumpling test, (c) *J*–*V* curves before crumpling and after shape recovery from crumpling test, (d) SEM and (e) magnified SEM images of the top surface after shape recovery from crumpling test showing regions of low strain and high strain. Reprinted with permission from ref. 90. Copyright 2015, Wiley-VCH.

possess some features, as follow:[163] (i) the valence band maximum (VBM; also known as the HOMO) of the HTLs is appropriate for the perovskite and electrode. This facilitates the rate of hole injection, thus enhancing the efficiency of f-PSCs. (ii) The materials of the HTL must be physically and chemically stable to avoid corrosion or degradation by oxygen and vapor penetrating through the flexible substrate. (iii) The HTL needs to be extremely compact to isolate the electrode from the perovskite layer. Spiro-OMeTAD is the most widely used material for HTLs due to its well-matched energy level with that of perovskites, low-temperature fabrication, and the high overall performance of the assembled FPSCs.[143,144] However, spiro-OMeTAD suffers from drawbacks such as high cost and relatively poor hole conductivity and mobility.[164,165] Consequently, great effort has been dedicated to finding alternative HTL materials.

Polymers offer numerous benefits as charge-transporting materials for flexible PSCs, such as great mechanical flexibility, customizable optoelectrical characteristics by adjusting their chemical structures, and low-temperature solution processability.[166] To date, many materials have been successfully utilized as HTL materials. Polymers display potential ability as HTLs due to their low-temperature solution processability, tunable optoelectrical properties, and high mechanical flexibility. Poly(3,4-ethylenedioxythiophene)–poly(styrenesulfonate) (PEDOT:PSS) is a promising candidate due to its high work function (WF), which is around 5.0 to 5.2 eV.[78,167] A device with the PET/ITO/PEDOT:PSS/perovskite/PCBM/Al structure demonstrated a PCE of 9.20%.[168] In further work by Pak *et al.*,[90] they deposited PEDOT:PSS on a flexible substrate polymer (Noland Optical Adhesive 63) to be utilized as the HTL for FPSCs with an inverted architecture (Fig. 15a and b). The capacity of the device to restore its shape after random crumpling is shown in Fig. 15c. It was discovered that following annealing on a hot plate for 10 s at 80 °C, the crumpled device was fully recovered. Fig. 15d and e demonstrate that the performance of the device deteriorated as a result of cracks created by particularly severe bending. There are two types of crumpled regions that can be distinguished by the degree of bending strains induced by random crumpling, low-strain ($r \geq 1$ mm) and high-strain ($r < 1$ mm) applied regions (Fig. 15d). Multiple cracks were discovered in the high-strain applied region, but no break was seen in the low-strain applied zone (Fig. 15e). The PCE of the assembled device before and after bending at a radius of 1 mm was 10.75% and 10.4%, respectively. After crumpling, the PCE decreased from its initial value of 10.2% to 6.1% upon crumpling recovery (Fig. 15c).

However, despite these tremendous advancements, the performance of PEDOT:PSS-based flexible PSCs is still limited due to some negative characteristics. (i) The PEDOT:PSS film has poor charge-transporting ability in the out-of-plane direction because it forms lamellar structures, (ii) its insufficient work function compared with the VBM of perovskite (−5.4 eV) results in energy loss at the PEDOT:PSS/perovskite interface, and (iii) PEDOT:PSS displays a strong acidic nature (pH ≈ 1), which degrade the device layers, and thus destroys the total performance.[169–171] Thus, its highly important to develop PEDOT:PSS-based HTLs or develop new polymeric HTLs for the further improvement of FPSCs. Doping PEDOT:PSS with other materials has shown promising potential to improve the

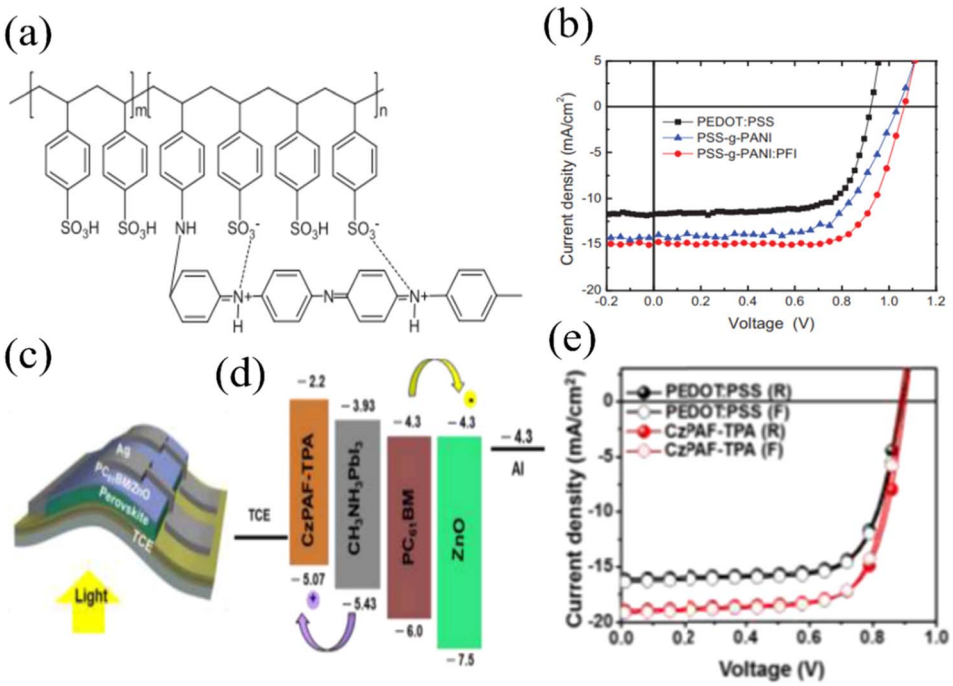

Fig. 16 (a) Chemical structure of PSS-*g*-PANI and (b) *J*–*V* curves of the devices with PEDOT:PSS, PSS-*g*-PANI, and PSS-*g*-PANI: PFI HTLs. Reprinted with permission from ref. 172. Copyright 2016, Wiley-VCH. (c) Flexible structure, (d) energy level, and (e) *J*–*V* curves of the FPSC with PEDOT:PSS. Reprinted with permission from ref. 173. Copyright 2017, Elsevier.

performance of the assembled FPSCs. For instance, Hu *et al.*[19] prepared nano-cellular-doped PEDOT:PSS (NC-PEDOT:PSS) HTL in FPSCs. They reported that the modification significantly enhanced the light absorption and charge transport. The related FPSC devices displayed a PCE of 12.32% on a large area of 1.01 cm^2 and outstanding flexural endurance.

One major cause of energy loss at the PEDOT:PSS/perovskite interface, which reduces the V_{OC}, is the relatively low WF of PEDOT:PSS (4.9–5.2 eV) compared to the perovskite VBM (~5.4 eV).[172] Thus, to overcome this, Lee *et al.* developed PSS-*g*-PANI, a water-soluble material that serves as an efficient HTL in FPSCs (Fig. 16a). The devices using PSS-*g*-PANI exhibited higher PCEs than that with PEDOT:PSS HTL (Fig. 16b).[172]

Recently, intense research has focused on replacing PEDOT:PSS with small molecules, organic polymers, and inorganic materials.[173,174] Based on their tunable photophysical properties and easy preparation at low temperatures, small organic molecules have received great interest as HTLs in FPSCs.[173] For example, *N*-(4-(9*H*-carbazol-9-yl)phenyl)-7-(4-(bis(4-methoxy-phenyl)amino)phenyl)-*N*-(7-(4-(bis(4-methoxyphenyl)amino)-phenyl)-9,9-dioctyl-9*H*-fluoren-2-yl)-9,9-dioctyl-9*H*-fluoren-2-amine (CzPAF-TPA) as the HTL demonstrated high hole mobility and an appropriate highest occupied molecular orbital (HOMO) energy level, as can be observed in Fig. 16d.[173] The structure of the flexible PEDOT:PSS-based FPSC device is presented in Fig. 16c. The *J*–*V* characteristics of the FPSCs with CzPAF-TPA and PEDOT:PSS as dopant-free HTMs are displayed in Fig. 16e. The assembled FPSC device displayed a PCE of 12.46%. Alternatively, poly(triaryl amine) (PTAA) as the HTL significantly enhanced the V_{OC} of the FPSC device with a structure of poly-ethylene naphthalate (PEN)/ITO/ZnO/$MAPbI_3$ perovskite/PTAA/Au. The PCE of the FPSC was 15.6%.[175]

Conjugated polyelectrolytes are a novel class of interface materials consisting of conjugated side chains with ionic functional groups and backbones. The strong solubilities of these materials in polar solvents allow them to be employed in

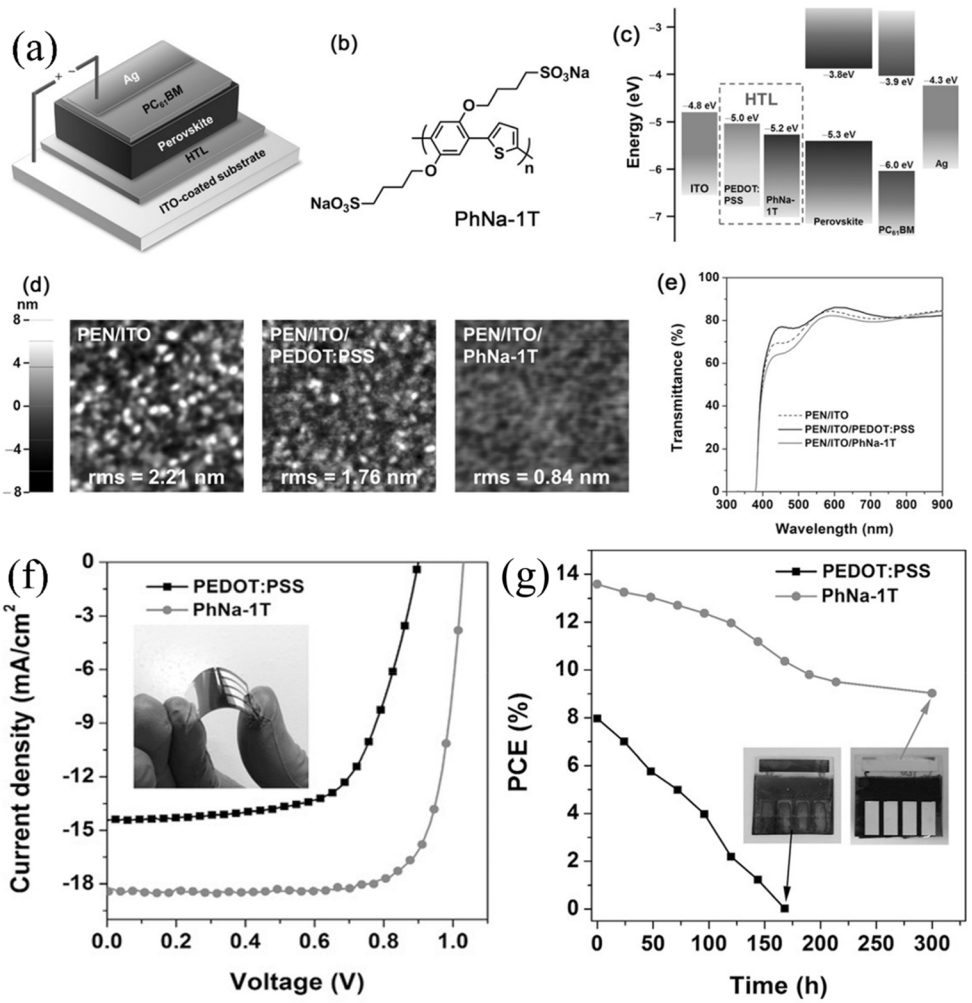

Fig. 17 (a) FPSC architecture, (b) chemical structure of PhNa-1T, (c) energy diagrams, (d) AFM images of PEDOT:PSS and PhNa-1T films deposited on ITO/PEN, (e) transmission spectra of PEDOT:PSS and PhNa-1T films deposited on ITO/PEN, (f) *J*–*V* curves of the FPSCs with PEDOT:PSS and PhNa-1T HTLs, and (g) PCE changes in the FPSCs with PEDOT:PSS and PhNa-1T HTLs as a function of exposure time to ambient atmosphere. The inset shows photographs of the corresponding degraded FPSCs. Reprinted with permission from ref. 176. Copyright 2019, Wiley-VCH.

low-temperature solution procedures to produce thin films on surfaces. Conjugated polymers have been successfully utilized as HTLs for FPSCs. For instance, Jo *et al.*[176] used 1,4-bis(4-sulfonatobutoxy)benzene and thiophene moieties (PhNa-1T) (Fig. 17a) as HTLs in inverted FPSCs (Fig. 17b). The incorporation of PhNa-1T into the HTL of the FPSC device significantly enhanced the charge extraction from the perovskite absorber to the HTL, suppressing charge recombination in the bulk perovskite and HTL/perovskite interface. Accordingly, the assembled FPSC device with PhNa-1T displayed a PCE of 14.7% (Fig. 17f), as well as high stability under ambient conditions (Fig. 17g).

Inorganic materials also offer a promising alternative to PEDOT:PSS, owing to their excellent chemical stability, low production costs, and high mobility.[177] Among these metal oxides, NiO_x displayed promising ability as an HTL material due to its broad bandgap, deep valence band edge (~5.4 eV), and high stability. However, the use of NiO_x as the HTL in flexible devices is limited given that the typical NiO_x layers require high temperatures (>300 °C) to prepare high-quality thin films.[178,179] Thus, great efforts have devoted to overcoming this limitation.[180] NiO_x nanoparticles are usually dispersed in water and coated on a flexible substrate through solution methods such as spin-coating and spray-coating techniques. For example, Yin *et al.*[177] reported that an NiO_x nanoparticle solution spin-coated onto ITO-PEN substrates at 130 °C for 20 min in air could be sufficiently utilized as the HTL for FPSCs (Fig. 18b). The prepared FPSC device displayed a PCE of 13.43% (Fig. 18a), which is close to that achieved with the rigid device using an NiO_x film prepared at higher temperature (16.47%). This indicates the potential ability of the NiO_x films as HTLs for FPSCs. Furthermore, Ye *et al.*[181] deposited NiO_x nanoparticles onto a PET substrate *via* a low-temperature soft-cover deposition (LT-SCD) method to be utilized as HTL for FPSCs. The assembled FPSC device achieved a PCE of 15.3%. A higher performance was achieved by Najafi *et al.*[182] In this study, NiO_x and ZnO nanoparticle films were employed at room temperature as the HTL and ETL, respectively. The assembled FPSC by the flexible PEN/thin film barrier/ITO substrates displayed PCEs of 16.6% (Fig. 18d and e). More interestingly, about 85% of its output efficiency is retained after 1000 h.

In conclusion, because of their exceptional solution processability at room temperature, NiO_x shows promise as HTLs for FPSC devices. Nevertheless, low-temperature processing frequently results in the development of defects, which significantly reduce the overall performance of the device and the quality of the film. Thus, great attempts have been made to alter NiO_x nanoparticles to enhance the overall performance of FPSCs. For instance, Wang *et al.*[183] passivated the surface defects of NiO_x NPs using benzoic acid self-assembled monolayers (SAMs). This study demonstrated that 4-bromobenzoic acid could effectively perform the function of surface passivation. This SAM layer decreased the trap-assisted recombination, minimized the energy offset between the NiO_x NPs and perovskite, and modified the HTL surface wettability. Thus, the perovskite crystallization was improved and more stable PSCs were produced with an improved overall performance. The fabricated FPSCs on a PET substrate displayed a PCE of 16.2%.

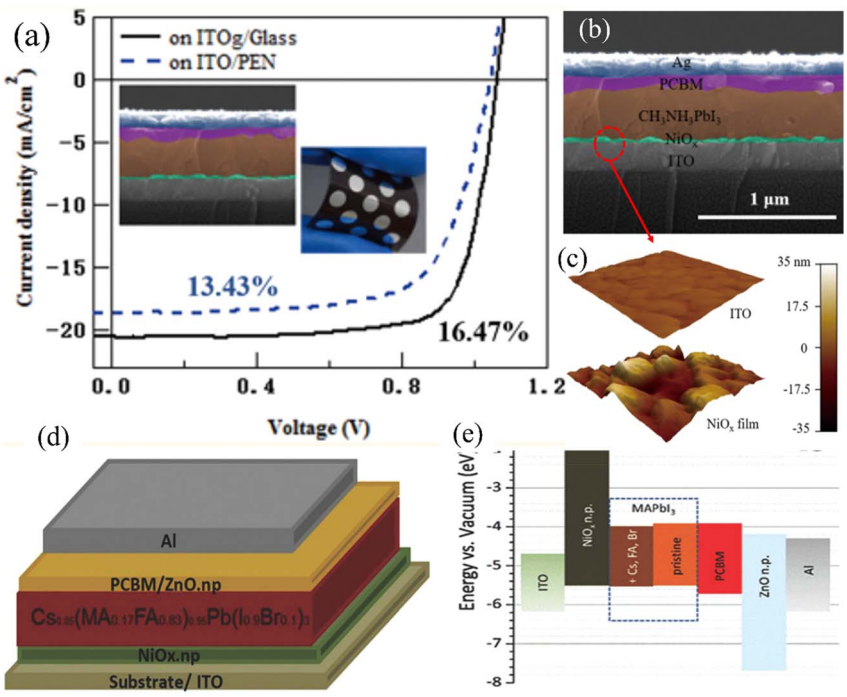

Fig. 18 (a) *J–V* curves of the devices based on NiO_x layers, (b) cross-sectional SEM image of the NiO_x-based FPSC, and (c) AFM images of ITO and the NiO_x film on the ITO substrate. Reprinted with permission from ref. 177. Copyright 2016, American Chemical Society. (d) Architecture of the inverted planar PSCs and (e) energy levels of the layers. Reprinted with permission from ref. 182 Copyright 2018, Wiley-VCH.

Later, He *et al.*[184] successfully prepared high-quality, phase-pure Cu-doped NiO_x nanoparticles using a chemical co-precipitation method. The insertion of Cu improved the electrical conductivity, the work function and densely packed and pinhole-free morphology of the NiO_x film. By employing the Cu-doped NiO_x HTL, the assembled FPSC device displayed a PCE of 16.96%.

4 Flexible electrodes

In general, the electrodes used in electrochemical applications consist of a support material coated with a conductive layer. Specifically, in FPSCs, the electrodes are typically comprised of an active material deposited onto a suitable substrate. Electrodes play a pivotal role in determining the overall performance of FPSCs. To achieve the optimal photovoltaic efficiency and mechanical durability for flexible electronics, the ideal flexible substrate must meet several key requirements,[185] as follows: (i) high optical transparency to allow absorption of a broad spectrum of light, particularly within the visible range (380–780 nm), (ii) excellent electrical conductivity to facilitate efficient charge collection and improve the overall device performance, (iii) effective barrier properties to block oxygen and moisture, which are major contributors to long-term degradation, (iv) strong chemical resistance to withstand exposure to various solvents and gases during the fabrication process, and (v) superior mechanical flexibility to endure mechanical stress and deformation without compromising functional integrity. A variety of materials has been explored as flexible substrates for FPSCs, including ultrathin flexible glass, metal foils (such as titanium, copper, and stainless steel), biodegradable substrates, and polymer films such as polyethylene naphthalate (PEN) and polyethylene terephthalate (PET).[185]

Flexible glass coated with ITO has been employed for FPSC applications. This is due to its excellent thermal stability (>600 °C), chemical stability, electrical conductivity, and superior gas barrier properties. When manufactured at thicknesses below a few hundred micrometres, flexible glass retains these characteristics while gaining mechanical flexibility. The first report utilising ultrathin glass in FPSCs was published in 2015 by Tavakoli *et al.*[29] They used a 50 μm-thick glass substrate to fabricate an FPSC device, which maintained 96% of its initial PCE (12.06%) after 200 bending cycles. The PCE was further enhanced to 13.14% by introducing an antireflection film with outstanding superhydrophobic properties. More recently, Sergio *et al.*[186] reported a PEC of 22.6% under 400 lx light-emitting diode (LED) illumination for FPSCs based on ultrathin ITO-coated flexible glass. The specific W g^{-1} of these devices was found to be an order of magnitude higher than that of the devices based on rigid glass and approximately 40–55% greater than that of the FPSCs using PET substrates. This highlights the significant potential of flexible glass for powering next-generation indoor electronics. However, its brittleness, relatively heavy weight, and cost remain big limitations. Metal foils are another candidate as FPSC substrates, offering excellent thermal stability, conductivity, and corrosion resistance. However, their low optical transmittance limits light absorption, thereby reducing the device efficiency.[187] In contrast, plastic substrates (*e.g.*, PET and PEN) exhibit high optical transparency, excellent flexibility, and good chemical resistance. However, their main drawbacks are low thermal tolerance and poor gas barrier properties.[188] Despite these limitations, plastic-based FPSCs are currently regarded as highly promising. The choice of electrode material that interfaces with the flexible substrate also plays a critical role in the device performance. Various materials have been investigated, including silver nanowires (Ag-NWs), Al-doped ZnO (AZO), ITO, carbon nanotubes (CNTs), graphene, and organic materials. ITO remains one of the most widely used electrode materials in FPSCs. However, its high cost and poor mechanical flexibility limit its suitability for commercial flexible devices, despite its ability to yield high PCEs on PET substrates.[133] Thus, research has been focused on developing alternative materials.

In search of alternatives, Ag-NWs have shown great promise in FPSCs due to their outstanding optical and electrical properties, together with compatibility with solution-based fabrication techniques.[189] For example, Lee *et al.*[190] demonstrated that the FPSC device assembled with Ag-NWs spray-coated on top spiro-MeOTAD as the HTL achieved a PCE of 7.45%. The SEM image of the Ag-NWs is presented in Fig. 19c. By coating Ag-NWs as the top electrode on titanium foil, as shown in Fig. 19a, and the cross-sectional SEM of the whole structure FPSC device (Fig. 19b), the PCE reached 7.58%.[190] The relatively low performance was largely attributed to the inferior conductivity of the ITO used for comparison. To improve the stability of Ag-NWs, Lee *et al.* developed a transparent electrode by sandwiching the Ag-NW layer between two amorphous aluminium-doped zinc oxide (a-AZO) layers (Fig. 19d). The fabricated device based on AZO/AgNW/AZO composite electrodes formed a pinhole-free structure (Fig. 19e and f). The SEM images of the c-AZO/AgNW/AZO and a-AZO/AgNW/AZO composite electrodes (Fig. 19g–i) showed that the c-AZO and a-AZO top layers uniformly covered the AgNWs. The AgNW network structure was well preserved, with only a slight bulge at the junctions due to the annealing process at 190 °C. However, as seen in the individual c-AZO and a-AZO layers, the c-AZO/AgNW/AZO composite exhibited a rough surface with significant porosity, while the a-AZO/AgNW/AZO composite had a smoother surface texture. The FPSC assembled with the a-AZO/Ag-NW/a-AZO/PES configuration achieved a PCE of 11.23%, which is comparable to that of ITO/PEN-based devices (Fig. 19j). Moreover, this device retained 94% of its initial PCE after 400 bending cycles with a 12.5 mm bending radius (Fig. 19k).[191]

PEDOT:PSS is widely used in FPSCs due to its high conductivity, excellent optical transmittance, uniform film coverage, and ease of fabrication through solution-processing techniques. FPSC devices incorporating PEDOT:PSS have demonstrated promising mechanical durability.[192] For instance, Poorkazem *et al.* developed a transparent electrode composed of PEDOT:PSS and In_2O_3 on a PET substrate, as illustrated in Fig. 20a.[192] The SEM images of the fabricated electrodes after undergoing 2000 bending cycles around a cylinder with a 4 mm radius are presented in Fig. 20b–e. It can be seen that the In_2O_3-

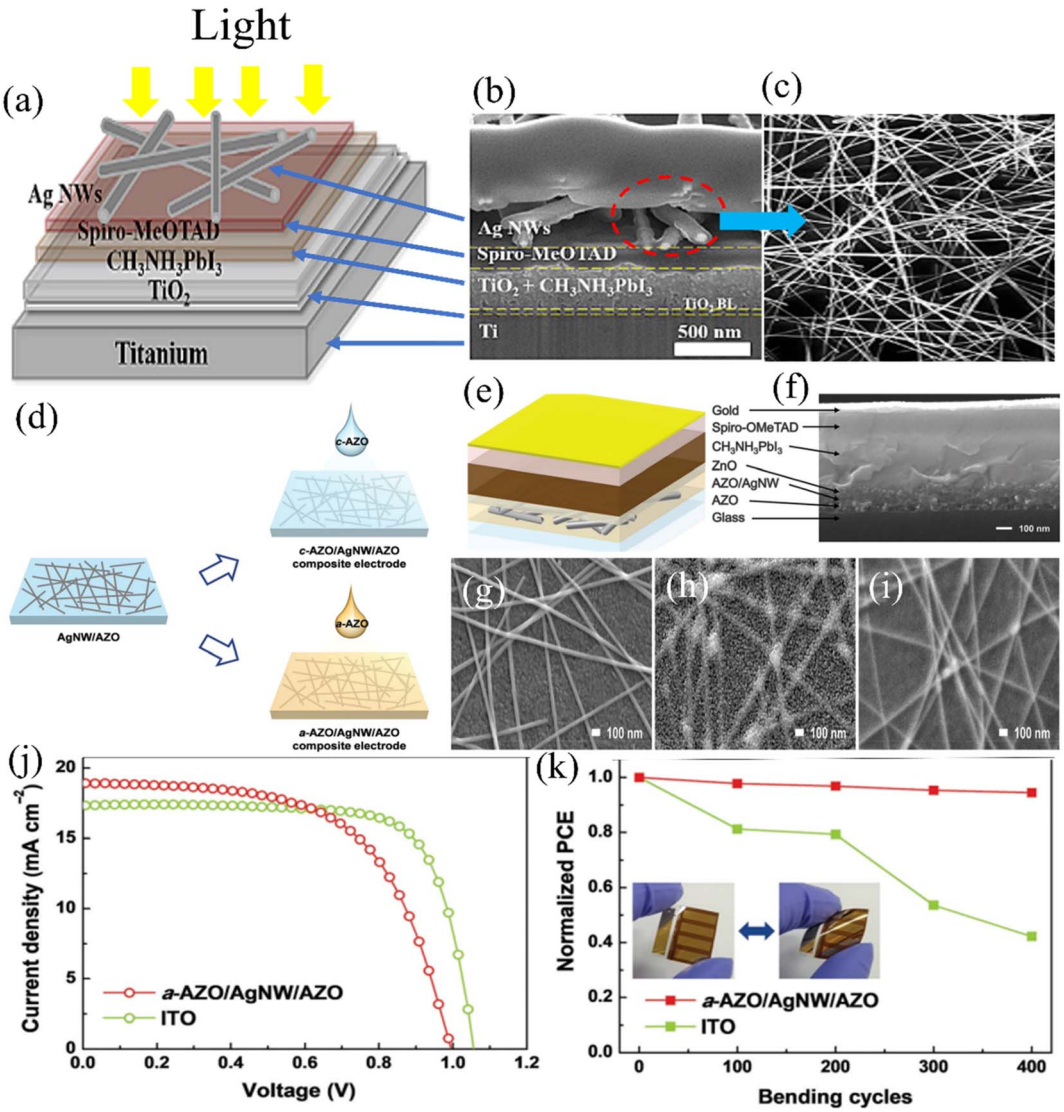

Fig. 19 (a) Scheme, (b) cross-sectional SEM of the FPSC with Ti metal coated with a Ag-NW top electrode, and (c) SEM images of the spray-coated Ag-NWs. Reprinted with permission from ref. 190. Copyright 2016, Wiley-VCH. (d) Scheme of the preparation of a-AZO/Ag-NW/AZO electrodes. (e) Scheme of the FPSC structure based on the AZO/AgNW/AZO electrode. (f) Cross-sectional SEM image of the FPSC device. SEM images of (g) AgNW/AZO, (h) c-AZO/AgNW/AZO, and (i) a-AZO/AgNW/AZO electrodes, (j) *J*–*V* hysteresis characteristics curves, and (k) the mechanical bending test for FPSCs on ITO/PEN and a-AZO/Ag-NW/AZO/PES electrodes. Reprinted with permission from ref. 191. Copyright 2017, Wiley-VCH.

based electrodes exhibited visible cracking (Fig. 20b and c), whereas the PEDOT:PSS layer retained its performance (Fig. 20d and e). The cracking in the metal-based electrodes led to increased sheet resistance, and consequently a reduction in the overall device performance. However, despite its advantages, PEDOT:PSS is known to corrode the bottom substrates over time, which adversely affects the long-term stability of FPSCs. As an alternative, graphene has gained attention for its exceptional chemical stability, superior optical transparency, high charge carrier mobility, and low electrical resistance; qualities making it a compelling candidate for use in FPSC electrodes.[193]

Zhike *et al.*[194] first report the use of graphene as a transparent electrode in FPSCs. They fabricated a device with PET/graphene/poly(3-hexylthiophene) (P3HT)/$MAPbI_3$/$PC_{71}BM$/Ag structure (Fig. 20f). The graphene layer was made using chemical vapour deposition (CVD) and transferred to flexible PET substrates, with the bottom electrodes modified by P3HT films to act as HTLs. As presented in Fig. 20g, the assembled device with the ZEOCOAT™ layer on the PET substrate demonstrates a PCE of 11.5%, which is better than that achieved by the device without ZEOCOAT™ (10.4%). This enhancement is mainly assigned to the rough surface of the PET substrate. After 500 bending cycles with a bending radius of 0.175 cm, the PCE decreased by 14% due to the reduction in the J_{SC}, as shown in Fig. 20h. The morphology of the perovskite layer, graphene electrode, and Ag top electrode in the control devices showed minimal alteration after the bending tests, which is a key factor contributing to the stability of the fabricated devices. Notably, the decline in PCE is

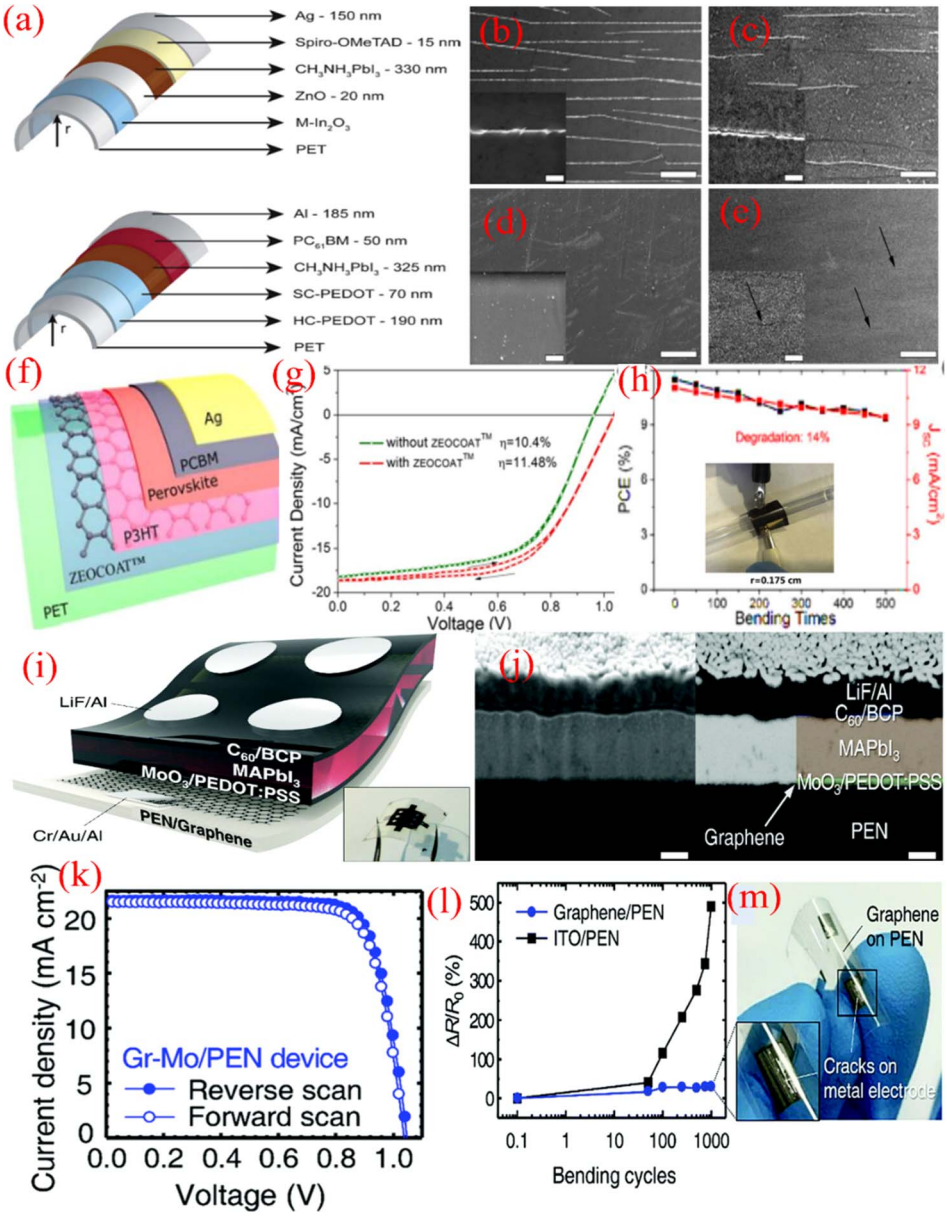

Fig. 20 (a) Scheme of the M-In_2O_3/ZnO/$CH_3NH_3PbI_3$ (top) and HC-PEDOT/SC-PEDOT/$CH_3NH_3PbI_3$ (bottom) devices. SEM images of (b) PET/M-In_2O_3, (c) PET/M-In_2O_3/ZnO/$CH_3NH_3PbI_3$, (d) PET/HC-PEDOT, and (e) PET/HC-PEDOT/SC-PEDOT/$CH_3NH_3PbI_3$ films after 2000 bending cycles. Reprinted with permission from ref. 192. Copyright 2015, Royal Society of Chemistry. (f) Scheme diagram and (g) *J*–*V* curves of the FPSC with/without the ZEOCOAT™ layer. PCE and J_{SC} of the FPSC with different bending cycles and (h) variation in PCE and J_{SC} of the FPSC by bending radius. Reprinted with permission from ref. 194. Copyright 2016, Elsevier. FPSC-based on Gr-Mo/PEN: (i) device structure, (j) cross-sectional SEM image of complete device, (k) *J*–*V* curves, and (l) resistance change of the Gr-Mo/PEN and ITO/PEN films by bending at $R = 4$ mm, and (m) photograph of Gr-Mo/PEN substrate. Reprinted with permission from ref. 77. Copyright 2017, Royal Society of Chemistry.

closely linked to the reduction in J_{SC}. In contrast, both the fill factor (FF) and V_{OC} experienced only minor changes during the bending tests, suggesting that the resistance of the graphene electrode remained unaffected. In a further study by Yoon *et al.*,[77] they demonstrated that the chemical bonding between the graphene layer and PET substrate is significantly responsible for the enhanced performance of FPSCs. In their study, an MoO_3-modified graphene layer prepared by the CVD method was employed as a transparent anode. The structure of the assembled FPSC device is illustrated in Fig. 20i, where $CH_3NH_3PbI_3$ is the perovskite layer, PEDOT:PSS is the HTL, fullerene (C_{60}) is the ETL, and bathocuproine (BCP) is the hole blocking layer (HBL). The entire fabrication process was carried out at a relatively low temperature (<110 °C). According to the cross-sectional SEM image of the Gr-Mo/PEN device (Fig. 20j), the PEDOT:PSS layer was well formed on the hydrophobic graphene surface, given that the 2 nm-thick MoO_3 interfacial layer rendered the hydrophobic graphene surface sufficiently hydrophilic. As a result, the subsequent perovskite layer was also uniformly fabricated on the Gr-Mo/PEN substrate. In addition,

the surface of the perovskite layers was observed to be quite smooth. The PCE of the device increased to 16.8% (Fig. 20k). As shown in Fig. 20m, the relative resistance for the ITO/PEN film initially increased slightly, but then increased sharply after 50 bending cycles, reaching five times the initial value after 1000 cycles. In contrast, the relative resistance of the Gr-Mo/PEN film increased only 0.4 times its original value after 1000 bending cycles.

Due to their low electrical resistance and excellent optical transparency, carbon nanotubes (CNTs) have received significant attention as promising electrode materials for FPSCs. However, the overall performance remained lower than that of graphene-based flexible devices, primarily due to limitations in CNT film morphology and light transmittance. In parallel, environmental concerns regarding petroleum-based, non-biodegradable polymer substrates have received interest as biodegradable and eco-friendly alternatives for FPSCs. Among them, cellulose-based materials have emerged as promising green substrates. Nanocellulose paper (NCP), which can be extracted from abundant cellulose-rich biomass, exhibits high transparency together with respectable mechanical, thermal, and chemical stability. Moreover, it is biodegradable, cost-effective, and can be derived from biowaste. Nevertheless, the water solubility of NCP in aqueous solutions compromises its structural integrity, limiting its direct application in electronic devices.[28] Thus, to address this issue, Huang *et al.*[195] successfully extracted NCP from a viscous solution of nanocellulose of cotton and coated it with acrylic resin to form a waterproof layer, as described in Fig. 21a (steps 1–3), and then FPSCs were prepared (steps 4–6). The assembled device achieved a PCE of 4.25% (Fig. 21b), with a specific power of 0.56 W g^{-1}. Furthermore, the device retained over 80% of its initial efficiency after 50 bending cycles (Fig. 21c), indicating its satisfactory mechanical stability.

Further progress was reported by Zhu *et al.*,[196] who extracted cellulose nanofibrils (CNFs) from bamboo to create b-CNF substrates (Fig. 22a). Subsequently, a transparent conductive indium zinc oxide (IZO) layer was sputtered onto the b-CNF substrate. The resulting b-CNF/IZO electrode exhibited high visible-range transmittance (~85%), low surface roughness, excellent conductivity (sheet resistance of 41 Ω sq^{-1}), and robust mechanical properties. The structure, morphology, and photovoltaic characteristics have been reported. The structure of the FPSC device based on the b-CNF substrate is CNF/IZO/PEDOT:PSS/perovskite/PCBM/Ag is presented in Fig. 22b. The coated perovskite layer showed a highly compact, large grain size, and monolithically grained films (Fig. 22c and d), which is conducive for the transportation of carriers and suppression of their recombination. The assembled FPSC achieved a PCE of 11.68% (Fig. 22e), the highest reported value among biomass-based PSCs. Additionally, the device retained approximately

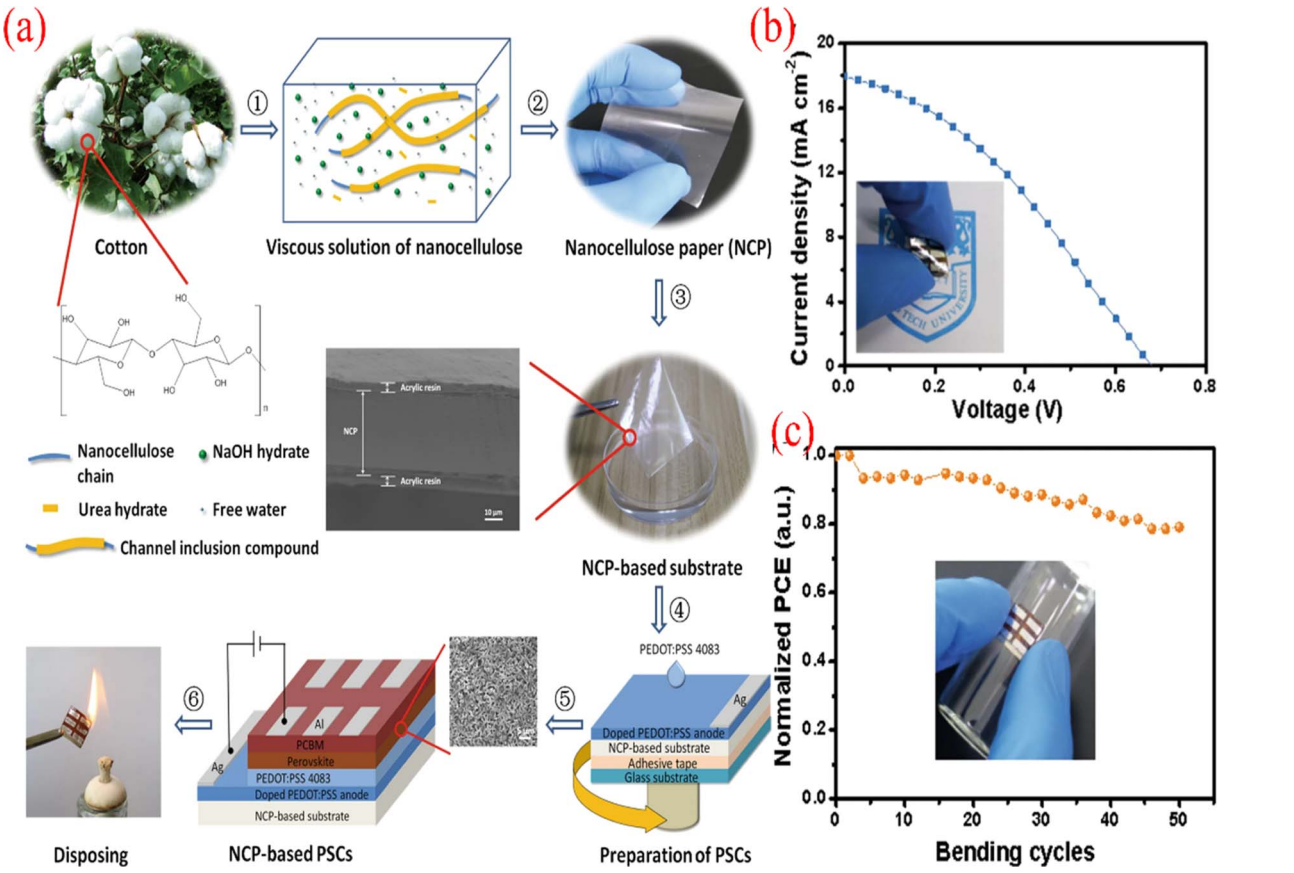

Fig. 21 (a) Scheme of the process of NCP-based substrate and NCP-FPSC, (b) *J*–*V* curves of NCP-FPSC, and (c) normalized PCE-bending cycles state on a bottle with a diameter of 15 mm. Reprinted with permission from ref. 195. Copyright 2019, Springer Nature.

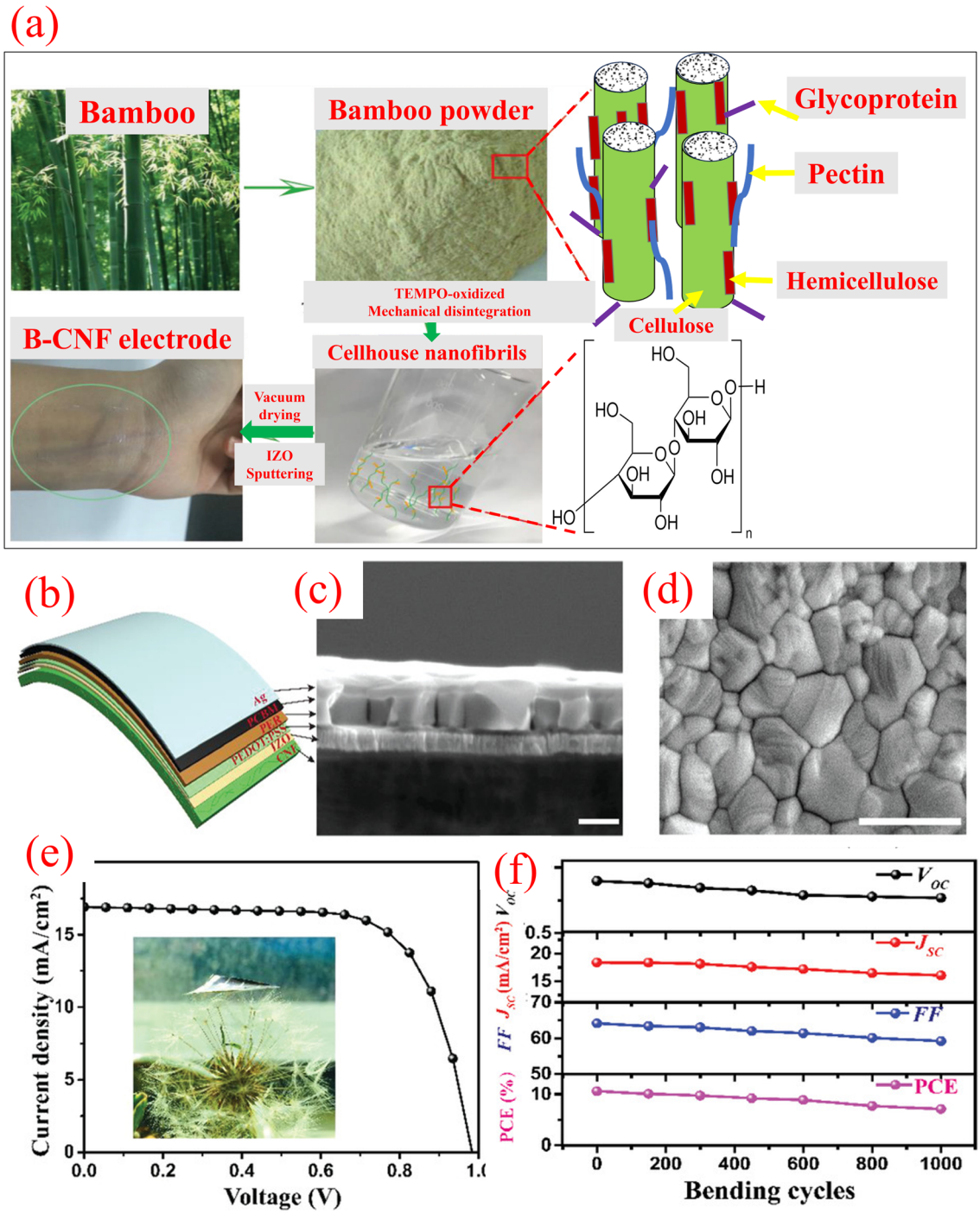

Fig. 22 (a) Scheme of the preparation of b-CNF electrodes, (b) scheme of the FPSCs, (c) cross-section SEM image of the perovskite films based on the b-CNF electrode, (d) top-view SEM image of the perovskite film, (e) *J*–*V* curve of the b-CNF-based FPSCs, and (f) main parameter variation of the FPSCs upon bending tests at a 4 mm radius. Reprinted with permission from ref. 196. Copyright 2019, Wiley-VCH.

70% of its original efficiency after 1000 bending cycles with a 4 mm curvature radius (Fig. 22f).

5 The stability of the FPSCs

As mentioned above, flexible photovoltaic devices are currently receiving significant attention and are highly recommended as the direction of the future photovoltaic industry. This is mainly attributed to the high demand for wearable and portable electronic devices. Among the various flexible solar technologies, FPSCs have emerged as the benchmark, achieving PCEs up to 20%, which surpass that of most other flexible photovoltaic devices.[197] However, despite this progress, several challenges still need to be addressed before FPSCs can be adopted for large-scale commercial applications. One of the most critical issues is the long-term stability of the devices, in addition to mitigating their

performance degradation over time.[198] The term *ecological stability* refers to the resilience of device against environmental factors such as oxygen and moisture, both of which can accelerate the degradation of perovskite materials. Mechanical stability is another key concern and is associated with the formation of cracks in various device layers caused by external stresses during bending, mechanical impact, or thermal expansion due to temperature fluctuations. These structural failures can significantly reduce the overall performance and reliability of the devices. The following sections will discuss in detail the environmental and mechanical stability challenges facing FPSCs and the strategies being developed to address them.

5.1 Mechanical stability of FPSCs

ITO-coated flexible polymer substrates, such as PET and PEN, are widely employed as electrodes in FPSCs. However, these substrates face fundamental limitations, including lower electrical conductivity and reduced mechanical durability compared to ITO-coated rigid glass. Specifically, they exhibit higher sheet resistance, lower optical transmittance, and inferior mechanical strength.[199] Moreover, polymer substrates cannot withstand processing temperatures above 250 °C, which necessitates low-temperature deposition techniques, and typically results in higher ITO resistivity (>20 Ω sq^{-1}).[76] Increasing the ITO thickness can partially offset the conductivity issue; the optimal ITO thickness is approximately 150 nm on glass and around 400 nm on PET. However, a thicker ITO layer on PET compromises the transmittance, leading to a reduced J_{SC}, and consequently lower device performance compared to its rigid counterparts.

Mechanical stability under bending stress is a critical concern for FPSCs. Seok *et al.*[200] reported that after 300 bending cycles, the PCE of FPSCs fabricated on PEN/ITO substrates decreased by 5%. Similarly, Jung *et al.*[143] observed that after 1000 cycles at a 10 mm bending radius, the PCE decreased from 12.20% to 6.10%, indicating significant mechanical degradation.

According to Carlo *et al.*,[201] an ideal radius for bending ITO is 14 mm, while a smaller radius causes the ITO layer to crack. Furthermore, in the study by Liu *et al.*,[202] they employed PET/ITO-based FPSCs to examine the inherent mechanical stability of the FPSCs with various bending radii. They reported that at a radius of 14 mm, there was no noticeable reduction in PCE after 500 cycles, while smaller radii resulted in substantial performance losses. Thus, to address these challenges, Yang *et al.*[76] introduced a novel electrode structure by incorporating a thin silver interlayer between two ITO coatings on PET. This approach enabled a reduction in the overall ITO thickness, while enhancing both the electrical performance and mechanical flexibility. The FPSC achieved a PCE of 18.4% and maintained 83% of their original efficiency after bending with a 4 mm radius.

5.2 Environmental stability of FPSCs

When evaluating solar cells for practical applications, long-term environmental stability is a critical factor. Unfortunately, this remains a major challenge in the development of PSCs. Their instability typically arises from the environmental sensitivity of their HTLs and the intrinsic degradation of perovskite materials. Based on their low-temperature processability and ease of fabrication, HTLs such as spiro-OMeTAD, PTAA, and PEDOT:PSS are widely employed in FPSCs. Also, to enhance the conductivity and overall performance, additives such as bis(trifluoromethanesulfonyl)imide (TFSI) and *tert*-butylpyridine (*t*-BP) are often incorporated.[203] However, TFSI is highly moisture sensitive and can accelerate the degradation of perovskites, while *t*-BP is corrosive to the perovskite layer.[204] Similarly, the hygroscopic nature of PEDOT:PSS contributes to poor device stability.[205] Thus, to address these limitations, alternative HTLs with improved environmental stability, such as nickel oxide (NiO), copper iodide (CuI), and poly(3-hexylthiophene) (P_3HT), have been developed using low-temperature processes.[187] These materials have demonstrated enhanced stability and performance in FPSCs. Nevertheless, perovskite layers remain highly sensitive to environmental factors such as oxygen, UV, and humidity, leading to their degradation and phase transitions. For example, $CH_3NH_3PbI_3$ decomposes into PbI_2 and CH_3NH_3I upon exposure to ambient air,[206] while formamidinium lead iodide ($FAPbI_3$) transitions from the photoactive black α-phase to the non-photoactive yellow δ-phase in the presence of moisture.[207] Given these vulnerabilities, encapsulation technology has become essential for protecting FPSCs from environmental degradation, particularly for industrial-scale applications. However, effective encapsulation is challenging due to the high water vapour transmission rate (WVTR) and oxygen permeability of common flexible substrates such as PEN and PET.[207] Consequently, FPSCs require encapsulation on both their front and rear sides. Their front (active) surface can be protected using flexible sealing films with low WVTR and oxygen ingress, while their rear side can be encapsulated using barrier layers deposited by techniques such as atomic layer deposition (ALD), physical vapor deposition (PVD), and plasma-enhanced chemical vapor deposition (PECVD).[208] According to Weerasinghe *et al.*,[209] FPSCs equipped with robust encapsulation retained their initial performance after 500 h of exposure to 30–80% relative humidity, whereas unencapsulated or poorly encapsulated devices exhibited significant degradation within 100–400 h. These results underscore the critical importance of high-quality encapsulation in ensuring the long-term stability of FPSCs.

6 Real applications of FPSCs

Owing to the aforementioned advantages, FPSCs have great potential for integration into a wide range of applications, including wearable electronics, vehicles, and even aerospace systems.[28] In the following sections, we highlight the recent advancements in the development of FPSCs for these three key application areas.

6.1 FPSCs for wearable devices

Wearable devices have become increasingly integrated into daily life, largely due to their low energy requirements. Future

wearable electronics are expected to be self-powered by advanced energy harvesting and storage technologies capable of generating electricity on demand.[28] In this context, significant efforts have been dedicated to developing high-efficiency FPSCs as energy sources for emerging wearable technologies, such as electronic skin, smart textiles, and surface-conforming foils, which can monitor physiological conditions or track physical activity.[28] Indoor lighting typically ranges from 100 to 1000 lux, corresponding to an irradiance of approximately 31–310 mW cm^{-2} under a 6500 K fluorescent lamp. Assuming a PCE of 20%, an FPSC would require a surface area of less than 1800 cm^2 to generate 100 mW; an area easily accommodated on clothing or accessories such as bags and hats. This level of output is sufficient to power low-energy devices, including wireless sensors, portable electronics, and components of the Internet of Things (IoT). Thus, FPSCs are well suited to serve as power sources for wearable electronics under both indoor and outdoor lighting conditions.[210] However, a primary concern in wearable

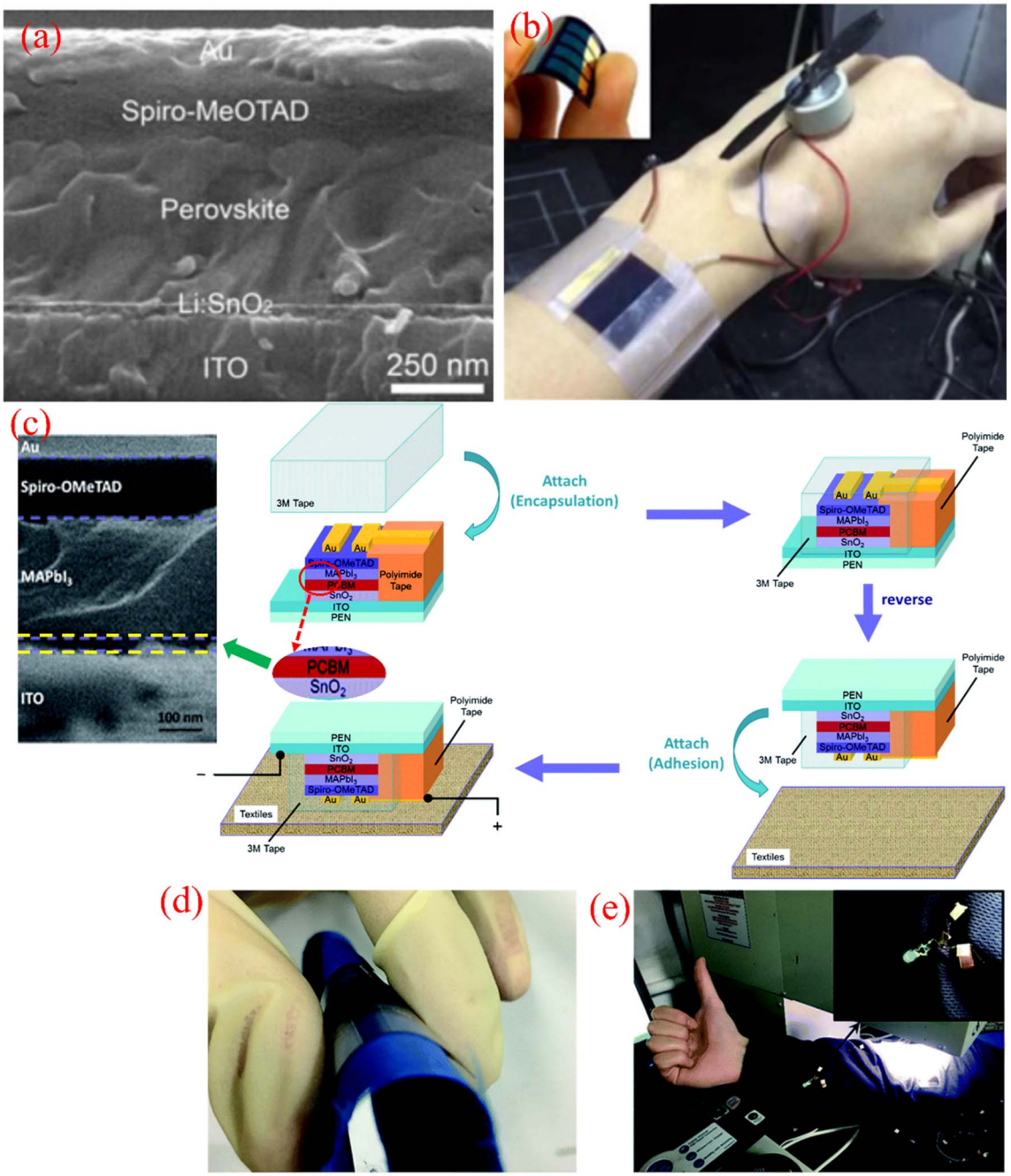

Fig. 23 (a) Cross-sectional SEM image and (b) photographs of FPSC with Li:SnO_2 ETL. Reprinted with permission from ref. 153. Copyright 2016, Elsevier. (c) Scheme of the fabrication of the textile-based FPSC with SnO_2 and PCBM ETL and the corresponding cross-sectional SEM image, (d) photographs of the textile-based FPSC and (e) commercial LED lit by the fabricated textile-based FPSC under 0.8 sun illumination. Reprinted with permission from ref. 212. Copyright 2017, Royal Society of Chemistry.

technology is the limited availability of stable, low-energy power sources.[211] Thus, to address this, various high-conductivity and mechanically stable multifunctional charge transport layers (CTLs) have been explored to enable efficient electron transport. For example, Kim *et al.*[143] demonstrated an FPSC incorporating a 20 nm amorphous compact TiO_x CTL, which achieved a PCE of 12.2%. The device maintained a stable performance under 0.4 sun illumination and at an incident angle of 45°, and exhibited excellent mechanical durability; losing only about 5% of its initial efficiency after 1000 bending cycles at a 10 mm radius. However, despite these advances, the performance of FPSCs remains limited by the relatively low conductivity of metal oxides synthesized at low temperatures. A promising strategy to overcome this is doping metal oxides with elements that enhance their conductivity and align energy levels with the perovskite absorber. For instance, Park *et al.*[153] successfully prepared FPSCs using Li-doped SnO_2 prepared in solution as the ETL at 185 °C. Lithium doping not only improved the conductivity of SnO_2 but also shifted its CB downward, facilitating more efficient electron injection from the perovskite layer. As shown in the cross-sectional SEM image of the fabricated device in Fig. 23a, the deposited Li:SnO_2 thin film on ITO was pin hole free and highly uniform with a smooth surface. The FPSC device with an active area of 0.48 cm^2 achieved a PCE of 12.17% under 1 sun illumination and was successfully used to operate a portable fan (Fig. 23b). The device also demonstrated excellent mechanical stability, retaining 91.9% of its initial efficiency after 500 bending cycles. Further advancements in wearable FPSCs have been demonstrated by Lam *et al.*,[212] who developed a textile-based FPSC utilizing a readily available elastomer as an efficient compressive medium. The device employed an SnO_2 ETL paired with a thin PCBM layer (Fig. 23c). This configuration achieved a PCE of 14.3% and exhibited strong ambient stability as well as waterproof capabilities. After 425 h of storage, the textile-based device retained approximately 70% of its initial efficiency. The fabricated device effectively demonstrated the performance of a high-efficiency textile-based FPSC (Fig. 23d). Furthermore, the authors connected multiple integrated FPSCs in series on the textile, which successfully powered a commercial LED (Fig. 23e). This

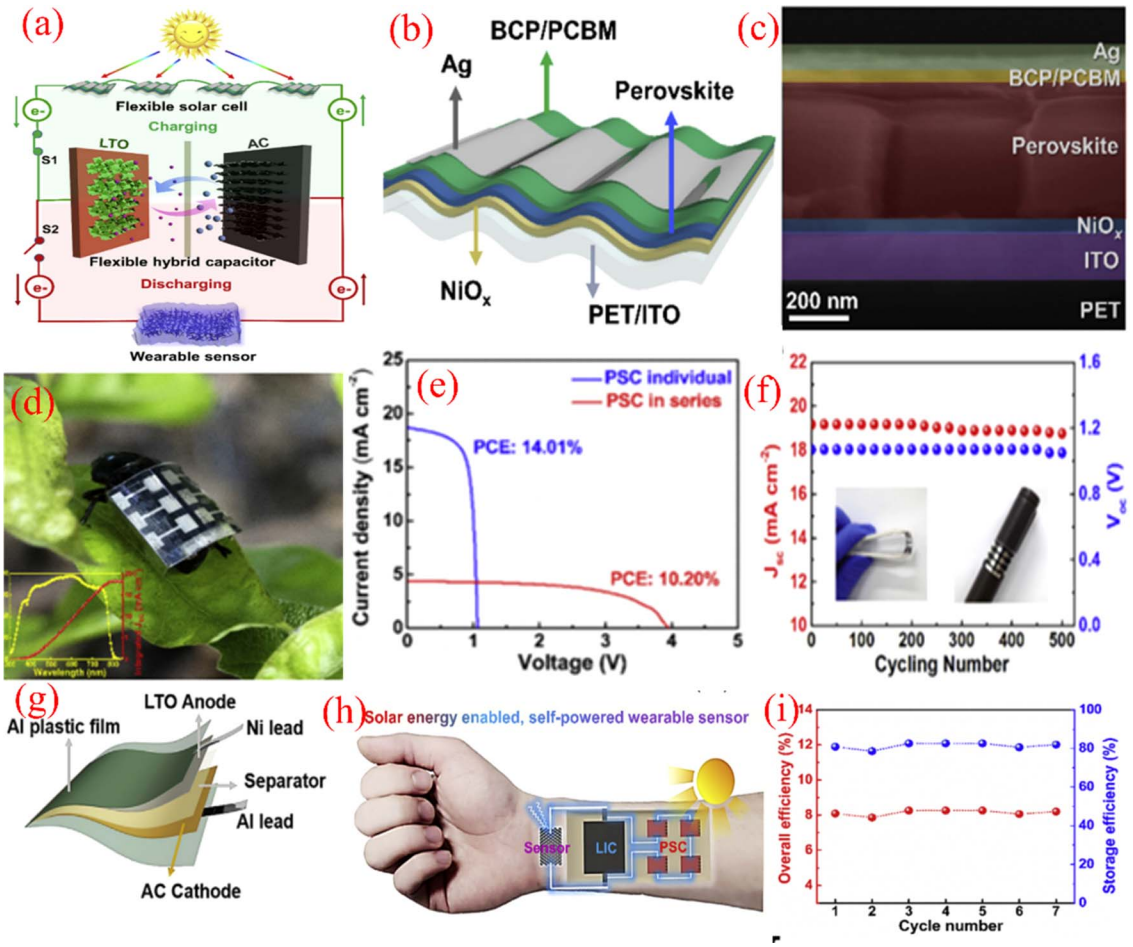

Fig. 24 (a) Scheme of the integrated FPSC-LIC system, (b) scheme of the FPSC structure, (c) cross-sectional SEM of the FPSC device, (d) digital photograph for the as-prepared PSC unit on a live beetle (inset is the IPCE spectrum of the PSC device), (e) *J*–*V* curves of individual FPSC and four FPSCs in series, (f) stability of the photovoltaic parameters with varying bending cycles, (g) scheme of the FLIC device, (h) scheme of the PSC-LIC-sensor integrated system, and (i) Overall efficiency of the PSC-LIC device and the energy storage efficiency of the LIC as a function of the cycle number. Reprinted with permission from ref. 213. Copyright 2019, Elsevier.

indicates the potential of the device to enhance the functionality of wearable electronics by serving as a reliable power supply.

FPSCs devices are also used in self-powered wearable devices, which consist of energy harvesting and storage integrated systems. For example, Chao *et al.*[213] designed an FPSC-photo-rechargeable lithium-ion capacitor (LIC) for self-powering wearable strain sensors (Fig. 24a). A schematic illustration of the fabricated FPSC device is displayed in Fig. 24b and c. According to the photograph in Fig. 24d, it can be seen that the assembled device was directly worn on a live beetle, demonstrating favorable wearability. The PCE of the single FPSC device with the configuration of PET/ITO/NiO_x/$MA_{1-\gamma}FA_\gamma PbI_{3-x}Cl_x$/PCBM/BCP/Ag was 14.01%, while the value was 8.41% when FPSC and LIC were integrated into a single system (Fig. 24e). Additionally, the system delivered a high output voltage of 3 V at a discharge current density of 0.1 A g^{-1}. A module exhibited excellent mechanical durability, maintaining its performance after 500 bending cycles (Fig. 24f). They constructed a flexible LIC based on an LTO/rGO anode and an AC cathode (Fig. 24g). A self-powered wearable sensor equipped with solar energy capabilities is shown after device integration (Fig. 24h), emphasizing its combined functions of energy harvesting, storage, and utilization, together with its ability to conform to the skin. This type of device can reliably and continuously monitor both subtle and more pronounced physiological signals without relying on an external power supply. Fig. 24i demonstrates that the PSC-LIC system achieved a consistently high and stable overall efficiency throughout photo-charging and discharge cycles, reaching a peak of 8.41% and averaging 8.19% at a current density of 0.1 A g^{-1}. As the applied current density increased, the overall efficiency gradually declined from 8.19% at 0.05 A g^{-1} to 6.70% at 1 A g^{-1}. Moreover, the LIC component within the integrated system showed an average energy storage efficiency exceeding 80%.

These results highlight the potential of FPSCs in enabling the autonomous operation of wearable electronics. However, the brittleness of perovskite crystals can compromise their mechanical stability and limit their large-scale application. Thus, to address this, Hu *et al.*[19] introduced polystyrene-doped nanocellular PEDOT:PSS (NC-PEDOT:PSS) in the low-temperature process to be utilised as the HTL (Fig. 25a). Owing to the mechanical stress-relieving capability of the nanocellular scaffold, these PSCs demonstrate outstanding repeatability and stability, together with exceptional resistance to bending (Fig. 25b). As shown in Fig. 25c and d, FPSCs incorporating the NC-PEDOT:PSS layer were effectively integrated into a wearable solar power source. A total of 24 solar cell units was utilized to operate a portable fan and a multifunctional electronic watch during various body movements. The prepared NCPEDOT:PSS film displayed three different diameters, as demonstrated by the SEM image (Fig. 25e). A cross-sectional SEM image of the complete device (substrate/transparent electrode/NC-PEDOT:PSS/perovskite/PCBM/Ag) is shown in Fig. 25f. The resulting FPSC device achieved a PCE of 12.32% with excellent mechanical robustness (Fig. 25f–h). According to the SEM images in Fig. 24i and j, the PEDOT:PSS-based films developed visible cracks after 1000 bending cycles, whereas the NC-PEDOT:PSS-based films maintained a uniform structure. This indicates that the NC-PEDOT:PSS scaffold effectively relieved the stress during repeated narrow bending.

To further enhance the mechanical resilience, they described a biomimetic crystallization approach for forming high-quality perovskite films with a flexible 'brick-and-mortar' design (Fig. 26a). The opposing solubility characteristics of the composite matrix promoted vertically oriented micro-parallel crystal growth and provided the stretchability needed to overcome the 'cask effect' in PSCs.[214] As illustrated in Fig. 26b, the insoluble poly(styrene-*co*-butadiene) (SBS) scaffold decreased the number of nucleation sites and facilitated heterogeneous nucleation by lowering the nucleation energy barrier. Simultaneously, the interaction between the soluble polyurethane (PU) and PbX_2 (X = I or Br) helped to slow down the crystallization process, leading to the formation of high-quality perovskite in PSCs. According to the SEM images in Fig. 26c and d, the reference perovskite film exhibited a rough surface with an average grain size of approximately 360 nm. In contrast, the film incorporating the SBS–PU biomimetic structure displayed significantly larger crystals, exceeding 700 nm in size. It is well-established that perovskite films are more prone to fracture at the grain boundaries than within the crystal grains themselves. Thus, the devices with the SBS–PU biomimetic displayed a higher PEC than the other devices (Fig. 26e). Furthermore, an FPSC with 56.02 cm^2 achieved a PCE of 7.91%, making it suitable as a skin-conforming power source (Fig. 26f). The FPSC module was capable of conveniently charging commercial wearable devices, such as a smartwatch, even during various body movements (Fig. 26g).

In the context of wearable electronics, both stretchability and twistability are crucial design features, and these studies illustrate the promising potential of FPSCs to meet these demands.

6.2 FPSCs for unmanned aerial vehicles

The "Sunrise I" solar-powered aircraft, built in 1974, was one of the earliest demonstrations of solar energy in aviation, utilizing six round solar cells (5.1 cm in diameter) with a total weight of 3.289 kg as its power source.[215] In actual tests, "Sunrise II" delivered a maximum output of 580 W and maximum efficiency of 0.23 W g^{-1} using four assembled solar cells (2 × 4 cm). The successful flight of the Sunrise vehicles showed that using solar cells in airplanes would be feasible.[28] To date, many attempts have been made following this successful.[216,217] Currently, FPSCs hold significant promise for powering lightweight, unmanned aerial electronics. For instance, Kaltenbrunner *et al.*[83] developed an ultrathin FPSC, 3 μm thick, specifically designed for aerial applications. The device structure is comprised of 4 μm-thick PET foil as the substrate, PEDOT:PSS as the HTL, a $CH_3NH_3PbI_{3-x}Cl_x$ perovskite absorber, and either vacuum-sublimed *N*,*N*-dimethyl-3,4,9,10-perylenetetracarboxylic diimide (PTCDI) or solution-processed 6,6-phenyl-C_{61}-butyric acid methyl ester (PCBM) as the ETL. A chromium oxide (Cr_2O_3) coating was applied to protect the

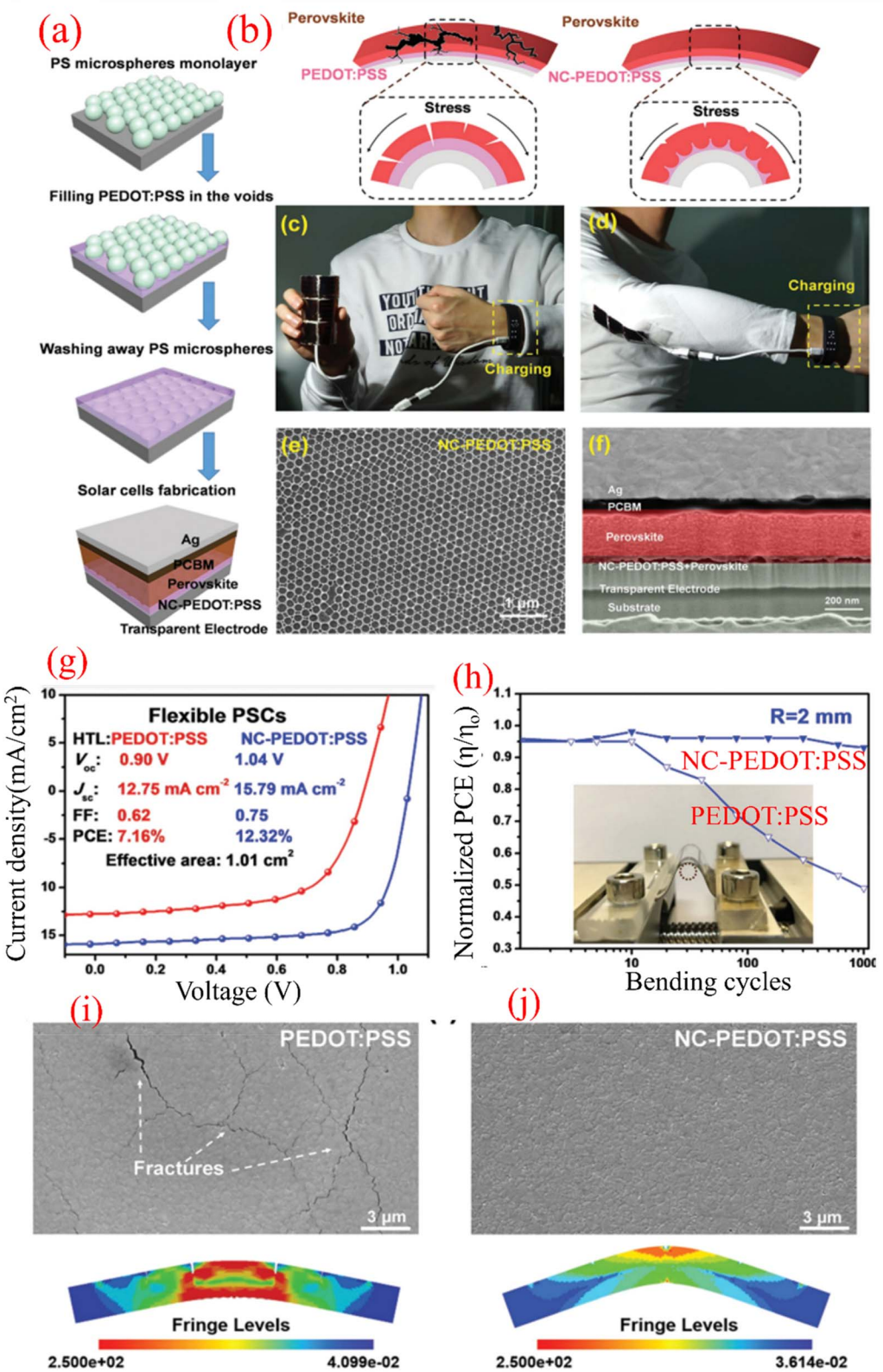

Fig. 25 (a) Fabrication procedure for the NC-PEDOT:PSS and FPSC device, (b) stress release diagram for NC-PEDOT:PSS, (c and d) photographs of the FPSC as a wearable power source, (e) SEM of NC-PEDOT:PSS, (f) SEM cross-sectional image of the FPSC with the NC-PEDOT:PSS layer, (g) *J*–*V* curves of the FPSC based on PEDOT:PSS and NC-PEDOT:PSS HTL, (h) normalized average PCE of FPSC devices as a function of bending cycles with a radius of 2 mm, and (i and j) SEM images and finite-element simulation of films based on PEDOT:PSS and NC-PEDOT:PSS under bending. Reprinted with permission from ref. 19. Copyright 2017, Wiley-VCH.

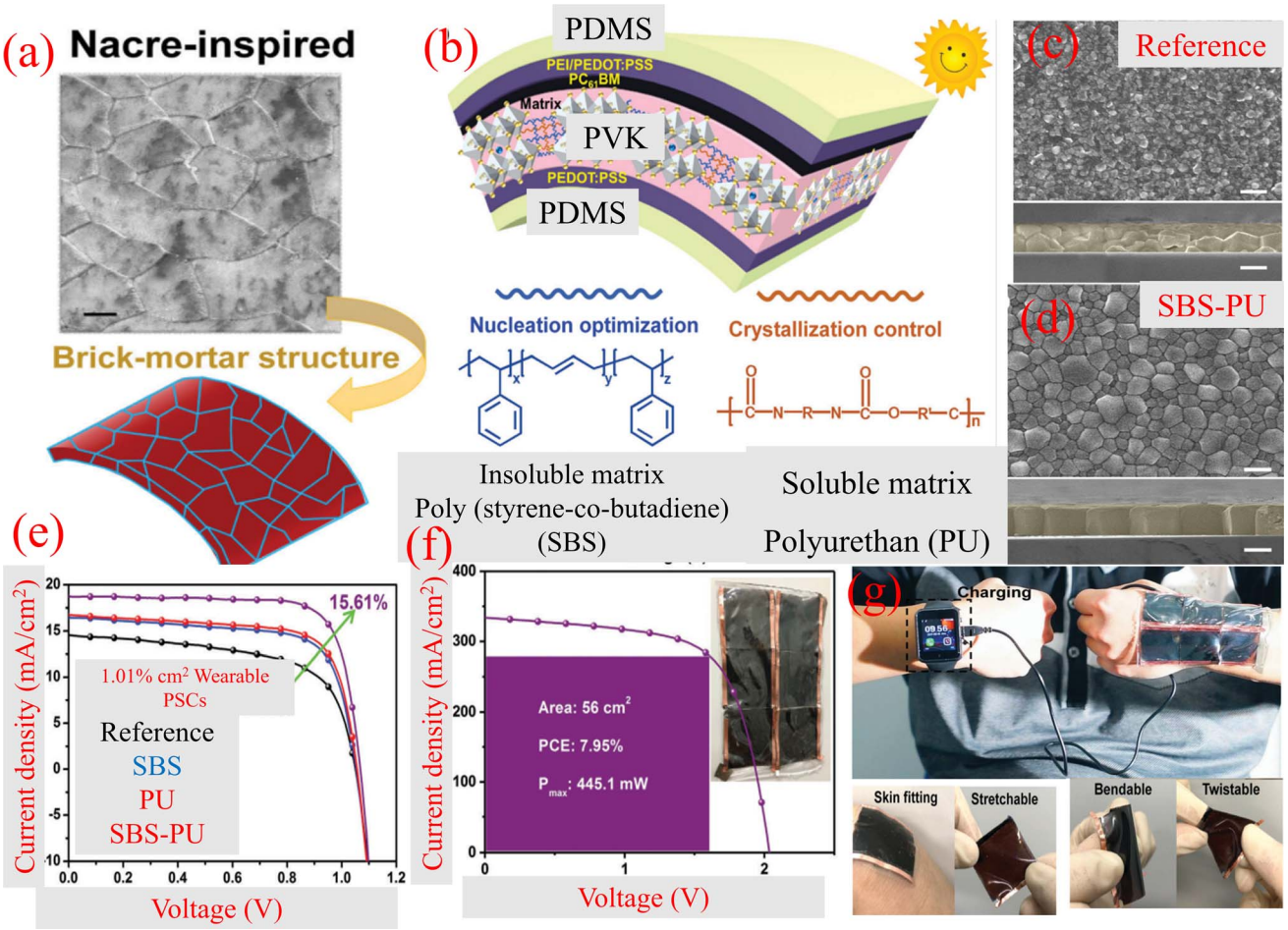

Fig. 26 (a) Brick-mortar structure, (b) structure of wearable FPSCs with chemical structures of SBS and PU. Top-view and cross-section SEM images of (c) reference and (d) SBS–PU-based films. (e) *J–V* curves of the related devices, (f) *I–V* curves of a wearable solar-power source with SBS–PU (inset is the photograph of assembled device), and (g) photographs of wearable FPSCs as a power source to power a smartwatch. Reprinted with permission from ref. 214. Copyright 2019, Royal Society of Chemistry.

metal top contacts from chemical interactions with the perovskite layer, thereby enhancing the stability of the device in air. This ultrathin FPSC demonstrated a PCE of 12% and specific power of 23 W g^{-1}. Furthermore, the device remained operational under real-world environmental conditions for several days. A "solar leaf" configuration, consisting of eight FPSC units integrated with a dried leaf skeleton, generated approximately 2.75 mW under 100 Ω. Additionally, a 64-cell module tested under AM 1.5 solar illumination produced 75 mW and successfully powered an unmanned model aircraft using only ambient sunlight.

6.3 FPSCs for space applications

In general, photovoltaic (PV) devices intended for space applications must meet stringent criteria, including a high PCE, high specific power, and long-term operational stability. It is also critical to evaluate their performance under extreme extraterrestrial conditions,[218] such as exposure to high-energy radiation,[219] extreme temperature, plasma environments, and ultra-low pressures.[28] To date, substantial efforts have been devoted to investigating the stability of PSCs for space applications. For instance, Cojocaru *et al.*[220] investigated the effect of temperature on the crystal structure and photovoltaic performance of $CH_3NH_3PbI_3$-based PSCs. The results revealed that the volume of the perovskite unit cells increased linearly with temperature. Thus, a noticeable difference in the *J–V* curves for the reverse and forward scans was observed in the temperature range of 0 °C to 55 °C. Other research groups have focused on assessing the effects of high-energy particle irradiation on PSCs. For example, Miyasaka *et al.*[221] demonstrated that methylammonium and formamidinium lead iodide PSCs can endure electron irradiation (1 MeV) up to 10^{16} particles per cm^2 and proton irradiation (50 keV) up to 10^{15} particles per cm^2. These results indicate that PSCs possess considerable resilience against radiation-induced degradation, a critical property for space deployment. Moreover, both the type and dosage of radiation significantly influence the long-term material stability. For example, PSCs with the architecture PEDOT:PSS HTL/$Cs_{0.15}MA_{0.10}FA_{0.75}Pb(Br_{0.17}I_{0.83})_3$/$PC_{61}BM$ ETL demonstrated high stability under γ-ray exposure up to 300 Gy. However, when the dose was increased to 500 Gy, the device performance rapidly declined. Additional

insights into the space-relevant degradation mechanisms and radiation tolerance of PSCs can be found in the comprehensive review by Huang *et al.*[28]

7 Conclusion and future perspectives

FPSCs have garnered significant attention as a promising class of next-generation solar cells due to their remarkable optoelectronic properties, high efficiency, and potential for integration into diverse substrates. This convergence offers a unique opportunity to create lightweight, high-performance solar cells that can be seamlessly integrated into a wide range of applications, ranging from wearable electronics to building-integrated photovoltaics (BIPV). This review comprehensively presented the state-of-the-art advancements in the development of FPSCs, including innovations in materials engineering, device architecture, and fabrication techniques, which have driven efficiency improvements and enhanced the mechanical and thermal stability of these devices.

However, despite the remarkable achievements, substantial challenges remain. The mechanical durability of FPSCs under repeated deformation and their long-term environmental stability in real-world conditions, particularly under conditions of moisture, temperature fluctuations, and UV exposure, are still inadequate for commercial viability. Moreover, the toxicity concerns related to lead-based perovskites are critical issues that must be addressed to ensure the commercialization and widespread adoption of this technology. Furthermore, the scalability of fabrication methods must be enhanced to meet the demands of large-scale production, while ensuring cost-effectiveness without compromising the device performance. Future research must prioritize the development of strategies to mitigate these challenges. Key areas of focus include the development of lead-free perovskites or low-toxicity alternatives, the optimization of encapsulation techniques for enhanced stability, and the improvement of mechanical resilience through advanced flexible substrates and protective coatings. Additionally, scaling up the fabrication methods such as R-to-R processing and the integration of FPSCs into multifunctional systems will be pivotal for realizing the full potential of this technology.

In conclusion, although FPSCs are poised to revolutionize the solar energy landscape, realizing their full potential will require sustained interdisciplinary efforts across materials science, engineering, and environmental sustainability. By overcoming the remaining barriers, FPSCs can play a pivotal role in the transition to a more sustainable and energy-efficient future, offering scalable, versatile solutions for the renewable energy sector.

Abbreviations

PVs	Photovoltaics
PSCs	Perovskite solar cells
FPSCs	Flexible perovskite solar cells
OPV	Organic photovoltaics
QDSCs	Quantum dot solar cells
DSSCs	Dye-sensitized solar cells
PCE	Power conversion efficiency
TFSCs	Thin-film solar cells
ETL	Electron transport layer
HTL	Hole transport layer
TCO	Transparent conducting oxide
PET	Poly(ethylene terephthalate)
PEN	Poly(ethylene naphthalate)
MA^+	Methylammonium ($CH_3NH_3^+$)
FA^+	Formamidine ($CH_3CH_2NH_3^+$)
CBD	Chemical bath deposition
PEALD	Plasma-enhanced atomic layer deposition
PEDOT:PSS	Poly(3,4-ethylenedioxythiophene)–poly(styrenesulfonate)
CB/M	Conduction band/maximum
VB/M	Valence band/maximum
R-to-R	Roll-to-roll

Data availability

In this review, no software or code has been included, and no new data were generated or analyzed as part of this review. Additionally, copyright permissions for all figures have been obtained.

Conflicts of interest

There are no conflicts of interest to declare.

References

1 S. Mishra, S. Ghosh and T. Singh, *ChemSusChem*, 2021, **14**, 512–538.
2 J. Gong, K. Sumathy, Q. Qiao and Z. Zhou, *Renew. Sustain. Energy Rev.*, 2017, **68**, 234–246.
3 A. Hagfeldt, G. Boschloo, L. Sun, L. Kloo and H. Pettersson, *Chem. Rev.*, 2010, **110**, 6595–6663.
4 X. Wang, X. Li, G. Liu, J. Li, X. Hu, N. Xu, W. Zhao, B. Zhu and J. Zhu, *Angew. Chem.*, 2019, **131**, 12182–12186.
5 Y. Li, B. Li, D. Zhang, L. Cheng and Q. Xiang, *ACS Nano*, 2020, **14**, 10552–10561.
6 D. M. Chapin, C. S. Fuller and G. L. Pearson, *J. Appl. Phys.*, 1954, **25**, 676–677.
7 M. Grätzel, *Nature*, 2001, **414**, 338–344.
8 A. S. A. Ahmed, W. Xiang, M. Abdelmotalleib and X. Zhao, *ACS Appl. Electron. Mater.*, 2022, **4**, 1063–1071.
9 R. W. Birkmire and E. Eser, *Annu. Rev. Mater. Sci.*, 1997, **27**, 625–653.
10 A. Chirila, S. Buecheler, F. Pianezzi, P. Bloesch, C. Gretener, A. R. Uhl, C. Fella, L. Kranz, J. Perrenoud, S. Seyrling, R. Verma, S. Nishiwaki, Y. E. Romanyuk, G. Bilger and A. N. Tiwari, *Nat. Mater.*, 2011, **10**, 857–861.
11 S. M. Hubbard, C. D. Cress, C. G. Bailey, R. P. Raffaelle, S. G. Bailey and D. M. Wilt, *Appl. Phys. Lett.*, 2008, **92**, 123512.

12 Y. Deng, J. Yang, R. Yang, K. Shen, D. Wang and D. Wang, *AIP Adv.*, 2016, **6**, 015203.
13 M. Ye, X. Hong, F. Zhang and X. Liu, *J. Mater. Chem. A*, 2016, **4**, 6755–6771.
14 G. H. Carey, A. L. Abdelhady, Z. Ning, S. M. Thon, O. M. Bakr and E. H. Sargent, *Chem. Rev.*, 2015, **115**, 12732–12763.
15 O. Brian and G. Michael, *Nature*, 1991, **353**, 737–740.
16 S. A. A. Abdelaal, X. Wanchun, S. M. H. Fatma and Z. Xiujian, *Sol. Energy*, 2021, **230**, 902–911.
17 A. S. A. Ahmed, W. Xiang, Z. Li, I. S. Amiinu and X. Zhao, *Electrochim. Acta*, 2018, **292**, 276–284.
18 S. Yang, W. Fu, Z. Zhang, H. Chen and C.-Z. Li, *J. Mater. Chem. A*, 2017, **5**, 11462–11482.
19 X. Hu, Z. Huang, X. Zhou, P. Li, Y. Wang, Z. Huang, M. Su, W. Ren, F. Li, M. Li, Y. Chen and Y. Song, *Adv. Mater.*, 2017, **29**, 1703236.
20 S. Park, K. Parida and P. S. Lee, *Adv. Energy Mater.*, 2017, **7**, 1701369.
21 C. Chen, Y. Kuang and L. Hu, *Joule*, 2019, **3**, 683–718.
22 D. J. Lipomi and Z. Bao, *Energy Environ. Sci.*, 2011, **4**, 3314–3328.
23 T. Q. Trung and N.-E. Lee, *Adv. Mater.*, 2017, **29**, 1603167.
24 S. Gong and W. Cheng, *Adv. Energy Mater.*, 2017, **7**, 1700648.
25 P. C. Y. Chow and T. Someya, *Adv. Mater.*, 2020, **32**, 1902045.
26 Z. Xu, T. Xue, Q. Guo, J. Yao, G. Li, J. Du, E. Zhou and Z. A. Tan, *Information & Functional Materials*, 2025, **2**, 1–39.
27 J. Wu, P. Chen, H. Xu, M. Yu, L. Li, H. Yan, Y. Huangfu, Y. Xiao, X. Yang, L. Zhao, W. Wang, Q. Gong and R. Zhu, *Sci. China Mater.*, 2022, **65**, 2319–2324.
28 Y. Hu, T. Niu, Y. Liu, Y. Zhou, Y. Xia, C. Ran, Z. Wu, L. Song, P. Müller-Buschbaum, Y. Chen and W. Huang, *ACS Energy Lett.*, 2021, **6**, 2917–2943.
29 M. M. Tavakoli, K.-H. Tsui, Q. Zhang, J. He, Y. Yao, D. Li and Z. Fan, *ACS Nano*, 2015, **9**, 10287–10295.
30 L. Xiaojing, Z. Wei and L. Shengzhong, *Mater. Sci. Semicond. Process.*, 2015, **39**, 192–199.
31 F. Di Giacomo, A. Fakharuddin, R. Jose and T. M. Brown, *Energy Environ. Sci.*, 2016, **9**, 3007–3035.
32 T. Jiao, D. Wei, J. Liu, W. Sun, S. Jia, W. Zhang, Y. Feng, H. Shi and C. Du, *RSC Adv.*, 2015, **5**, 73202–73206.
33 F. Meillaud, M. Boccard, G. Bugnon, M. Despeisse, S. Hänni, F. J. Haug, J. Persoz, J. W. Schüttauf, M. Stuckelberger and C. Ballif, *Mater. Today*, 2015, **18**, 378–384.
34 D. Dheeraj, S. Muthu, S. Prakasha and S. Mysore Sridhar, *Renew. Sustain. Energy Rev.*, 2022, **159**, 112252.
35 L. Li, Y. Wang, X. Wang, R. Lin, X. Luo, Z. Liu, K. Zhou, S. Xiong, Q. Bao, G. Chen, Y. Tian, Y. Deng, K. Xiao, J. Wu, M. I. Saidaminov, H. Lin, C.-Q. Ma, Z. Zhao, Y. Wu, L. Zhang and H. Tan, *Nat. Energy*, 2022, **7**, 708–717.
36 H. Zhang, J. Cheng, F. Lin, H. He, J. Mao, K. S. Wong, A. K.-Y. Jen and W. C. H. Choy, *ACS Energy Lett.*, 2021, **6**, 2917–2943.
37 S. Mahalingam, A. Manap, D. Floresyona, R. Rabeya, N. Afandi, Z. Hasan and A. Nugroho, *Renew. Sustain. Energy Rev.*, 2025, **213**, 115488.
38 A. A. Goje, N. A. Ludin, P. N. A. Fahsyar, U. Syafiq, P. Chelvanathan, A. D. A.-G. Syakirin, M. A. Teridi, M. A. Ibrahim, M. S. Su'ait, S. Sepeai and A. S. H. M. Yasir, *Mater. Renew. Sustain. Energy*, 2024, **13**, 155–179.
39 Y. Y. Kim, T.-Y. Yang, R. Suhonen, A. Kemppainen, K. Hwang, N. J. Jeon and J. Seo, *Nat. Commun.*, 2020, **11**, 5146.
40 Z. Xu, Q. Zhuang, Y. Zhou, S. Lu, X. Wang, W. Cai and Z. Zang, *Small Struct.*, 2023, **4**, 2200338.
41 D. I. Kutsarov, E. Rezaee, J. Lambert, W. T. Stroud, A. Panagiotopoulos and S. R. P. Silva, *Adv. Mater. Technol.*, 2025, 2401834.
42 J. Y. Kim, J.-W. Lee, H. S. Jung, H. Shin and N.-G. Park, *Chem. Rev.*, 2020, **120**, 7867–7918.
43 P. V. Kamat, *J. Phys. Chem. Lett.*, 2013, **4**, 3733–3734.
44 M. Liu, M. B. Johnston and H. J. Snaith, *Nature*, 2013, **501**, 395–398.
45 M. A. Green, A. Ho-Baillie and H. J. Snaith, *Nat. Photonics*, 2014, **8**, 506–514.
46 M. Grätzel, *Nat. Mater.*, 2014, **13**, 838–842.
47 N.-G. Park, *J. Phys. Chem. Lett.*, 2013, **4**, 2423–2429.
48 T. He, Q. Huang, A. P. Ramirez, Y. Wang, K. A. Regan, N. Rogado, M. A. Hayward, M. K. Haas, J. S. Slusky, K. Inumara, H. W. Zandbergen, N. P. Ong and R. J. Cava, *Nature*, 2001, **411**, 54–56.
49 W.-J. Yin, J.-H. Yang, J. Kang, Y. Yan and S.-H. Wei, *J. Mater. Chem. A*, 2015, **3**, 8926–8942.
50 W.-J. Yin, T. Shi and Y. Yan, *Appl. Phys. Lett.*, 2014, **104**, 063903.
51 I. B. Koutselas, L. Ducasse and G. C. Papavassiliou, *J. Phys.:Condens. Matter*, 1996, **8**, 1217.
52 W. Aron and W. W. Graeme, *J. Solid State Chem.*, 2005, **178**, 1422–1428.
53 G. Xing, N. Mathews, S. Sun, S. S. Lim, Y. M. Lam, M. Grätzel, S. Mhaisalkar and T. C. Sum, *Science*, 2013, **342**, 344–347.
54 T. Kenichiro, T. Takayuki, B. Takuma, K. Takashi, U. Kazuhito and M. Noboru, *Solid State Commun.*, 2003, **127**, 619–623.
55 M. Era, S. Morimoto, T. Tsutsui and S. Saito, *Appl. Phys. Lett.*, 1994, **65**, 676–678.
56 B. J. Kim, S. Lee and H. S. Jung, *J. Mater. Chem. A*, 2018, **6**, 12215–12236.
57 A. Kojima, K. Teshima, Y. Shirai and T. Miyasaka, *J. Am. Chem. Soc.*, 2009, **131**, 6050–6051.
58 N.-G. Park, *J. Phys. Chem. Lett.*, 2013, **4**, 2423–2429.
59 J. Burschka, N. Pellet, S.-J. Moon, R. Humphry-Baker, P. Gao, M. K. Nazeeruddin and M. Grätzel, *Nature*, 2013, **499**, 316–319.
60 L. Etgar, W. Zhang, S. Gabriel, S. G. Hickey, M. K. Nazeeruddin, A. Eychmüller, B. Liu and M. Grätzel, *Adv. Mater.*, 2012, **24**, 2202–2206.
61 B. Saparov and D. B. Mitzi, *Chem. Rev.*, 2016, **116**, 4558–4596.
62 H. S. Jung, G. S. Han, N.-G. Park and M. J. Ko, *Joule*, 2019, **3**, 1850–1880.

63 R. Hu, C. Ge, L. Chu, Y. Feng, S. Xiao, Y. Ma, W. Liu, X. a. Li and M. K. Nazeeruddin, *J. Energy Chem.*, 2021, **59**, 581–588.
64 H.-S. Kim, C.-R. Lee, J.-H. Im, K.-B. Lee, T. Moehl, A. Marchioro, S.-J. Moon, R. Humphry-Baker, J.-H. Yum, J. E. Moser, M. Grätzel and N.-G. Park, *Sci. Rep.*, 2012, **2**, 591.
65 Y. Woon Seok, N. Jun Hong, J. Nam Joong, K. Young Chan, R. Seungchan, S. Jangwon and S. Sang Il, *Science*, 2015, **348**, 1234–1237.
66 L. Xiong, B. Dongqin, Y. Chenyi, D. Jean-David, L. Jingshan, Z. Shaik Mohammed, H. Anders and G. Michael, *Science*, 2016, **353**, 58–62.
67 P. You, G. Tang, J. Cao, D. Shen, T.-W. Ng, Z. Hawash, N. Wang, C.-K. Liu, W. Lu, Q. Tai, Y. Qi, C.-S. Lee and F. Yan, *Light: Sci. Appl.*, 2021, **10**, 68.
68 L. Haizhou, L. Yuhang, A. Paramvir, M. Aditya, R. T. Wolfgang, T. E. Felix, Y. Yingguo, F. Fan, W. Zaiwei, E. A. Claudia, I. C. Brian, A. Anand, Z. Xin, L. Xiaoguo, Z. Yiqiang, M. Z. Shaik, E. Lyndon, R. Ursula, Z. Lirong, H. Anders and G. Michael, *Science*, 2020, **370**, eabb8985.
69 M. H. Kumar, N. Yantara, S. Dharani, M. Graetzel, S. Mhaisalkar, P. P. Boix and N. Mathews, *Chem. Commun.*, 2013, **49**, 11089–11091.
70 Z. Li, C. Jia, Z. Wan, J. Cao, J. Shi, J. Xue, X. Liu, H. Wu, C. Xiao, C. Li, M. Li, C. Zhang and Z. Li, *Nat. Commun.*, 2025, **16**, 1771.
71 J. Chen, X. Fan, J. Wang, J. Wang, J. Zeng, Z. Zhang, J. Li and W. Song, *ACS Nano*, 2024, **18**, 19190–19199.
72 Z. Li, C. Jia, Z. Wan, J. Xue, J. Cao, M. Zhang, C. Li, J. Shen, C. Zhang and Z. Li, *Nat. Commun.*, 2023, **14**, 6451.
73 L. Yang, Q. Xiong, Y. Li, P. Gao, B. Xu, H. Lin, X. Li and T. Miyasaka, *J. Mater. Chem. A*, 2021, **9**, 1574–1582.
74 J. Chung, S. S. Shin, K. Hwang, G. Kim, K. W. Kim, D. S. Lee, W. Kim, B. S. Ma, Y.-K. Kim, T.-S. Kim and J. Seo, *Energy Environ. Sci.*, 2020, **13**, 4854–4861.
75 K. Huang, Y. Peng, Y. Gao, J. Shi, H. Li, X. Mo, H. Huang, Y. Gao, L. Ding and J. Yang, *Adv. Energy Mater.*, 2019, **9**, 1901419.
76 J. Feng, X. Zhu, Z. Yang, X. Zhang, J. Niu, Z. Wang, S. Zuo, S. Priya, S. Liu and D. Yang, *Adv. Mater.*, 2018, **30**, 1801418.
77 J. Yoon, H. Sung, G. Lee, W. Cho, N. Ahn, H. S. Jung and M. Choi, *Energy Environ. Sci.*, 2017, **10**, 337–345.
78 Y. Li, L. Meng, Y. Yang, G. Xu, Z. Hong, Q. Chen, J. You, G. Li, Y. Yang and Y. Li, *Nat. Commun.*, 2016, **7**, 10214.
79 S. S. Shin, W. S. Yang, J. H. Noh, J. H. Suk, N. J. Jeon, J. H. Park, J. S. Kim, W. M. Seong and S. I. Seok, *Nat. Commun.*, 2015, **6**, 7410.
80 C. Roldán-Carmona, O. Malinkiewicz, A. Soriano, G. Mínguez Espallargas, A. Garcia, P. Reinecke, T. Kroyer, M. I. Dar, M. K. Nazeeruddin and H. J. Bolink, *Energy Environ. Sci.*, 2014, **7**, 994–997.
81 J. P. Tiwari, *Small Methods*, 2025, **9**, 2400624.
82 X. Li, H. Yu, Z. Liu, J. Huang, X. Ma, Y. Liu, Q. Sun, L. Dai, S. Ahmad, Y. Shen and M. Wang, *Nano-Micro Lett.*, 2023, **15**, 206.
83 M. Kaltenbrunner, G. Adam, E. D. Głowacki, M. Drack, R. Schwödiauer, L. Leonat, D. H. Apaydin, H. Groiss, M. C. Scharber, M. S. White, N. S. Sariciftci and S. Bauer, *Nat. Mater.*, 2015, **14**, 1032–1039.
84 S. Kang, J. Jeong, S. Cho, Y. J. Yoon, S. Park, S. Lim, J. Y. Kim and H. Ko, *J. Mater. Chem. A*, 2019, **7**, 1107–1114.
85 X. Zhang, C. Zhang, D. Li, S. Cao, M. Yin, P. Wang, G. Ding, L. Yang, J. Cheng and L. Lu, *Nanoscale Res. Lett.*, 2019, **14**, 324.
86 M. Kaltenbrunner, M. S. White, E. D. Głowacki, T. Sekitani, T. Someya, N. S. Sariciftci and S. Bauer, *Nat. Commun.*, 2012, **3**, 770.
87 M. M. Tavakoli, M. H. Gharahcheshmeh, N. Moody, M. G. Bawendi, K. K. Gleason and J. Kong, *Adv. Mater. Interfaces*, 2020, **7**, 2000498.
88 E. Cho, Y. Kang, D. Kim and J. Kim, *Opt. Express*, 2016, **24**, A791–A796.
89 M. Zhang, Z. Li, Z. Gong, Z. Li and C. Zhang, *Energy Adv.*, 2023, **2**, 355–364.
90 M. Park, H. J. Kim, I. Jeong, J. Lee, H. Lee, H. J. Son, D.-E. Kim and M. J. Ko, *Adv. Energy Mater.*, 2015, **5**, 1501406.
91 V. C. M. Duarte and L. Andrade, *Energies*, 2024, **17**(16), 3896.
92 Z. Chuantian, V. Doojin, A. Dechan, D. Liming and G. Mei, *Nano Energy*, 2018, **46**, 185–192.
93 J.-E. Kim, S.-S. Kim, C. Zuo, M. Gao, D. Vak and D.-Y. Kim, *Adv. Funct. Mater.*, 2019, **29**, 1809194.
94 J. Liu, D. Zheng, K. Wang, Z. Li, S. Liu, L. Peng and D. Yang, *Joule*, 2024, **8**, 944–969.
95 Y. Galagan, F. Di Giacomo, H. Gorter, G. Kirchner, I. de Vries, R. Andriessen and P. Groen, *Adv. Energy Mater.*, 2018, **8**, 1801935.
96 T. Bu, J. Li, F. Zheng, W. Chen, X. Wen, Z. Ku, Y. Peng, J. Zhong, Y.-B. Cheng and F. Huang, *Nat. Commun.*, 2018, **9**, 4609.
97 G. Tang and F. Yan, *Nano Today*, 2021, **39**, 101155.
98 C. Bi, B. Chen, H. Wei, S. DeLuca and J. Huang, *Adv. Mater.*, 2017, **29**, 1605900.
99 B. Yang, C. Yao, Y. Yu, Z. Li and X. Wang, *Sci. Rep.*, 2017, **7**, 4936.
100 N. J. Jeon, J. H. Noh, Y. C. Kim, W. S. Yang, S. Ryu and S. I. Seok, *Nat. Mater.*, 2014, **13**, 897–903.
101 Z. Saki, M. M. Byranvand, N. Taghavinia, M. Kedia and M. Saliba, *Energy Environ. Sci.*, 2021, **14**, 5690–5722.
102 Y. Wang, S. Bai, L. Cheng, N. Wang, J. Wang, F. Gao and W. Huang, *Adv. Mater.*, 2016, **28**, 4532–4540.
103 D. Zhou, T. Zhou, Y. Tian, X. Zhu and Y. Tu, *J. Nanomater.*, 2018, **2018**, 8148072.
104 T. Zhang, N. Guo, G. Li, X. Qian, L. Li and Y. Zhao, *J. Mater. Chem. A*, 2016, **4**, 3245–3248.
105 C.-H. Chiang, J.-W. Lin and C.-G. Wu, *J. Mater. Chem. A*, 2016, **4**, 13525–13533.
106 Z. Huanping, C. Qi, L. Gang, L. Song, S. Tze-bing, D. Hsin-Sheng, H. Ziruo, Y. Jingbi, L. Yongsheng and Y. Yang, *Science*, 2014, **345**, 542–546.
107 A. Dualeh, N. Tétreault, T. Moehl, P. Gao, M. K. Nazeeruddin and M. Grätzel, *Adv. Funct. Mater.*, 2014, **24**, 3250–3258.
108 P.-H. Huang, Y.-H. Wang, J.-C. Ke and C.-J. Huang, *Energies*, 2017, **10**, 599.

109 F. Hao, C. C. Stoumpos, P. Guo, N. Zhou, T. J. Marks, R. P. H. Chang and M. G. Kanatzidis, *J. Am. Chem. Soc.*, 2015, **137**, 11445–11452.
110 P. J. Holliman, E. W. Jones, A. Connell, S. Ghosh, L. Furnell and R. J. Hobbs, *Mater. Res. Innovations*, 2015, **19**, 508–511.
111 K. H. Hendriks, J. J. van Franeker, B. J. Bruijnaers, J. A. Anta, M. M. Wienk and R. A. J. Janssen, *J. Mater. Chem. A*, 2017, **5**, 2346–2354.
112 Z. Wenhui, J. Yue, D. Yang, Z. Mingzhi, W. Sujuan, L. Xubing, G. Xinseng, W. Qianming, Z. Guofu, L. Junming, J. N. Michael, K. Krzysztof and G. Jinwei, *Opt. Mater. Express*, 2017, **7**, 2150–2160.
113 X. Cao, L. Zhi, Y. Jia, Y. Li, K. Zhao, X. Cui, L. Ci, D. Zhuang and J. Wei, *ACS Appl. Mater. Interfaces*, 2019, **11**, 7639–7654.
114 N. J. Jeon, J. H. Noh, Y. C. Kim, W. S. Yang, S. Ryu and S. I. Seok, *Nat. Mater.*, 2014, **13**, 897–903.
115 D. Bi, S.-J. Moon, L. Häggman, G. Boschloo, L. Yang, E. M. J. Johansson, M. K. Nazeeruddin, M. Grätzel and A. Hagfeldt, *RSC Adv.*, 2013, **3**, 18762–18766.
116 Y. Han, H. Xie, E. L. Lim and D. Bi, *Sol. RRL*, 2022, **6**, 2101007.
117 J.-H. Im, H.-S. Kim and N.-G. Park, *APL Mater.*, 2014, **2**, 081510.
118 J.-H. Im, H.-S. Kim and N.-G. Park, *APL Mater.*, 2014, **2**, 081510.
119 K. Liang, D. B. Mitzi and M. T. Prikas, *Chem. Mater.*, 1998, **10**, 403–411.
120 D. Yang, R. Yang, S. Priya and S. F. Liu, *Angew Chem. Int. Ed. Engl.*, 2019, **58**, 4466–4483.
121 Z. Xiao, C. Bi, Y. Shao, Q. Dong, Q. Wang, Y. Yuan, C. Wang, Y. Gao and J. Huang, *Energy Environ. Sci.*, 2014, **7**, 2619–2623.
122 Y. Wu, A. Islam, X. Yang, C. Qin, J. Liu, K. Zhang, W. Peng and L. Han, *Energy Environ. Sci.*, 2014, **7**, 2934–2938.
123 T. Li, Y. Pan, Z. Wang, Y. Xia, Y. Chen and W. Huang, *J. Mater. Chem. A*, 2017, **5**, 12602–12652.
124 S. Abicho, B. Hailegnaw, G. A. Workneh and T. Yohannes, *Mater. Renew. Sustain. Energy*, 2022, **11**, 47–70.
125 S. Liu, Y. Guan, Y. Sheng, Y. Hu, Y. Rong, A. Mei and H. Han, *Adv. Energy Mater.*, 2020, **10**, 1902492.
126 S. Collavini, A. Cabrera-Espinoza and J. L. Delgado, *Macromolecules*, 2021, **54**, 5451–5463.
127 C.-Y. Chang, C.-Y. Chu, Y.-C. Huang, C.-W. Huang, S.-Y. Chang, C.-A. Chen, C.-Y. Chao and W.-F. Su, *ACS Appl. Mater. Interfaces*, 2015, **7**, 4955–4961.
128 L. Gang, Z. Weidong, H. Fengqin, C. Dazheng, Z. Chunfu and H. Yue, *Mater. Lett.*, 2019, **250**, 88–91.
129 C.-G. Wu, C.-H. Chiang, Z.-L. Tseng, M. K. Nazeeruddin, A. Hagfeldt and M. Grätzel, *Energy Environ. Sci.*, 2015, **8**, 2725–2733.
130 J. Wu, X. Xu, Y. Zhao, J. Shi, Y. Xu, Y. Luo, D. Li, H. Wu and Q. Meng, *ACS Appl. Mater. Interfaces*, 2017, **9**, 26937–26947.
131 Y. Wen, Y.-G. Tang and G.-Q. Yan, *AIP Adv.*, 2018, **8**, 095226.
132 Q. Chen, H. Zhou, Z. Hong, S. Luo, H.-S. Duan, H.-H. Wang, Y. Liu, G. Li and Y. Yang, *J. Am. Chem. Soc.*, 2014, **136**, 622–625.
133 D. Yang, R. Yang, J. Zhang, Z. Yang, S. Liu and C. Li, *Energy Environ. Sci.*, 2015, **8**, 3208–3214.
134 R. Vanaraj, V. Murugesan and B. Rathinam, *Micromachines*, 2024, **15**(7), 859.
135 H. S. Jung and N.-G. Park, *Small*, 2015, **11**, 10–25.
136 P. B. Pablo, N. Kazuteru, M. Nripan and G. M. Subodh, *Mater. Today*, 2014, **17**, 16–23.
137 Y. Wu, X. Yang, H. Chen, K. Zhang, C. Qin, J. Liu, W. Peng, A. Islam, E. Bi and F. Ye, *Appl. Phys. Express*, 2014, **7**, 052301.
138 J. Choi, S. Song, M. T. Hörantner, H. J. Snaith and T. Park, *ACS Nano*, 2016, **10**, 6029–6036.
139 G. E. Eperon, V. M. Burlakov, A. Goriely and H. J. Snaith, *ACS Nano*, 2014, **8**, 591–598.
140 F. Giordano, A. Abate, J. P. Correa Baena, M. Saliba, T. Matsui, S. H. Im, S. M. Zakeeruddin, M. K. Nazeeruddin, A. Hagfeldt and M. Graetzel, *Nat. Commun.*, 2016, **7**, 10379.
141 M. Dürr, A. Schmid, M. Obermaier, S. Rosselli, A. Yasuda and G. Nelles, *Nat. Mater.*, 2005, **4**, 607–611.
142 D. Zhang, T. Yoshida and H. Minoura, *Adv. Mater.*, 2003, **15**, 814–817.
143 B. J. Kim, D. H. Kim, Y.-Y. Lee, H.-W. Shin, G. S. Han, J. S. Hong, K. Mahmood, T. K. Ahn, Y.-C. Joo, K. S. Hong, N.-G. Park, S. Lee and H. S. Jung, *Energy Environ. Sci.*, 2015, **8**, 916–921.
144 D. Yang, R. Yang, X. Ren, X. Zhu, Z. Yang, C. Li and S. Liu, *Adv. Mater.*, 2016, **28**, 5206–5213.
145 I. Jeong, H. Jung, M. Park, J. S. Park, H. J. Son, J. Joo, J. Lee and M. J. Ko, *Nano Energy*, 2016, **28**, 380–389.
146 Z. Yang, W. Chen, A. Mei, Q. Li and Y. Liu, *J. Alloys Compd.*, 2021, **854**, 155488.
147 N. Gu, L. Song, P. Zhang, Y. Feng, P. Du, Y. Zhu, L. Ning, Z. Sun, H. Jiang and J. Xiong, *ACS Sustain. Chem. Eng.*, 2023, **11**, 13646–13655.
148 D. Liu and T. L. Kelly, *Nat. Photonics*, 2014, **8**, 133–138.
149 N. Chakravarthi, K. Gunasekar, W. Cho, D. X. Long, Y.-H. Kim, C. E. Song, J.-C. Lee, A. Facchetti, M. Song and Y.-Y. Noh, *Energy Environ. Sci.*, 2016, **9**, 2595–2602.
150 R. Azmi, W. T. Hadmojo, S. Sinaga, C. L. Lee, S. C. Yoon, I. H. Jung and S. Y. Jang, *Adv. Energy Mater.*, 2018, **8**, 1701683.
151 W. Chu, J. Yang, Q. Jiang, X. Li and J. Xin, *Appl. Surf. Sci.*, 2018, **440**, 1116–1122.
152 S. Shi, J. Li, T. Bu, S. Yang, J. Xiao, Y. Peng, W. Li, J. Zhong, Z. Ku, Y.-B. Cheng and F. Huang, *RSC Adv.*, 2019, **9**, 9946–9950.
153 M. Park, J.-Y. Kim, H. J. Son, C.-H. Lee, S. S. Jang and M. J. Ko, *Nano Energy*, 2016, **26**, 208–215.
154 C. Wang, L. Guan, D. Zhao, Y. Yu, C. R. Grice, Z. Song, R. A. Awni, J. Chen, J. Wang, X. Zhao and Y. Yan, *ACS Energy Lett.*, 2017, **2**, 2118–2124.
155 J.-X. Zhong, W.-Q. Wu, Y. Zhou, Q. Dong, P. Wang, H. Ma, Z. Wang, C.-Y. Yao, X. Chen, G.-l. Liu, Y. Shi and D.-B. Kuang, *Adv. Funct. Mater.*, 2022, **32**, 2200817.
156 M. J. Paik, J. W. Yoo, J. Park, E. Noh, H. Kim, S.-G. Ji, Y. Y. Kim and S. I. Seok, *ACS Energy Lett.*, 2022, **7**, 1864–1870.

157 C. Long, E. Feng, J. Chang, Y. Ding, Y. Gao, H. Li, B. Liu, Z. Zheng, L. Ding and J. Yang, *Appl. Phys. Lett.*, 2024, **124**, 123908.
158 Y. Shao, Z. Xiao, C. Bi, Y. Yuan and J. Huang, *Nat. Commun.*, 2014, **5**, 5784.
159 H. Wang, Z. Zhang, C. Zhang, Y. Yao and K. Wang, *J. Mater. Chem. A*, 2024, **12**, 22442–22457.
160 H. Yoon, S. M. Kang, J.-K. Lee and M. Choi, *Energy Environ. Sci.*, 2016, **9**, 2262–2266.
161 Y.-C. Wang, X. Li, L. Zhu, X. Liu, W. Zhang and J. Fang, *Adv. Energy Mater.*, 2017, **7**, 1701144.
162 E. Hou, J. Chen, J. Luo, Y. Fan, C. Sun, Y. Ding, P. Xu, H. Zhang, S. Cheng, X. Zhao, L. Xie, J. Yan, C. Tian and Z. Wei, *Angew. Chem., Int. Ed.*, 2024, **63**, e202402775.
163 J. Dou and Q. Chen, *Energy Mater. Adv.*, 2022, **2022**, 0002.
164 P. Gratia, A. Magomedov, T. Malinauskas, M. Daskeviciene, A. Abate, S. Ahmad, M. Grätzel, V. Getautis and M. K. Nazeeruddin, *Angew. Chem., Int. Ed.*, 2015, **54**, 11409–11413.
165 M. Saliba, S. Orlandi, T. Matsui, S. Aghazada, M. Cavazzini, J.-P. Correa-Baena, P. Gao, R. Scopelliti, E. Mosconi, K.-H. Dahmen, F. De Angelis, A. Abate, A. Hagfeldt, G. Pozzi, M. Graetzel and M. K. Nazeeruddin, *Nat. Energy*, 2016, **1**, 15017.
166 K. Kranthiraja, K. Gunasekar, H. Kim, A. N. Cho, N. G. Park, S. Kim, B. J. Kim, R. Nishikubo, A. Saeki and M. Song, *Adv. Mater.*, 2017, **29**, 1700183.
167 T. M. Brown, J. S. Kim, R. H. Friend, F. Cacialli, R. Daik and W. J. Feast, *Appl. Phys. Lett.*, 1999, **75**, 1679–1681.
168 J. You, Z. Hong, Y. Yang, Q. Chen, M. Cai, T.-B. Song, C.-C. Chen, S. Lu, Y. Liu, H. Zhou and Y. Yang, *ACS Nano*, 2014, **8**, 1674–1680.
169 A. M. Nardes, M. Kemerink, R. A. Janssen, J. A. Bastiaansen, N. M. Kiggen, B. M. Langeveld, A. J. Van Breemen and M. M. De Kok, *Adv. Mater.*, 2007, **19**, 1196–1200.
170 Y. Hou, H. Zhang, W. Chen, S. Chen, C. O. R. Quiroz, H. Azimi, A. Osvet, G. J. Matt, E. Zeira and J. Seuring, *Adv. Energy Mater.*, 2015, **5**, 1500543.
171 F. Hou, Z. Su, F. Jin, X. Yan, L. Wang, H. Zhao, J. Zhu, B. Chu and W. Li, *Nanoscale*, 2015, **7**, 9427–9432.
172 K.-G. Lim, S. Ahn, H. Kim, M.-R. Choi, D. H. Huh and T.-W. Lee, *Adv. Mater. Interfaces*, 2016, **3**, 1500678.
173 R. Saripally Sudhaker, S. Sungmin, A. Um Kanta, N. Ryosuke, S. Akinori, S. Myungkwan and J. Sung-Ho, *Nano Energy*, 2017, **41**, 10–17.
174 H. Li, K. Fu, P. P. Boix, L. H. Wong, A. Hagfeldt, M. Grätzel, S. G. Mhaisalkar and A. C. Grimsdale, *ChemSusChem*, 2014, **7**, 3420–3425.
175 W. Qi, B. Cheng and H. Jinsong, *Nano Energy*, 2015, **15**, 275–280.
176 J. W. Jo, M.-S. Seo, M. Park, J.-Y. Kim, J. S. Park, I. K. Han, H. Ahn, J. W. Jung, B.-H. Sohn, M. J. Ko and H. J. Son, *Adv. Funct. Mater.*, 2016, **26**, 4464–4471.
177 X. Yin, P. Chen, M. Que, Y. Xing, W. Que, C. Niu and J. Shao, *ACS Nano*, 2016, **10**, 3630–3636.
178 J.-Y. Jeng, K.-C. Chen, T.-Y. Chiang, P.-Y. Lin, T.-D. Tsai, Y.-C. Chang, T.-F. Guo, P. Chen, T.-C. Wen and Y.-J. Hsu, *Adv. Mater.*, 2014, **26**, 4107–4113.
179 Z. Zhu, Y. Bai, T. Zhang, Z. Liu, X. Long, Z. Wei, Z. Wang, L. Zhang, J. Wang and F. Yan, *Angew. Chem., Int. Ed.*, 2014, **53**, 12571–12575.
180 P. Vivo, J. K. Salunke and A. Priimagi, *Materials*, 2017, **10**(9), 1087.
181 F. Ye, W. Tang, F. Xie, M. Yin, J. He, Y. Wang, H. Chen, Y. Qiang, X. Yang and L. Han, *Adv. Mater.*, 2017, **29**, 1701440.
182 M. Najafi, F. Di Giacomo, D. Zhang, S. Shanmugam, A. Senes, W. Verhees, A. Hadipour, Y. Galagan, T. Aernouts, S. Veenstra and R. Andriessen, *Small*, 2018, **14**, 1702775.
183 Q. Wang, C.-C. Chueh, T. Zhao, J. Cheng, M. Eslamian, W. C. H. Choy and A. K. Y. Jen, *ChemSusChem*, 2017, **10**, 3794–3803.
184 Q. He, K. Yao, X. Wang, X. Xia, S. Leng and F. Li, *ACS Appl. Mater. Interfaces*, 2017, **9**, 41887–41897.
185 X. Liang, C. Ge, Q. Fang, W. Deng, S. Dey, H. Lin, Y. Zhang, X. Zhang, Q. Zhu and H. Hu, *Frontiers in Materials*, 2021, **8**, 634353.
186 C.-H. Sergio, L. Giulia, T. Michiel, F. Matthias, F. John and M. B. Thomas, *Cell Rep. Phys. Sci.*, 2020, **1**, 100045.
187 B. Abdollahi Nejand, P. Nazari, S. Gharibzadeh, V. Ahmadi and A. Moshaii, *Chem. Commun.*, 2017, **53**, 747–750.
188 S. You, H. Zeng, Z. Ku, X. Wang, Z. Wang, Y. Rong, Y. Zhao, X. Zheng, L. Luo, L. Li, S. Zhang, M. Li, X. Gao and X. Li, *Adv. Mater.*, 2020, **32**, 2003990.
189 D. Langley, G. Giusti, C. Mayousse, C. Celle, D. Bellet and J.-P. Simonato, *Nanotechnology*, 2013, **24**, 452001.
190 M. Lee, Y. Ko, B. K. Min and Y. Jun, *ChemSusChem*, 2016, **9**, 31–35.
191 E. Lee, J. Ahn, H.-C. Kwon, S. Ma, K. Kim, S. Yun and J. Moon, *Adv. Energy Mater.*, 2018, **8**, 1702182.
192 K. Poorkazem, D. Liu and T. L. Kelly, *J. Mater. Chem. A*, 2015, **3**, 9241–9248.
193 J. T.-W. Wang, J. M. Ball, E. M. Barea, A. Abate, J. A. Alexander-Webber, J. Huang, M. Saliba, I. Mora-Sero, J. Bisquert, H. J. Snaith and R. J. Nicholas, *Nano Lett.*, 2014, **14**, 724–730.
194 L. Zhike, Y. Peng, X. Chao, T. Guanqi and Y. Feng, *Nano Energy*, 2016, **28**, 151–157.
195 L. Gao, L. Chao, M. Hou, J. Liang, Y. Chen, H.-D. Yu and W. Huang, *npj Flexible Electron.*, 2019, **3**, 4.
196 K. Zhu, Z. Lu, S. Cong, G. Cheng, P. Ma, Y. Lou, J. Ding, N. Yuan, M. H. Rümmeli and G. Zou, *Small*, 2019, **15**, e1902878.
197 X. Dai, Y. Deng, C. H. Van Brackle, S. Chen, P. N. Rudd, X. Xiao, Y. Lin, B. Chen and J. Huang, *Adv. Energy Mater.*, 2020, **10**, 1903108.
198 Y.-R. Shi, C.-H. Chen, Y.-H. Lou and Z.-K. Wang, *Mater. Chem. Front.*, 2021, **5**, 7467–7478.
199 S. T. Williams, A. Rajagopal, C.-C. Chueh and A. K. Y. Jen, *J. Phys. Chem. Lett.*, 2016, **7**, 811–819.
200 S. S. Shin, W. S. Yang, J. H. Noh, J. H. Suk, N. J. Jeon, J. H. Park, J. S. Kim, W. M. Seong and S. I. Seok, *Nat. Commun.*, 2015, **6**, 7410.

201 V. Zardetto, T. M. Brown, A. Reale and A. Di Carlo, *J. Polym. Sci., Part B:Polym. Phys.*, 2011, **49**, 638–648.
202 D. Yang, R. Yang, K. Wang, C. Wu, X. Zhu, J. Feng, X. Ren, G. Fang, S. Priya and S. Liu, *Nat. Commun.*, 2018, **9**, 3239.
203 L. Lingbo, Z. Shasha, Y. Zhichun, B. Engamba Esso Samy and C. Wei, *J. Energy Chem.*, 2018, **27**, 673–689.
204 Z. Li, C. Xiao, Y. Yang, S. P. Harvey, D. H. Kim, J. A. Christians, M. Yang, P. Schulz, S. U. Nanayakkara, C.-S. Jiang, J. M. Luther, J. J. Berry, M. C. Beard, M. M. Al-Jassim and K. Zhu, *Energy Environ. Sci.*, 2017, **10**, 1234–1242.
205 J. Niu, D. Yang, X. Ren, Z. Yang, Y. Liu, X. Zhu, W. Zhao and S. Liu, *Org. Electron.*, 2017, **48**, 165–171.
206 J. Yang, B. D. Siempelkamp, D. Liu and T. L. Kelly, *ACS Nano*, 2015, **9**, 1955–1963.
207 Y. Fu, T. Wu, J. Wang, J. Zhai, M. J. Shearer, Y. Zhao, R. J. Hamers, E. Kan, K. Deng, X. Y. Zhu and S. Jin, *Nano Lett.*, 2017, **17**, 4405–4414.
208 I. S. Kim, D. H. Cao, D. B. Buchholz, J. D. Emery, O. K. Farha, J. T. Hupp, M. G. Kanatzidis and A. B. F. Martinson, *Nano Lett.*, 2016, **16**, 7786–7790.
209 H. C. Weerasinghe, Y. Dkhissi, A. D. Scully, R. A. Caruso and Y.-B. Cheng, *Nano Energy*, 2015, **18**, 118–125.
210 D. Yang, R. Yang, S. Priya and S. Liu, *Angew. Chem., Int. Ed.*, 2019, **58**, 4466–4483.
211 J. Deng, L. Qiu, X. Lu, Z. Yang, G. Guan, Z. Zhang and H. Peng, *J. Mater. Chem. A*, 2015, **3**, 21070–21076.
212 J.-Y. Lam, J.-Y. Chen, P.-C. Tsai, Y.-T. Hsieh, C.-C. Chueh, S.-H. Tung and W.-C. Chen, *RSC Adv.*, 2017, **7**, 54361–54368.
213 L. Chao, C. Shan, T. Zhengnan, S. Yingze, Y. Lianghao, L. Chen, S. Yuanlong, L. Jie, Z. Guifu, H. R. Mark, D. Shixue, S. Jingyu and L. Zhongfan, *Nano Energy*, 2019, **60**, 247–256.
214 X. Hu, Z. Huang, F. Li, M. Su, Z. Huang, Z. Zhao, Z. Cai, X. Yang, X. Meng, P. Li, Y. Wang, M. Li, Y. Chen and Y. Song, *Energy Environ. Sci.*, 2019, **12**, 979–987.
215 R. J. Boucher, *J. Aircr.*, 1985, **22**, 840–846.
216 N. T. Jafferis, E. F. Helbling, M. Karpelson and R. J. Wood, *Nature*, 2019, **570**, 491–495.
217 R. Zhang, J. F. Klotz, D. Wei, Z. Yang, A. Sherehiy, M. N. Saadatzi and D. O. Popa, *Journal of Micro and Bio Robotics*, 2020, **16**, 1–12.
218 D. Pérez-del-Rey, C. Dreessen, A. M. Igual-Muñoz, L. van den Hengel, M. C. Gélvez-Rueda, T. J. Savenije, F. C. Grozema, C. Zimmermann and H. J. Bolink, *Sol. RRL*, 2020, **4**, 2000447.
219 G. M. Paternò, V. Robbiano, L. Santarelli, A. Zampetti, C. Cazzaniga, V. Garcìa Sakai and F. Cacialli, *Sustainable Energy Fuels*, 2019, **3**, 2561–2566.
220 L. Cojocaru, S. Uchida, Y. Sanehira, V. Gonzalez-Pedro, J. Bisquert, J. Nakazaki, T. Kubo and H. Segawa, *Chem. Lett.*, 2015, **44**, 1557–1559.
221 Y. Miyazawa, M. Ikegami, H.-W. Chen, T. Ohshima, M. Imaizumi, K. Hirose and T. Miyasaka, *iScience*, 2018, **2**, 148–155.